Award Number: DAMD17-01-1-0502

TITLE: Breast Cancer Detection and Management Using 3D Quantitative Ultrasonic Diffraction Tomography

PRINCIPAL INVESTIGATOR: Xiaochuan Pan, Ph.D.

CONTRACTING ORGANIZATION: The University of Chicago
Chicago, Illinois 60637

REPORT DATE: May 2003

TYPE OF REPORT: Final

PREPARED FOR: U.S. Army Medical Research and Materiel Command
Fort Detrick, Maryland 21702-5012

DISTRIBUTION STATEMENT: Approved for Public Release;
Distribution Unlimited

The views, opinions and/or findings contained in this report are those of the author(s) and should not be construed as an official Department of the Army position, policy or decision unless so designated by other documentation.

REPORT DOCUMENTATION PAGE

Public reporting burden for this collection of information is estimated to average 1 hour per response, including the time for reviewing instructions, searching existing data sources, gathering and maintaining the data needed, and completing and reviewing this collection of information. Send comments regarding this burden estimate or any other aspect of this collection of information, including suggestions for reducing this burden to Washington Headquarters Services, Directorate for Information Operations and Reports, 1215 Jefferson Davis Highway, Suite 1204, Arlington, VA 22202-4302, and to the Office of Management and Budget, Paperwork Reduction Project (0704-0188), Washington, DC 20503

1. AGENCY USE ONLY (Leave blank)	2. REPORT DATE May 2003	3. REPORT TYPE AND DATES COVERED Final (1 May 01 – 30 Apr 03)

4. TITLE AND SUBTITLE
Breast Cancer Detection and Management Using 3D Quantitative Ultrasonic Diffraction Tomography

5. FUNDING NUMBERS
DAMD17-01-1-0502

6. AUTHOR(S)
Xiaochuan Pan, Ph.D.

7. PERFORMING ORGANIZATION NAME(S) AND ADDRESS(ES)
The University of Chicago
Chicago, Illinois 60637

E-Mail: xpan@uchicago.edu

8. PERFORMING ORGANIZATION REPORT NUMBER

9. SPONSORING / MONITORING AGENCY NAME(S) AND ADDRESS(ES)
U.S. Army Medical Research and Materiel Command
Fort Detrick, Maryland 21702-5012

10. SPONSORING / MONITORING AGENCY REPORT NUMBER

11. SUPPLEMENTARY NOTES

12a. DISTRIBUTION / AVAILABILITY STATEMENT
Approved for Public Release; Distribution Unlimited

12b. DISTRIBUTION CODE

13. ABSTRACT (Maximum 200 Words)

The broad objective of the project is to investigate, develop, and evaluate the application of 3D ultrasonic diffraction tomography (UDT) for detection of breast cancer. UDT can be viewed as a generalization of x-ray tomography where x-rays have been replaced with acoustical wave. It can determine refractive index distributions within the breast that are of interest clinically and can be an excellent imaging modality for breast cancer because it can provide information complementary to that obtained from mammograms and because it is non-invasive, free of radiation hazard, and reproducible. While UDT promises potentially important advantages over conventional ultrasonic imaging and has found important uses in a wide variety of engineering and scientific disciplines, its application to breast imaging remains largely unexplored. In the past two years, our research on this project has been supported by a Concept Award from the U.S. Army MRMC. We have developed and evaluated optimal algorithms for accurate reconstruction of UDT images that may find applications in UDT imaging of breast cancer. We made contributions to UDT research, as summarized in the report. These results are necessary in making UDT a viable medical technique for imaging of breast cancer.

14. SUBJECT TERMS
Ultrasonic diffraction tomography, Breast Cancer Detection

15. NUMBER OF PAGES
49

16. PRICE CODE

17. SECURITY CLASSIFICATION OF REPORT Unclassified	18. SECURITY CLASSIFICATION OF THIS PAGE Unclassified	19. SECURITY CLASSIFICATION OF ABSTRACT Unclassified	20. LIMITATION OF ABSTRACT Unlimited

NSN 7540-01-280-5500

Table of Contents

1   Introduction

The broad objective of the proposed project is to investigate, develop, and evaluate computationally efficient [1] and statistically optimal [2–4] algorithms for accurate image reconstruction in three-dimensional (3D) Ultrasonic diffraction tomography (UDT) imaging of the breast cancer. UDT [5–7] can be viewed as a generalization of X-ray tomography where X-rays have been replaced with an acoustical wavefield. Because UDT is non-invasive, free of radiation hazard, and reproducible, it is potentially an excellent tool for imaging of breast cancer [8, 9]. While UDT promises several potentially important advantages over conventional ultrasonic imaging and has found important uses in a wide variety of engineering and scientific disciplines, its application to imaging of breast cancer still remains largely unexplored. In the past two years, our research on this project has been supported by a Concept Award of the US Army Medical Research adn Material Command, and we believe that our research has been successful and productive. The report below summarizes our research activities and results on the project to date.

2   Body

Our research activities on the project to date can be grouped naturally into 4 categories. The first was the investigation of efficient linear algorithms for image reconstruction from 3D data and from minimum scan data. The second was the development of efficient nonlinear algorithms for 2D and 3D image reconstructions. The third was the applications of the developed algorithms to simulated and experimental data for evaluation of their performance. Finally, as a by product, we developed short-scan reconstruction algorithms for reflection-mode ultrasound tomography that can also be a potentially important modality for imaging of the breast cancer.

2.1   Development of efficient linear reconstruction algorithms

In breast imaging applications of ultrasound, the first-order Born or Rytov approximations are typically not valid, and consequently, a linearized Helmholtz equation may not accurately describe the relationship between the measured scattered wavefield and the scattering

4

tissue [10–18]. However, many nonlinear reconstruction algorithms that account for multiple-scattering effects, including the ones we discuss below [19], involve the recursive application of a linear reconstruction algorithm (that assumes the validity of the first-order Born or Rytov approximation.) It is therefore very important to develop computational efficient and numerically robust linear reconstruction algorithms for DT. Below, we discuss our results on this salient topic.

2.1.1 Development of 3D efficient reconstruction algorithms

In 2D DT, the filtered backpropagation (FBPP) algorithm is [5] widely used for image reconstruction and is generally regarded as being more accurate than direct Fourier reconstruction approaches. However, objects such as the female breast are inherently three-dimensional and must be reconstructed using fully 3D reconstruction algorithms in order to avoid significant artifacts and a loss of quantitative accuracy. We developed and evaluated novel reconstruction algorithms for 3D DT, referred to as the esstimation-combination (E-C) reconstruction algorithms, that effectively solve the (fully) 3D DT reconstruction problem by performing a series of 2D Radon transform inversions [20]. This greatly reduces the large computational load that is generally required by any other 3D DT reconstruction technique such as the 3D FBPP algorithm. This is vitally important for the development of computationally tractable 3D nonlinear algorithms that involve the recursive application of a 3D linear reconstruction algorithm. We also demonstrated that, in the presence of data noise, there is redundant information contained in the 3D DT data function that can be exploited by the 3D E-C algorithms to reduce the variance of the reconstructed image [19].

2.1.2 Development of minimum-scan reconstruction algorithms

In many applications of tomographic imaging it is desirable to minimize the angular range over which the measurement data are acquired. This reduces the time necessary to collect the measurement data, which can reduce artifacts due to patient motion. Furthermore, in certain situations it may not be experimentally possible to collect data over a complete 2π range. We demonstrated that a minimal-scan data set acquired using view angles only in $[0, \phi_{min}]$ contains all the information necessary to reconstruct exactly a 2D scattering object function, where $\pi \leq \phi_{min} \leq 3\pi/2$ is a function of the measurement geometry. Based on this ob-

servation, we developed, investigated, and numerically implemented minimal-scan FBPP and E-C reconstruction algorithms for 2D DT that can exactly reconstruct the scattering object function from the minimal scan data set. *Prior to our work, all reconstruction algorithms for DT required a full 2π worth of angular measurements to reconstruct an accurate image.* We numerically demonstrated that the minimal-scan E-C reconstruction algorithms were less susceptible to the effects of data noise and inconsistencies than were the minimal-scan FBPP reconstruction algorithms. We also generalized this work to 2D DT using the fan-beam geometry and revealed a novel relationship between the maximum scanning angle and achievable image resolution. This work may provide useful insights into the development of minimum-scan reconstruction algorithms for 3D DT that can be used for breast imaging [21].

2.2 Development of efficient nonlinear reconstruction algorithms

In certain situations of the breast imaging, the first-order Born or Rytov approximations may not be valid. Consequently, a linearized Helmholtz equation may not accurately describe the relationship between the measured scattered wavefield and the scattering object, and nonlinear algorithms are necessary for obtaining accurate images. We proposed to develop efficient nonlinear reconstruction algorithms for UDT.

2.2.1 Development of 2D efficient nonlinear reconstruction algorithms

Previously we described our development and investigation of E-C reconstruction algorithms for linear DT. We have generalized these algorithms to the case where a forward scattering model includes multiple-scattering effects. Two forward scattering models were utilized that captured higher-order terms in the Born or Rytov perturbation series, and are therefore potentially useful for modeling ultrasound wave propagation in breast tissue [22, 23]. For each of the two forward scattering models, we developed families of nonlinear E-C reconstruction algorithms to solve the inverse problem [19]. The nonlinear E-C reconstruction algorithms operate by relating, in 2D Fourier space of the Radon transform, the n-th order perturbation of the measured data function to the n-th order perturbation of the scattering object function. The algorithms are recursive in the sense that calculation of the n-th order perturbation of the object function requires knowledge of the $(n$-1$)$-th order perturbation. The computational

efficiency of the E-C algorithms is therefore very relevant to this problem. We also identified consistency conditions for the nonlinear imaging models employed by the two families of nonlinear E-C algorithms. For both imaging models, the consistency conditions for linear DT were contained as special cases.

2.2.2 Development of 3D efficient nonlinear reconstruction algorithms

Although we have been largely successful in the theoretical development of computationally efficient nonlinear algorithms for 2D UDT, the applicability of such algorithms can be restrictive because the multi-scattering effect in the breast imaging is generally 3D in nature. Therefore, we have also investigated 3D nonlinear reconstruction algorithms. Our strategy for the development of 3D nonlinear reconstruction algorithms is similar to that for 2D nonlinear reconstruction discussed above. Specifically, we proposed to investigate the two mentioned forward models in 3D and to use the perturbation series for the inversion. The inversion of the solution at each perturbative order will be accomplished through the use of our developed linear 3D E-C algorithms for improving the computational efficiency. We have also made progress on the development of such 3D perturbative nonlinear algorithms.

2.3 Implementation and evaluation of the proposed algorithms

We have implemented the proposed linear algorithms and nonlinear algorithms and evaluated them by use of computer simulated data and real data.

2.3.1 Implementation and evaluation of linear reconstruction algorithms

We have implemented the linear E-C reconstruction algorithms and investigated their noise properties by using a large number of computer simulated data sets. Through our simulation studies, we have demonstrated that it is possible to achieve a bias-free reduction of the statistical variation in the reconstructed object function by utilizing complementary statistical information inherent in the scattered data. (The use of an explicit smoothing operation generally introduces bias in the reconstructed scattering object function.) We have quantitatively demonstrated that the E-C algorithms are less susceptible to data noise and other finite sampling effects than are the corresponding FBPP algorithms. This result is consistent with the observation that the FBPP algorithms involve more complicated numerical operations (e.g.,

7

backpropagation) than do the E-C algorithms, which may amplify the propagation of noise and errors into the reconstructed image. Using simulated strongly scattering data, we have demonstrated that the E-C algorithms are less susceptible to modeling errors due to violation of first-order scattering approximations. These same results have been verified for the minimum-scan DT problem.

2.3.2 Implementation and evaluation of nonlinear reconstruction algorithms

Using simulated strongly scattering data, we have started to numerically investigate nonlinear reconstruction algorithms for 2D DT. As described in Section 2.2.1, our nonlinear reconstruction algorithms utilize a forward scattering operator that assumes the validity of a higher-order Born or Rytov terms. An accurate numerical implementation of the forward scattering operator is critical for obtaining accurate reconstructions using our algorithms. In a preliminary study, we have encountered difficulty in achieving an accurate numerical implementation of this operator. The forward scattering models employed by our families of nonlinear algorithms involve an integration over a complex frequency variable, which is not computable in practice. Accordingly, numerical inaccuracies were introduced by truncating the limits of integration, which we observed to introduce a severe degradation in the reconstructed image quality. Compensation for such image degradations is a challenging task, and we are still investigating methods for efficiently and adequately mitigating the effects of the integration truncation used by the forward scattering operator.

2.4 Development and evaluation of reconstruction algorithms for reflectivity tomography

Reflectivity tomography has been applied to numerous biomedical and non-destructive test imaging problems [24–27]. It has a strong relationship to UDT and can be a potential useful technique for imaging the breast cancer. The task in reflectivity tomography is to reconstruct from the measured data a function describing the reflectivity distribution within the breast. It has been generally considered that accurate images can be reconstructed only from full scan data over 2π. Recently, we have investigated and evaluated image reconstruction from minimum-scan data in reflectivity tomography. Using the so-called potato-peeler perspective that we developed, we showed that accurate images can be reconstructed from minimum-scan

data in reflectivity tomography. We also performed quantitative studies by use of computer simulated data, and the results in such studies validated our theoretical results for image reconstruction in minimum-scan reflectivity tomography. One of our papers on 2D reflectivity tomography is to be published in the July issue of *IEEE Transactions on Image Processing* [28]. Furthermore, we have generalized our results to 3D reflectivity tomography, and our paper on this topic has been accepted for presentation by the notoriously competitive international conferences on 3D image reconstruction [29].

3 Key research accomplishments

- We have developed and evaluated computationally efficient 3D linear reconstruction algorithms that are more than 100 times faster than the conventional 3D FBPP algorithm.

- We have investigated, developed, and evaluated algorithms for image reconstruction from minimum-scan data in UDT with plane wave sources.

- We have investigated, developed, and evaluated algorithms for image reconstruction from full-scan and minimum-scan data in UDT with fan-beam wave sources.

- We have developed and evaluated computationally efficient 3D linear reconstruction algorithms for UDT with spherical wave sources.

- We have developed computationally efficient 2D nonlinear reconstruction algorithms for UDT with plane wave sources.

- We have investigated theoretically the development of computationally efficient nonlinear reconstruction algorithms for 3D UDT.

- We have developed computer codes that implement the proposed linear and nonlinear reconstruction algorithms.

- We have evaluated the developed linear and nonlinear reconstruction algorithms by use of computer simulated and experimental data.

- We have developed and evaluated reconstruction algorithms for 2D short-scan reflectivity tomography.

9

- We have developed and evaluated reconstruction algorithms for 3D short-scan reflectivity tomography.

4 Reportable outcomes

10 papers and 3 conference abstracts were published as listed in **Section 6. Bibliography** below.

5 Bibliography of all Publications

Peer-Reviewed Original Articles

1. M. Anastasio and X. Pan: Full- and minimal-scan reconstruction algorithms for fan-beam diffraction tomography, *Appl. Opt.*, **40**, 3334-3345, 2001.

2. X. Pan and M. Anastasio: On a limited-view reconstruction problem in wavefield tomography, *IEEE Trans. Med. Imaging.*, **21**, 413-416, 2002.

3. M. Anastasio and X. Pan: Numerically robust minimal-scan reconstruction algorithms for diffraction tomography via Radon transform inversion, *Int. J. Imag. Sys. Tech.*, **12**, 84-91, 2002.

4. M. Anastasio and X. Pan: An improved reconstruction algorithm for 3D diffraction tomography with spheric-wave sources, *IEEE Trans. Biomed. Eng.*, (in press), 2003.

5. X. Pan, Y. Zou, and M. Anastasio: Data redundancy and reduced-scan reconstruction algorithms in reflectivity tomography, *IEEE Trans. Image Processing*, (in press), 2003.

6. X. Pan, Y. Zou, and M. Anastasio: Image reconstruction of reflectivity from short scan data, *CD Proc. of International Symposium on Biomedical Imaging*, Washington D. C., 2002.

7. X. Pan, Y. Zou, M. Anastasio, and E. Sidky: Reduced-scan image reconstruction in 3D reflectivity tomography, *Proc. Int. Meeting Fully 3D Image Recon. in Radiol. and Nucl. Med.*, (in press), 2003.

Ph.D. Thesis

1. M. Anastasio: Development and analysis of image reconstruction algorithms in diffraction tomography, The University of Chicago, 2001.

Peer-Reviewed Proceedings Articles

1. X. Pan and M. Anastasio: Minimal-scan reconstruction algorithms for fan-beam diffraction tomography and their analogy to halfscan fan-beam CT, *IEEE Medical Imaging Conference Record (CD)*, 2001.

2. M. Anastasio and X. Pan: Development and evaluation of minimal-scan reconstruction algorithms for diffraction tomography, *Proc. SPIE*, **1322**, 860-866, 2001.

3. X. Pan, Y. Zou, and M. Anastasio: Image reconstruction from reduced-scan data in ultrasonic reflectivity tomography, *Proc. SPIE*, (in press), 2003.

Abstracts and Presentations

1. X. Pan and M. Anastasio: Reconstruction algorithms in diffraction tomography, Advanced Light Source, Lawrence Berkeley National Laboratory, California, (Host: Dr. Malcolm Howells), October 29, 2001.

2. M. Anastasio, Y. Zou, and X. Pan: Reflectivity tomography using temporally truncated data, *The 2nd Joint Meeting of the IEEE Engineering in Medicine and Biology Society and Biomedical Engineering Society*, Houston, 2002.

3. Y. Zou, M. Anastasio, and X. Pan: Data truncation and the exterior problem in reflection-mode tomography, *IEEE Medical Imaging Conference*, Norfolk, 2002.

6   Conclusion

Ultrasonic diffraction tomography is a potentially important technique for imaging of the breast cancer. In this project, we have investigated, developed, and evaluated computationally efficient and statistically optimal algorithms for accurate reconstruction of UDT images

that may find applications in UDT imaging of breast cancer. In the past two years, we have made contributions to UDT research, as summarized above. Our research on UDT have addressed numerous scientific and engineering problems involved in UDT image reconstruction. These results are necessary in making UDT a viable medical imaging technique for imaging breast cancer.

7 List of Personnel

Xiaochuan Pan, Ph.D., Associate Professor
Mark Anastasio, Ph.D., Assistant Professor
Yu Zou, Ph.D., Research Associate (Instructor)
Lifeng Yu, M.S., Research Assistant

References

[1] M. Anastasio and X. Pan. Full- and minimal-scan reconstruction algorithms for fan-beam diffraction tomography. *Appl. Opt.*, 40, 2001.

[2] D. Rouseff and R. Porter. Diffraction tomography and the stochastic inverse scattering problem. *Journal of the Acoustical Society of America*, 89:1599–1605, 1991.

[3] G. Tsihrintzis and A. Devaney. Stochastic diffraction tomography: Theory and computer simulation. *Signal Processing*, 93:49–64, 1993.

[4] X. Pan. A unified reconstruction theory for diffraction tomography with considerations of noise control. *Journal of the Optical Society of America*, 15:2312–2326, 1998.

[5] A. Devaney. A filtered backpropagation algorithm for diffraction tomography. *Ultrasonic Imaging*, 4:336–350, 1982.

[6] S. Pan and A. Kak. A computational study of reconstruction algorithms for diffraction tomography: Interpolation versus filtered backpropagation. *IEEE Transactions on Acoustics, Speech, and Signal Processing*, 31:1262–1275, 1983.

[7] M. Kaveh, M. Soumekh, and J. Greenleaf. Signal processing for diffraction tomography. *IEEE Transactions on Sonics and Ultrasonics*, 31:230–239, 1984.

[8] M. Andre, H. Janee, G. Otto, P. Martin, G. Otto, and B. Spivey. High-speed data acquisition in a diffraction tomography system employing large-scale toroidal arrays. *Int. J. Imaging Syst. Technol.*, 8:137–147, 1997.

[9] R. Waag, A. Nachman, and T. Mast. New method and apparatus for imaging. In *Department of Defense Breast Cancer Research Program Meeting*, Washington,D.C., 1997.

[10] F. Lin and M. Fiddy. Image estimation from scattered field data. *Int J. Imag. Sys. Tech.*, 2:76–95, 1990.

[11] R. G. Newton. Inverse scattering II. Three dimensions. *J. Math Phys.*, 21:1698–1715, 1981.

[12] R. G. Newton. Inverse scattering II. Three dimensions, continued. *J. Math Phys.*, 22:2191–2200, 1981.

[13] D. Colton and P. Monk. The inverse scattering problem for time harmonic acoustic waves in an inhomogeneous medium. *Q. J. Mech. Appl. Math.*, 41:97–125, 1988.

[14] Y. Wang and W. C. Chew. Solution of large 2-D inhomogeneous scatterers for TM waves by fast recursive algorithm. *Micro. Opt. Tech. Lett.*, 4, 1991.

[15] S. Johnson and M. Tracy. Inverse scattering solutions by a sinc basis, multiple source, moment method - Part I:theory. *Ultrasonic Imaging*, 5:361–375, 1983.

[16] S. Johnson and M. Tracy. Inverse scattering solutions by a sinc basis, multiple source, moment method - Part II:numerical evaluations. *Ultrasonic Imaging*, 5:376–392, 1983.

[17] M. Moghaddam and W. C. Chew. Study of some practical issues in inversion with the Born iterative method using time domain data. *IEEE Trans. Antennas Propag.*, 41:177–184, 1993.

[18] W. Chew and Y. Wang. Reconstruction of two-dimensional permittivity distribution using the distorted Born iterative method. *IEEE Transactions on Medical Imaging*, 9:218–225, 1990.

[19] M. Anastasio. Development and analysis of iamge reconstruction algorithms in diffraction tomography. Ph.D. Thesis, The University of Chicago, 2001.

[20] M. Anastasio and X. Pan. Computationally efficient and statistically robust image reconstruction in 3D diffraction tomography. *J. Opt. Soc. Am.*, 17:391–400, 2000.

[21] X. Pan and M. Anastasio. On a limited-view reconstruction problem in wavefield tomography. *IEEE Trans. Med. Imaging*, 21, 2002.

[22] C. Lu, W. Chew, and G. Otto. Image reconstruction with acoustic measurement using distorted Born iterative method. *Ultrasonic Imaging*, 18:140–156, 1996.

[23] G. A. Tsihrintzis and A. J. Devaney. Higher-order (nonlinear) diffraction tomography: Reconstruction algorithms and computer simulation.

[24] S. Norton and M. Linzer. Ultrasonic reflectivity imaging in three dimensions: Exact inverse scattering solutions for plane, cylindrical, and spherical aperatures. *J. Acous. Soc. Am.*, 67, 1980.

[25] M. Moshfeghhi. Ultrasound reflection-mode tomography using fan-shaped-beam insonification. *IEEE Transactions on Ultrasonics, Ferroelectrics and Frequency Control*, 33:299–314, 1986.

[26] K. Dines and A. Goss. Computer ultrasonic reflection tomography. *IEEE Transactions on Ultrasonics, Ferroelectrics and Frequency Control*, 34:309–317, 1987.

[27] J. Ylitalo, J. Kaovukangas, and J. Oksman. Ultrasonic reflection mode computed tomography through a skullbone. *IEEE Transactions on Biomedical Engineering*, 37:1059–1065, 1990.

[28] X. Pan, Y. Zou, and M. Anastasio. Data redundancy and reduced-scan reconstruction algorithms in reflectivity tomography. *IEEE Trans Image Processing*, (in press), 2003.

[29] X. Pan, Y. Zou, M. Anastasio, and E. Sidky. Reduced-scan image reconstruction in 3D reflectivity tomography. *Proc. Int. Meeting Fully 3D Image Recon. in Radiol. and Nucl. Med.*, (in press), 2003.

Appendix: Attached articles

Reduced-Scan Image Reconstruction in 3D Reflectivity Tomography

Xiaochuan Pan, Yu Zou, Mark A. Anastasio[†] and Emil Y. Sidky

Department of Radiology

The University of Chicago, Chicago, IL 60637

† Department of Biomedical Engineering

Illinois Institute of Technology, Chicago, IL 60616

I. INTRODUCTION

Because of its great potential in biomedical imaging, reflectivity tomography using ultrasound sources has been widely studied since the late 1970s [1–4]. Recently there has been a renewed interest in reflectivity tomography due to the similarity of its mathematical structure to that of developing imaging modalities such as thermoacoustic computed tomography (CT) [5]. In three-dimensional (3D) reflectivity tomography, a weakly reflecting object, immersed in an acoustically homogeneous background medium, is illuminated with short ultrasonic pulses that are located at different positions on a spherical surface, enclosing the object, and the concomitant reflected signals are measured as functions of time at each of the multiple source locations. The task in 3D reflectivity tomography is to reconstruct from such measured data a function describing the reflectivity distribution within the scattering object[1]. Under certain physical conditions, the 3D reflectivity tomography reconstruction problem is tantamount to the problem of reconstructing a 3D function from knowledge of its integrals over sets of spherical surfaces with varying radii that are centered at the source-receiver locations; i.e., a generalized 3D Radon transform inversion problem.

In their seminal paper, Norton and Linzer [2] derived an explicit and exact inversion formula for reconstructing the object function from data acquired at all source-receiver locations on the measurement sphere. We refer to such an imaging configuration that utilizes 4π steradians worth of measurements as a *full-scan* geometry. In many medical imaging applications it is not feasible to collect a complete data set using the full-scan geometry. In this situation, we have a *reduced-scan* measurement geometry and an associated limited-angle tomographic reconstruction problem. When imaging the female breast, for example, only reduced-scan measurements acquired over a hemisphere can be obtained readily.

In other tomographic imaging modalities including fan-beam computed tomography (CT) [6] and single-photon emission computed tomography (SPECT) [7], it has been shown that one can accurately reconstruct images from data acquired with reduced-scan configurations. However, the exact inversion formula of Norton and Linzer [2] cannot

reconstruct, in general, accurate images from reduced-scan data. A reduced-scan reconstruction problem for 3D reflectivity tomography has been investigated in [8]. In that work, which was based on the paraxial approximation, approximate reconstruction algorithms were proposed that assumed full-scan or reduced-scan measurement geometries. Their results suggested that the hemisphere reduced-scan geometry could yield approximation reconstructions that were comparable in quality to the approximate reconstructions yielded by the full-scan geometry. However, it remains unclear whether an object function can be *exactly* determined from certain reduced-scan data sets in 3D reflectivity tomography.

In this work, we investigate the problem of reconstructing an exact image from reduced-scan data in 3D reflectivity tomography. A potato-peeler perspective, which is conceptually similar to "layer-stripping" methods, is proposed for identifying data symmetries in 3D reflectivity tomography. Using the identified data symmetries, we *heuristically* demonstrate that, under certain conditions, data acquired with reduced-scan configurations in reflectivity tomography are sufficient to completely specify the object function. It is interesting to note that our observations regarding the stability of the reduced-scan reflectivity tomography reconstruction problem can be related readily to a similar analysis of the limited-view thermoacoustic CT problem [9].

II. DATA FUNCTION IN 3D REFLECTIVITY TOMOGRAPHY

Consider an acoustic medium that contains a compactly supported region $\mathcal{R}$, residing completely inside a sphere of radius R_f centered at the origin. The region $\mathcal{R}$ is characterized by an inhomogeneous compressibility $\kappa(\vec{r})$ and density $\rho(\vec{r})$. Outside of $\mathcal{R}$, the background medium has no absorption and homogeneous compressibility κ_0 and density ρ_0. This implies a constant speed of sound in the background medium that is denoted by c_0. The reflectivity function of the medium is defined as

$$f(\vec{r}) = \gamma_k(\vec{r}) - \gamma_\rho(\vec{r}), \qquad (1)$$

where

$$\gamma_k(\vec{r}) = \begin{cases} \frac{\kappa - \kappa_0}{\kappa_0} & : \ \vec{r} \in \mathcal{R} \\ 0 & : \ \vec{r} \notin \mathcal{R} \end{cases} \qquad (2)$$

---

[1] For simplicity, we refer to the object's reflectivity function as the object function.

and

$$\gamma_p(\vec{r}) = \begin{cases} \frac{\rho - \rho_0}{\rho_0} & : \quad \vec{r} \in \mathcal{R} \\ 0 & : \quad \vec{r} \notin \mathcal{R}. \end{cases} \quad (3)$$

Consider a (measurement) sphere, which has a radius R_0 and is centered at the origin, that encloses the acoustical inhomogeneity, i.e, the region $\mathcal{R}$. Let $\vec{r}_0 \in \Omega_0$ where Ω_0 denotes the set of vectors that reside on the surface of the measurement sphere. The vector components of $\vec{r}_0$ in spherical coordinates are indicated by (θ_0, ϕ_0, R_0). At time $t = 0$, an omni-directional acoustic point source with time dependence $p(\bar{t})$ located at position $\vec{r}_0$ emits a spherical pulse $\psi_{inc}(\vec{r}; \bar{t})$ into the region $\mathcal{R}$, where $\bar{t} \equiv c_o t$. As the spherically-diverging pulse propagates into the inhomogeneous region $\mathcal{R}$, echos will be produced that propagate back to the source location. These echos, which physically represent fluctuations in acoustic pressure, are functions of time and will be denoted by the function $\psi(\vec{r}_0; \bar{t}) = \psi_T(\vec{r}_0; \bar{t}) - \psi_{inc}(\vec{r}_0; \bar{t})$, where $\psi_T(\vec{r}_0; \bar{t})$ and $\psi_{inc}(\vec{r}_0; \bar{t})$ represent the total and incident wavefields, respectively. Because $\psi_T(\vec{r}_0; \bar{t})$ is directly measured and $\psi_{inc}(\vec{r}_0; \bar{t})$ is known, $\psi(\vec{r}_0; \bar{t})$ can be interpreted as a measurable quantity.

In order to define conveniently the relationship between $f(\vec{r})$ and the measured echo signal $\psi(\vec{r}_0; t)$, we introduce the temporal Fourier transform pairs

$$\hat{p}(k) = \int_{-\infty}^{\infty} p(\bar{t}) \, e^{-jk\bar{t}} d\bar{t}, \quad (4)$$

and

$$\hat{\psi}(\vec{r}_0; k) = \int_{-\infty}^{\infty} \psi(\vec{r}_0, \bar{t}) \, e^{-jk\bar{t}} d\bar{t}, \quad (5)$$

where $\hat{p}$ and $\hat{\psi}$ denote the Fourier transformed quantities. Furthermore, it is useful to define the intermediate quantity

$$\hat{\psi}_1(\vec{r}_0; k) \equiv \frac{d}{dk} \left[\frac{j16\pi \hat{\psi}(\vec{r}_0; k/2)}{k^2 \hat{p}(k/2)} \right], \quad (6)$$

and let $\psi_1(\vec{r}_0; \bar{t})$ denote its inverse Fourier transform. As derived in [2], the mathematical relationship between $f(\vec{r})$ and the measured echo signal $\psi(\vec{r}_0, \bar{t})$ is given by

$$g(\vec{r}_0; \bar{t}) = \int_{\mathcal{R}} d^3\vec{r} \, f(\vec{r}) \, \delta(\bar{t} - |\vec{r} - \vec{r}_0|), \quad (7)$$

where the modified data function is $g(\vec{r}_0; \bar{t}) \equiv 2\bar{t}\psi_1(\vec{r}_0; \bar{t})$. Notice that $g(\vec{r}_0; \bar{t})$ is equal to integrals of $f(\vec{r})$ calculated over concentric spherical surfaces with radii $\bar{t}$ that are centered at the source-receiver location $\vec{r}_0$. The goal of (conventional full-scan) 3D reflectivity tomography is to utilize knowledge of $g(\vec{r}_0; \bar{t})$ for $\vec{r}_0 \in \Omega_0$ and $\bar{t} \in [0, R_0 + R_f]$ to determine $f(\vec{r})$ by inverting the generalized Radon transform given in Eq. (7).

III. Full-scan Inversion Formula

Let $\vec{r} = (\theta, \phi, r)$ denote a point inside the measurement sphere and, as before, let $\vec{r}_0 = (\theta_0, \phi_0, r_0) \in \Omega_0$ reside on the measurement surface. The unit vectors $\vec{n}$ and $\vec{n}_0$ describe the directions of $\vec{r}$ and $\vec{r}_0$, respectively. For a full-scan geometry where $g(\vec{r}_0; \bar{t})$ is completely specified for $\vec{r}_0 \in \Omega_0$ and $\bar{t} \in [0, R_0 + R_f]$, Norton and Linzer [2] derived an exact explicit inversion formula given by

$$f(\vec{r}) = \int_{\Omega_0} d\Omega_0 \int_{-\infty}^{\infty} dk \, \hat{\psi}_1(\vec{r}_0; k) K(r, k; \vec{n} \cdot \vec{n}_0), \quad (8)$$

where

$$K(r, k; \vec{n} \cdot \vec{n}_0) = \frac{jk}{(2\pi)^2} \sum_{n=0}^{\infty} \frac{(2n+1)j_n(kr)}{h_n^{(1)}(kr_0)} P_n(\vec{n} \cdot \vec{n}_0). \quad (9)$$

In Eq. (8), $j_n(\cdot)$, $h_n^{(1)}(\cdot)$ and $P_n(\cdot)$ are the n-th order spherical Bessel, Hankel and Legendre polynomial functions, respectively.

Due to the infinite summation, the numerical implementation of Eq. (8) is computationally demanding. In [2], the following approximate inversion formula for determining $f(\vec{r})$ was also proposed:

$$f_a(\vec{r}) = \alpha_0 \int_{\Omega_0} d\Omega_0 \, \psi(\vec{r}_0; 2|\vec{r} - \vec{r}_0|), \quad (10)$$

where α_0 is a constant. Equation 10 describes a simple backprojection of the echo data ψ over the spherical surfaces from which the echos originated, summed over all of the source-receiver locations in Ω_0 (the surface of the measurement sphere). It was demonstrated [2] that Eq. (10) closely approximates the exact inversion formula given in Eq. (8). This result was explained by revealing that the scattering process itself inherently provides the correct filtering of the measurement data prior to application of the backprojection operation in Eq. (10).

IV. The Potato-peeler Perspective and Reduced-scan in 3D Reflectivity Tomography

The data function in Eq. (7) does not have an obvious symmetry such as that of the Radon transform, where measurements at conjugate views are mathematically equal. But if we assume that the object function has compact support, then we can apply the potato peeler perspective for revealing redundant information in tomographic data functions. The potato peeler perspective has been applied both heuristically [10, 11] and mathematically [12, 13] to show that half-detector [13] and π-scheme [10] (a generalization of the 180° short-scan) data contain enough information to uniquely determine the object function. The same perspective has also shown the data redundancy in SPECT when the effect of distant dependent spatial resolution is included [11]. The potato peeler perspective has already been applied to 2D reflectivity tomography [14]. We review the argument for redundant information in 2D reflectivity tomography and then move on to show that data covering views over 2π steradians are sufficient to determine the object function in 3D reflectivity tomography.
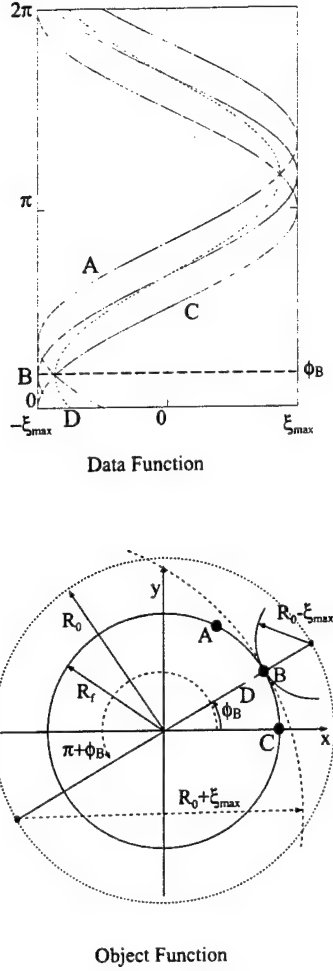
Data Function

Object Function

Fig. 1. Schematic of data function (top) and two-dimensional object function (bottom) for the heuristic potato peeler perspective. Points A, B, and C lie on the outermost ring of the object support, and their loci in the data space are also shown. The illustrated integration arcs from opposing views ϕ_B and $\phi_B + \pi$ intersect the support disk at B. When the outermost ring along with points A, B and C are removed, D becomes a point on the outermost edge.

A. 2D reflectivity tomography

In analogy with the 3D case, the source position is specified by a 2D vector in polar coordinates, $\vec{r}_0(\phi_0, R_0)$, and Eq. (7) holds as the data function except that the vectors are replaced by 2D counterparts and the integration sphere becomes an arc. Without loss of generality we assume that the support of the object function lies within a disk of radius R_f centered at the origin of the measurement circle, see Fig. 1. Let $L(\xi, \phi_0)$ denote the integration arc from the 2D reflectivity tomography data function, where the coordinate $\xi \equiv \bar{t} - R_0$ measures the position of the wave fronts relative to the center of the measurement circle. The key observation is that there exists a value of $\xi = \xi_{max}$ such that $L(\xi_{max}, \phi_B)$ intersects the support disk at one point. Specifically, consider the view angle ϕ_B shown in Fig. 1. The data point $g(\vec{r}_B, -\xi_{max})$ depends on the object only at the point B; moreover, the data point $g(\vec{s}_B, \xi_{max})$ also

depends only on B, where $\vec{s}_B = (\phi_B + \pi, R_0)$. Thus the symmetry,

$$g(\vec{r}_B, -\xi_{max}) = g(\vec{s}_B, \xi_{max}) \qquad (11)$$

follows. The potato peeler heuristing argument rests on this symmetry, and the fact that either data point can be used to determine B.

Conceptually, reconstruction, employing the data redundancy, proceeds by the repetition of three steps. First, each point on the outermost edge of the disk support is determined using the symmetry for the outermost points, i.e. points A, B, and C in Fig. 1. Second, each of these outermost points are forward projected individually back to the data space. Third, each point's contribution to the data is subtracted away from the data function. When the subtraction is performed for all of the outermost points, then the resulting new data function will be the forward projection corresponding to the object missing the outermost ring, exposing the next set of points toward the interior. In terms of Fig. 1, once the contribution of points A, B, and C are removed from the data function, point D is exposed on the outermost edge. These steps can be repeated until all points of the object are determined. The symmetry used in the first step applies to all points during the peeling procedure. Thus, we have data redundancy, and views covering 180° degrees are sufficient to determine the object function.
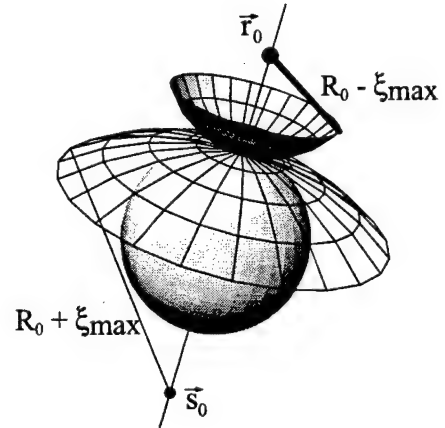

Fig. 2. Schematic of the three-dimensional object function for the heuristic potato peeler perspective. The illustrated integration surfaces from opposing views $\vec{r}_0$ and $\vec{s}_0$ intersect spherical support at one point.

B. 3D reflectivity tomography

The potato peeler perspective can be generalized to 3D reflectivity tomography in a straightforward manner. In this case the support of the object function is contained in a sphere of radius R_f shown in Fig. 2. Let the surface of integration be denoted by $S(\theta_0, \phi_0, \xi)$ where again $\xi \equiv \bar{t} - R_0$ represents the distance away from the center of the measurement sphere. Clearly, from Fig. 2, the surface $S(\theta_0, \phi_0, \xi_{max})$ intersects the support sphere at one point, and a symmetry analgous to Eq. (11) holds for points on the outermost shell, namely:

$$g(\vec{r}_0, -\xi_{max}) = g(\vec{s}_0, \xi_{max}), \qquad (12)$$

where $\vec{s}_0 = (\pi - \theta_0, \phi_0 + \pi, R_0)$. From this symmetry, the 3D version of the heuristic potato peeler perspective extends naturally from the 2D version. In the 3D argument the outermost shell of the object function is determined, making use of the symmetry in Eq. (12); only half of the views over 4π steradians are needed to specify all points on the outer shell. Again, the contribution of points in the outer shell can be subtracted away from the data, exposing the next shell toward the interior. From repeating the peeling, only 2π steradian coverage of the sphere is needed to determine the complete 3D object function.

V. NUMERICAL RESULTS

We performed computer-simulation studies to validate that accurate images can be reconstructed from reduced-scan data in 3D reflectivity tomography. A 3D Shepp-Logan phantom was used to generate the data function $g(\vec{r}_0; \bar{t})$. For a given R_0, which is the distance between the center of rotation and transducer, $g(\vec{r}_0; \bar{t})$ is a function of variables θ_0, ϕ_0, and $\bar{t}$, where $0 \leq \theta_0 \leq \pi$ and $0 \leq \phi_0 \leq 2\pi$ specify the direction of measurements, and $\bar{t} \in [0, R_0 + R_f]$ identifies the time of measurements to a location. We divided the data space $\{\theta_0, \phi_0, \bar{t}\}$ into a $60 \times 120 \times 128$ uniform lattice and generated full-scan data on this lattice for $R_0 = 30$ cm.

Since the data function in Eq. (7) is non-negative, the iterative expectation-maximization (EM) algorithm can be applied to reconstruct the image. We used the EM algorithm for image reconstruction, because it is unclear whether non-iterative algorithms exist for exact reconstruction of images from reduced-scan data. For the purpose of comparison, we also used the EM algorithm for image reconstruction from full-scan data. In an attempt to increase the convergence speed of the EM algorithm, we used the ordered-subsets EM (OSEM) for image reconstruction from both full-scan and reduced-scan in our simulation studies. The data set was divided into 5 subsets along θ dimension, and the OSEM algorithm was parallelized for different ϕ values. We used 200 iterations for both reconstructions from the reduced-scan and full-scan data. The calculation was performed on the "Chiba City" cluster computer at the Mathematics and Computer Science Division in Argonne National Laboratory. With 60 processors, it took about 80 and 40 hours to reconstruct

3D images of 128^3 voxels from the full-scan and half-scan data, respectively.

We show in Fig. 3 2D images at $x = 0$ cm (left), $y = 0$ cm (middle), and $z = -2.5$ cm (right) in the reconstructed 3D images. The original images are shown in the top row, and the images in middle and bottom rows were obtained from the full-scan and half-scan data, respectively. In Fig. 4, we show the profiles along the central, vertical axis of images in the third column in Fig. 3. As these results show, one can reconstruct 3D images from half-scan data with quantitative accuracy comparable to that of 3D images reconstructed from full-scan data.
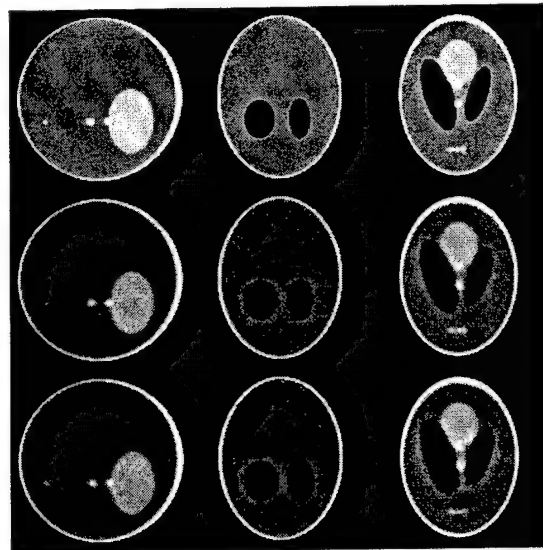

Fig. 3. 2D images at $x = 0$ cm (left), $y = 0$ cm (middle), and $z = -2.5$ cm (right) in the 3D Shepp-Logan image. The original images are shown in the top row. The images reconstructed from full-scan and half-scan data are displayed in the middle and bottom rows, respectively.
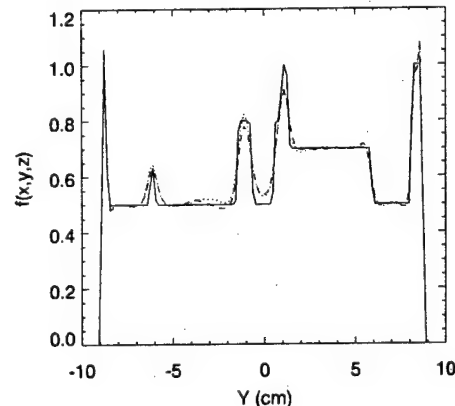

Fig. 4. Original profile (solid curve), profile in images obtained from full-scan (dotted curve) and half-scan (dashed curve) data. Profile along the central vertical axes in images shown in the third column in Fig. 3.

VI. DISCUSSION

We investigated image reconstruction in 3D reflectivity tomography. Motivated by the potato-peeler perspective that we developed for image reconstruction from reduced-scan data in 2D reflectivity tomography, we proposed a potato-peeler perspective for identifying symmetry and redundant information in data function in 3D reflectivity tomography. Such redundant information can be exploited for accurate reconstruction 3D reflectivity images from reduced-scan data. We conducted computer simulation studies, and results in these studies quantitatively suggest that 3D reflectivity tomography can accurately be reconstructed from reduced-scan data. In many applications of reflectivity tomography, it is not feasible to collect full-scan data. Therefore, the practical implication of reflectivity tomography with a reduced-scan configuration can be significant. For example, when imaging breast cancer, although only reduced-scan measurements acquired over a hemisphere can be obtained, our results presented here suggest that such data may contain complete information for accurate reconstruction of 3D breast images. We also applied the microlocal analysis [15] to demonstrate the stability of reconstructing image boundaries from reduced-scan data and will report such results at the meeting. It is interesting to note that our observations regarding the stability of the reduced-scan reflectivity tomography reconstruction problem can be related readily to a similar analysis of the limited-view thermoacoustic CT problem [9].

VII. ACKNOWLEDGMENT

REFERENCES

[1] S. Norton. Reconstruction of a two-dimensional reflecting medium over a circular domain: Exact solution. *Journal of the Acoustical Society of America*, 67(4):1266–1273, 1980.

[2] S. Norton and M. Linzer. Ultrasonic reflectivity imaging in three dimensions: Exact inverse scattering solutions for plane, cylindrical, and spherical apertures. *IEEE Transactions on Biomedical Engineering*, 28:202–220, 1981.

[3] J. Ylitalo, J. Kaovukangas, and J. Oksman. Ultrasonic reflection mode computed tomography through a skullbone. *IEEE Transactions on Biomedical Engineering*, 37:1059–1065, 1990.

[4] K. Dines and A. Goss. Computer ultrasonic reflection tomography. *IEEE Transactions on Ultrasonics, Ferroelectrics and Frequency Control*, 34:309–317, 1987.

[5] M. Xu and L. Wang. Time-domain reconstruction for thermoacoustic tomography in a spherical geometry. *IEEE Transactions on Medical Imaging*, 21:814–822, 2002.

[6] D. Parker. Optimal short scan convolution reconstruction for fanbeam CT. *Medical Physics*, 9:254–257, 1982.

[7] F. Noo and J. Wagner. Image reconstruction in 2D SPECT with 180° acquisition. *Inverse Problems*, 17:1357–1371, 2001.

[8] S. Norton and M. Linzer. Ultrasonic reflectivity imaging in three dimensions: Reconstruction with spherical transducer arrays. *Ultrasonic Imaging*, 1:210–231, 1979.

[9] M. Xu and L. Wang. Limited-view thermoacoustic tomography. In *Proceedings of the Second Joint EMBS/BMES Conference*, volume 2, pages 937–938, 2002.

[10] X. Pan, E. Y. Sidky, C. Kao, Y. Zou, and C. E. Metz. Image reconstruction in π-scheme SPECT with non-uniform attenuation. *IEEE Transactions on Nuclear Science*, (accepted), 2003.

[11] X. Pan, E. Y. Sidky, C.-M. Kao, Y. Zou, and C. E. Metz. Image reconstruction in SPECT with non-uniform attenuation and 3D distance-dependent spatial resolution. *Phys. Med. Biol.*, 47:2811–2833, 2002.

[12] E. Y. Sidky and X. Pan. Variable Sinograms and Redundant Information in SPECT with Non-uniform Attenuation. *Inverse Problems*, 18:1483–1497, 2002.

[13] E. Y. Sidky and X. Pan. Image Reconstruction with a Half-Detector in SPECT with Non-uniform Attenuation. *Optical Engineering*, (submitted).

[14] X. Pan, Y. Zou, and M. Anastasio. Data redundany and reduced-scan reconstruction in reflectivity tomography. *IEEE Transactions on Image Processing*, (accepted), 2003.

[15] A. K. Louis and E. T. Quinto. Local tomographic methods in SONAR. In *Surveys on Solution Methods for Inverse Problems*. Springer-Verlag, To appear (2003).

Full- and minimal-scan reconstruction algorithms for fan-beam diffraction tomography

Mark A. Anastasio and Xiaochuan Pan

Diffraction tomography (DT) is a tomographic inversion technique that reconstructs the spatially variant refractive-index distribution of a scattering object. In fan-beam DT, the interrogating radiation is not a plane wave but rather a cylindrical wave front emanating from a line source located a finite distance from the scattering object. We reveal and examine the redundant information that is inherent in the fan-beam DT data function. Such redundant information can be exploited to reduce the reconstructed image variance or, alternatively, to reduce the angular scanning requirements of the fan-beam DT experiment. We develop novel filtered backpropagation and estimate–combination reconstruction algorithms for full-scan and minimal-scan fan-beam DT. The full-scan algorithms utilize measurements taken over the angular range $0 \leq \phi \leq 2\pi$, whereas the minimal-scan reconstruction algorithms utilize only measurements taken over the angular range $0 \leq \phi \leq \phi_{min}$, where $\pi \leq \phi_{min} \leq 3\pi/2$ is a specified function that describes the fan-beam geometry. We demonstrate that the full- and minimal-scan fan-beam algorithms are mathematically equivalent. An implementation of the algorithms and numerical results obtained with noiseless and noisy simulated data are presented. © 2001 Optical Society of America

OCIS codes: 100.3190, 100.3010, 100.6950.

1. Introduction

Diffraction tomography (DT) is an inversion scheme that can be used for obtaining the spatially variant refractive-index distribution of a scattering object. Applications of DT can be found in various scientific fields such as medical imaging,[1,2] nondestructive evaluation of materials,[3,4] and geophysics.[5,6] Unlike the x rays used in computed tomography (CT), the optical or acoustical wave fields employed in DT do not generally travel along straight lines, thus precluding the use of the geometrical optics approximation. Therefore a wide variety of techniques that are suitable for reconstruction of CT images cannot be used directly for reconstruction of diffraction tomographic images. CT can be viewed as a limiting case of DT, in which the frequency of the probing radiation tends toward infinity.

A vast majority of the algorithm development ef-

forts in DT have utilized the classic scanning geometry,[7] which assumes that the interrogating radiation is plane wave and the transmitted scattered wave field is measured in a plane (or in two dimensions, along a line) on the opposite side of the scattering object. This geometry is analogous to the parallel-beam geometry of x-ray CT. In many practical situations, however, the interrogating radiation may be not plane wave but rather produced by a line source located a finite distance from the scattering object. We refer to this configuration as the fan-beam geometry of DT,[8] which is somewhat analogous to the two-dimensional (2D) fan-beam geometry of CT.

The Born and Rytov approximations[9] are weak-scattering approximations that effectively linearize the inhomogeneous Helmholtz and Ricatti equations, respectively. The relative merits of the Born and Rytov approximations in the context of DT have been widely explored in the literature.[10,11] Under weak-scattering conditions it is customary and useful in DT to invoke the Born or Rytov approximation that permits the derivation of the Fourier diffraction projection (FDP) theorem. The FDP theorem relates the one-dimensional (1D) Fourier transform of the measured scattered data to the 2D Fourier transform of the scattering object. For 2D DT employing plane-wave illumination and the classic scan configuration, Devaney[7] utilized the FDP theorem to develop the

M. A. Anastasio and X. Pan (x-pan@uchicago.edu) are with the Graduate Program in Medical Physics, Department of Radiology, University of Chicago, 5841 South Maryland Avenue, Chicago, Illinois 60637.

well-known filtered backpropagation (FBPP) algorithm, which can be viewed as a generalization of the conventional filtered backprojection (FBPJ) algorithm of x-ray CT. Alternative families of plane-wave DT reconstruction algorithms, referred to as estimate–combination (E-C) algorithms and generalized FBPP algorithms, have been developed[12] and investigated.[13,14] The family of plane-wave E-C algorithms effectively operates by transforming (in 2D Fourier space) the DT problem into a 2D Radon transform problem that can be efficiently and stably inverted by use of the FBPJ algorithm. The family of plane-wave generalized FBPP algorithms reconstructs the image directly from the DT data function and includes the FBPP algorithm as a special member. Both the generalized FBPP and E-C algorithms generally require scattered data measured from view angles in $[0, 2\pi)$ to perform an exact reconstruction of a complex-valued scattering object. Accordingly, we refer to these algorithms as being full-scan algorithms.

Previously we showed[15] that, in plane-wave DT that employs the 2D classic scanning geometry, a minimal-scan data set acquired by use of view angles only in $[0, \phi_{min} = 3\pi/2]$ contains all the information necessary for exact reconstruction of the scattering object function. As the frequency of the probing radiation tends toward infinity, $\phi_{min} \to \pi$, which reflects the well-known fact that measurements corresponding to $\phi \in [0, \pi]$ completely specify the 2D Radon transform. [Of course, compactly supported objects are mathematically specified by a sinogram $p(\xi, \phi_0)$, where ϕ_0 is contained in any open set $[0, \epsilon)$, but if $p(\xi, \phi_0)$ is not continuously sampled this observation does not yield stable reconstruction algorithms.] We subsequently developed minimal-scan FBPP[15] and minimal-scan E-C[16] algorithms that were capable of reconstructing the scattering object function by use of the minimal-scan data set. Under the conditions of continuous sampling and in the absence of noise, we demonstrated[16] that the minimal-scan FBPP and E-C reconstruction algorithms were mathematically equivalent to the full-scan FBPP and E-C reconstruction algorithms, respectively.

Here we reveal and examine the redundant information that is inherent in the fan-beam DT data function. Such redundant information can be exploited to reduce the noise in the reconstructed image or, alternatively, to reduce the angular scanning requirements of the fan-beam DT experiment. We develop novel E-C and FBPP reconstruction algorithms for full-scan and minimal-scan fan-beam DT. We demonstrate that the minimal-scan algorithms, which utilize measurements taken over the angular range $0 \le \phi \le \phi_{min}$, where $\pi \le \phi_{min} \le 3\pi/2$, are mathematically equivalent to their full-scan counterparts that utilize measurements over the full angular range $0 \le \phi \le 2\pi$. An implementation of the algorithms and numerical results obtained with noiseless and with noisy simulated data are presented.
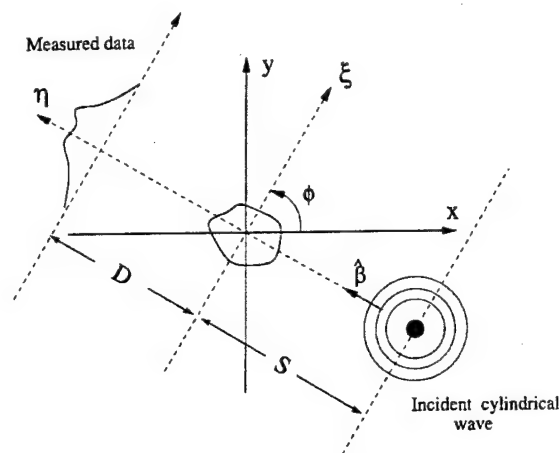

Fig. 1. Fan-beam scanning geometry of 2D DT. The interrogating cylindrical wave propagates along the η axis, and the scattered wave field is measured along the line $\eta = l$. We obtain full-scan and minimal-scan data sets by varying the measurement angle ϕ between 0 and 2π or between 0 and ϕ_{min} [see Eq. (29)], respectively. We assume that S and D are much larger than the transverse dimension of the scattering object.

2. Background

Here we briefly review the geometry and approximations that are traditionally employed in fan-beam DT, as described in the pioneering work of Devaney.[8] A table of the acronyms used in this manuscript is included in Appendix A.

A. Fan-Beam Diffraction Tomography

The classic scanning configuration of fan-beam DT is shown in Fig. 1. The fixed coordinate system (x, y), the rotated coordinate system (ξ, η), and the usual polar coordinates (r, θ) are related by $x = r \cos \theta$, $y = r \sin \theta$, $\xi = x \cos \phi + y \sin \phi = r \cos (\phi - \theta)$, and $\eta = -x \sin \phi + y \cos \phi = -r \sin(\phi - \theta)$. The scattering object is illuminated by a monochromatic cylindrical-wave source located at the position $\eta = -S$ on the η axis, emitting a wave field of the form

$$u_i(\xi, \phi) = U_0 \frac{\exp(j2\pi\nu_0|\mathbf{r} - S\hat{\beta}|)}{|\mathbf{r} - S\hat{\beta}|}$$
$$= U_0 \frac{\exp\{j2\pi\nu_0[\xi^2 + (S + D)^2]^{1/2}\}}{[\xi^2 + (S + D)^2]^{1/2}}, \quad (1)$$

where U_0 is the complex amplitude, $k = 2\pi\nu_0$ is the wave number, $\hat{\beta}$ is a unit vector pointing along the positive η axis, and D is the distance of the detector surface from the center of rotation. The incident wave field $u_i(\xi, \phi)$ could represent a pressure field in acoustical applications or a scalar electromagnetic field in optical applications, for example. From measurements of the scattered wave field obtained along the ξ axis oriented at a measurement angle ϕ at a distance $\eta = D$ from the origin, one seeks to reconstruct the scattering object function $a(\mathbf{r})$. The underlying physical property of the scattering object that is mapped in DT is the refractive-index distri-

bution $n(\mathbf{r})$, which is related to the scattering object function by the equation $a(\mathbf{r}) = n^2(\mathbf{r}) - 1$.

Let $u(\xi, \phi)$ denote the measured total wave field along the line $\eta = D$, as shown in Fig. 1. The scattered data are given by

$$u_s(\xi, \phi) = u(\xi, \phi) - u_i(\xi, \phi), \tag{2}$$

which can be treated as a measurable data function because $u(\xi, \phi)$ and $u_i(\xi, \phi)$ can be measured. Therefore we can introduce a modified data function $M(\nu_m, \phi)$, which is given by

$$M(\nu_m, \phi) = \frac{\chi}{\pi \nu_0^2} \nu' \exp[-j2\pi(\nu' - \nu_0)D]$$
$$\times \mathscr{F}_{\nu_m}\left\{\frac{u_s(\xi, \phi)}{u_i(\xi, \phi)}\right\}, \tag{3}$$

where

$$\mathscr{F}_{\nu_m}\{h(\xi)\} = (1/2\pi)\int_{-\infty}^{\infty} h(\xi)\exp(-j2\pi\nu_m\xi)\mathrm{d}\xi,$$

$$\chi = \sqrt{\frac{S}{S + D}}, \tag{4}$$

$$\nu' = \sqrt{\nu_0^2 - \frac{\nu_m^2}{\chi^2}}. \tag{5}$$

B. Fan-Beam Fourier Diffraction Projection Theorem

In plane-wave DT, the FDP theorem[17] relates the modified data function to the 2D Fourier transform of the scattering object and can be viewed as a generalization of the Fourier slice theorem of conventional x-ray CT. The FDP theorem is valid under conditions of weak scattering and plane-wave illumination. To establish the FDP theorem for the fan-beam DT geometry it is necessary to assume the weak-scattering approximation and the so-called paraxial approximation,[8] which is a well-known approximation in the optics literature. The paraxial approximation requires that both S and D be much larger than the dimension size of the scattering object. This amounts to requiring that the largest angle subtended by the object when the object is viewed from either the source or the measurement location be much smaller than a radian.

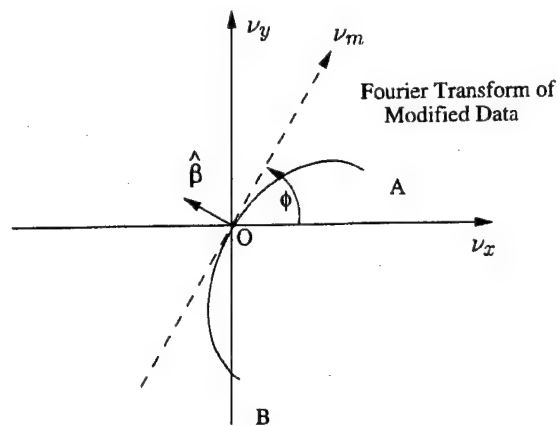Under the Born and paraxial approximations, Devaney derived the fan-beam FDP theorem,[8] which is given by

Fig. 2. The fan-beam FDP theorem states that $M(\nu_m, \phi)$ is equal to the 2D Fourier transform of $a(\mathbf{r})$ along the semielliptic arc AOB that has semiaxes equal to ν_0 and ν_0/χ.

As displayed in Fig. 2, Eq. (6) states that the modified data function, $M(\nu_m, \phi)$, is equal to a semielliptical slice, oriented at angle ϕ, through the 2D Fourier transform of the object function $a(\mathbf{r})$. One can also derive the FDP theorem by employing the Rytov approximation instead of the Born approximation. In this case, Eq. (6) remains unchanged and only Eq. (3) needs to be appropriately redefined.[8]

3. Full-Scan Reconstruction Algorithms for Fan-Beam Diffraction Tomography

First, we present families of full-scan FBPP and E-C reconstruction algorithms for fan-beam DT. These fan-beam algorithms are novel and contain the previously developed families of plane-wave FBPP and E-C algorithms as limiting cases. They will be generalized to the minimal-scan situation in Section 4 below.

A. Fan-Beam Full-Scan Estimate–Combination Algorithms

The Radon transform[18] of the scattering object function $a(r, \theta)$ is defined as

$$p(\xi, \phi_0) = \int_{-\infty}^{\infty}\int_{-\infty}^{\infty} a(r, \theta)\delta[\xi - r\cos(\phi_0 - \theta)]\mathrm{d}\mathbf{r}, \tag{7}$$

where ϕ_0 is the projection angle, $\xi = r\cos(\phi_0 - \theta)$, and $\eta = -r\sin(\phi_0 - \theta)$. The 2D Fourier transform of $p(\xi, \phi_0)$ is defined as [strictly speaking, $P_k(\nu_a)$ is the com-

$$M(\nu_m, \phi) = \int_{-\infty}^{\infty}\int_{-\infty}^{\infty} a(\mathbf{r})\exp\left\{-j2\pi\left[\frac{\nu_m}{\chi^2}\xi - (\nu' - \nu_0)\eta\right]\right\}\mathrm{d}\mathbf{r} \qquad |\nu_m| \le \chi\nu_0,$$
$$= 0 \qquad\qquad\qquad\qquad\qquad\qquad\qquad\qquad\qquad\qquad |\nu_m| > \chi\nu_0. \tag{6}$$

bination of the 1D Fourier transform with respect to v_a and a 1D Fourier series expansion with respect to ϕ_0 of the Radon transform]

$$P_k(v_a) = \frac{1}{2\pi} \int_0^{2\pi} \int_{-\infty}^{\infty} p(\xi, \phi_0)$$
$$\times \exp[-j2\pi v_a\xi - jk\phi_0]d\xi d\phi_0, \qquad (8)$$

where v_a is the spatial frequency with respect to ξ and the integer k is the angular frequency index with respect to ϕ_0. It is well known that $a(r, \theta)$ can readily be reconstructed exactly from its Radon transform $p(\xi, \phi_0)$ [or, equivalently, $P_k(v_a)$] by use of a wide variety of computationally efficient and numerically stable reconstruction algorithms such as the FBPJ algorithm. Therefore the task of image reconstruction in fan-beam DT is tantamount to the task of estimating $P_k(v_a)$. Furthermore, because $P_k(v_a)$ for $v_a \geq 0$ contains full knowledge of the Radon transform, one needs to estimate $P_k(v_a)$ from the measured scattered data only for $v_a \geq 0$.

Comparison of Eqs. (9) and (11) yields that, for $|v_m| \leq \chi v_0$,

$$P_k(v_a) = \gamma(v_m/\chi^2)^k M_k(v_m), \qquad (13)$$

provided that

$$v_a{}^2 = \left(\frac{v_m}{\chi^2}\right)^2 + \left\{\left[v_0{}^2 - \left(\frac{v_m}{\chi}\right)^2\right]^{1/2} - v_0\right\}^2. \quad (14)$$

From Eq. (14) we see that v_a is real (that is, $0 \leq v_a \leq v_0\sqrt{1 + 1/\chi^2}$) only for $|v_m| \leq \chi v_0$.

In the absence of data noise or inconsistencies, one can use Eq. (13) to obtain $P_k(v_a)$ exactly from $M_k(v_m)$, which can readily be obtained from the modified data function. In the presence of data noise or inconsistencies, one can use Eq. (13) to obtain an estimate of $P_k(v_a)$. For any given $0 \leq v_a \leq v_0\sqrt{1 + 1/\chi^2}$, we show in Appendix B that four different roots $v_{mi}, i = 1, 2, 3, 4$, satisfy Eq. (14). However, only two of these four roots correspond to real-valued frequencies, which are given by

$$v_{m1} = -v_{m2} = v_m = v_a\left(1 - \frac{v_a{}^2}{4v_0{}^2}\right)^{1/2}\left(\frac{\chi^4}{\frac{1}{2}\{1 - (1 - \chi^2)(v_a{}^2/2v_0{}^2) + [1 - \chi^2(1 - \chi^2)(v_a{}^2/v_0{}^2)]^{1/2}\}}\right)^{1/2} \qquad (15)$$

From Eqs. (7) and (8) it can be shown[19] that

$$P_k(v_a) = (-j)^k \int_{\theta=0}^{2\pi} \int_{r=0}^{\infty} a(\mathbf{r})$$
$$\times \exp(-jk\theta)J_k(2\pi v_a r)r dr d\theta, \qquad (9)$$

where J_k indicates the kth-order Bessel function of the first kind. Because $M(v_m, \phi)$ is a periodic function of ϕ, it can be expanded into a Fourier series with expansion coefficients given by

$$M_k(v_m) = \frac{1}{2\pi} \int_0^{2\pi} M(v_m, \phi)\exp(-jk\phi)d\phi. \quad (10)$$

Substituting Eq. (6) into Eq. (10), noting that $\xi = r\cos(\phi - \theta)$ and $\eta = -r\sin(\phi - \theta)$, and carrying out the integration over angle ϕ (Ref. 19) yield

In the plane-wave case there are only two roots,[12] which one can obtain from Eq. (15) by letting $\chi = 1$.

Therefore, for a given $0 \leq v_a \leq v_0(1 + 1/\chi^2)^{1/2}$, one can obtain two estimates of $P_k(v_a)$ from knowledge of $M_k(v_m)$ at v_{m1} and v_{m2}, namely,

$$P_k(v_a) = \left[\gamma\left(\frac{v_{m1}}{\chi^2}\right)\right]^k M_k(v_{m1}) = \left[\gamma\left(\frac{v_m}{\chi^2}\right)\right]^k M_k(v_m),$$
$$\qquad (16)$$

$$P_k(v_a) = \left[\gamma\left(\frac{v_{m2}}{\chi^2}\right)\right]^k M_k(v_{m2})$$
$$= (-1)^k\left[\gamma\left(\frac{v_m}{\chi^2}\right)\right]^{-k} M_k(-v_m). \qquad (17)$$

In establishing Eq. (17) we used the property $\gamma(-v_m') = -\gamma(v_m')^{-1}$. It can readily be shown that, as the

$$M_k(v_m) = (-j)^k\gamma(v_m')^{-k} \int_{r=0}^{\infty} \int_{\theta=0}^{2\pi} a(\mathbf{r})\exp(-jk\theta)J_k(2\pi r\sqrt{v_m'^2 - v_\mu{}^2})r dr d\theta \qquad |v_m| \leq \chi v_0,$$
$$= 0 \qquad\qquad |v_m| > \chi v_0, \qquad (11)$$

where $v_m' = v_m/\chi^2$, $v_\mu = j(v' - v_0)$, and

$$\gamma(v_m') = \frac{\sqrt{v_m'^2 - v_\mu{}^2}}{v_m' + v_\mu}. \qquad (12)$$

incident wave becomes planar (i.e., as $\chi \to 1$), the above results become the results in Ref. 12 for the plane-wave case.

In the absence of noise, Eqs. (16) and (17) yield identical (and exact) values of $P_k(v_a)$. In the presence of data noise (or other inconsistencies), the two

estimates of $P_k(\nu_a)$ are distinct, suggesting that it may be beneficial to combine the two estimates linearly[12] to form a final estimate of $P_k(\nu_a)$ as

$$P_k(\nu_a) = \omega_k(\nu_m)[\gamma^k M_k(\nu_m)]$$
$$+ [1 - \omega_k(\nu_m)][(-1)^k \gamma^{-k} M_k(-\nu_m)], \quad (18)$$

where $\omega_k(\nu_m)$ is a combination coefficient that dictates how Eqs. (16) and (17) are combined. This strategy of linear combination has been demonstrated to be useful in reducing the noise in the reconstructed image.[12-14] Because each selection of $\omega_k(\nu_m)$ gives rise to a particular final estimate $P_k(\nu_a)$, Eq. (18) can be interpreted as an estimation method for obtaining $P_k(\nu_a)$ (or, equivalently, the Radon transform). Because $\omega_k(\nu_m)$ may be any complex-valued function of ν_m and k, Eq. (18), in effect, provides infinite families of estimation methods. From the estimate $P_k(\nu_a)$ (i.e., the Radon transform), one can subsequently reconstruct the image $a(\mathbf{r})$ by use of the FBPJ algorithm. For simplicity, the use of Eq. (18) to estimate $P_k(\nu_a)$ coupled with the 2D FBPJ algorithm to reconstruct $a(\mathbf{r})$ is referred to as a fan-beam full-scan E-C reconstruction algorithm. As $S \to \infty$, we observe that $\chi \to 1$ and that the fan-beam full-scan E-C reconstruction algorithms reduce to the plane-wave full-scan E-C reconstruction algorithms developed previously.[12]

B. Fan-Beam Full-Scan Filtered Backpropagation Algorithms

The fan-beam full-scan E-C algorithms discussed above first estimate $P_k(\nu_a)$ (i.e., the Radon transform) from the modified data function $M_k(\nu_m)$ and subsequently reconstruct the image by inverting the estimated Radon transform. Below, we develop algorithms that reconstruct images directly from the modified data function. Using Eq. (9), one can directly express the object function in terms of the estimate $P_k(\nu_a)$ as

$$a(\mathbf{r}) = 2\pi \sum_{k=-\infty}^{\infty} j^k \int_{\nu_a=0}^{\infty} P_k(\nu_a)$$
$$\times \exp(jk\theta) J_k(2\pi\nu_a r)\nu_a \mathrm{d}\nu_a. \quad (19)$$

Substituting Eq. (18) into Eq. (19) yields

$$a(\mathbf{r}) = 2\pi \sum_{k=-\infty}^{\infty} j^k \exp(jk\theta) \int_{\nu_a=0}^{\nu_0\sqrt{1+1/\chi^2}} \{\omega_k(\nu_m)\gamma^k M_k(\nu_m)$$
$$+ [1 - \omega_k(\nu_m)](-1)^k\gamma^{-k}M_k(-\nu_m)\}J_k(2\pi\nu_a r)\nu_a \mathrm{d}\nu_a.$$
$$(20)$$

Using the relationship between ν_a and ν_m in Eq. (14), one can show that, for $0 \leq \nu_a \leq \nu_0\sqrt{1+1/\chi^2}$,

$$\nu_a \mathrm{d}\nu_a = \frac{\nu_m'\mathrm{d}\nu_m'}{\nu'} [(1 - \chi^2)\nu' + \chi^2\nu_0]. \quad (21)$$

Substituting this result into Eq. (20), and noting that $\nu_m' = \nu_m/\chi^2$, yields

$$a(\mathbf{r}) = \pi \sum_{k=-\infty}^{\infty} j^k \exp(jk\theta) \int_{\nu_m=0}^{\chi\nu_0} \frac{\nu_m}{\chi^4\nu'} [(1 - \chi^2)\nu'$$
$$+ \chi^2\nu_0]\{\omega_k(\nu_m)\gamma^k M_k(\nu_m) + [1 - \omega_k(\nu_m)]$$
$$\times (-1)^k\gamma^{-k}M_k(-\nu_m)\}$$
$$\times J_k[2\pi(\nu_m'^2 - \nu_\mu^2 r)^{1/2}]\mathrm{d}\nu_m. \quad (22)$$

To reduce Eq. (22) to the form of the FBPP algorithm, we assume that $\omega_k(\nu_m) + \omega_k(-\nu_m) = 1$. Using the integral identities[12]

$$(\pm)^k j^k \gamma(\nu_m')^{\pm k} \exp(jk\theta) J_k[2\pi(\nu_m'^2 - \nu_\mu^2 r)^{1/2}]$$
$$= \frac{1}{2\pi} \int_0^{2\pi} \exp\left[jk\phi \pm j2\pi\nu_m \frac{\xi}{\chi^2} + 2\pi\nu_\mu\eta\right]\mathrm{d}\phi \quad (23)$$

and defining

$$M^{(\omega)}(\nu_m, \phi) = \sum_{k=-\infty}^{\infty} \exp(jk\phi)\omega_k(\nu_m) M_k(\nu_m) \quad (24)$$

yield for Eq. (22)

$$a(\mathbf{r}) = \frac{1}{2} \int_0^{2\pi} \int_{-\chi\nu_0}^{\chi\nu_0} \frac{|\nu_m|}{\chi^4\nu'} [(1 - \chi^2)\nu' + \chi^2\nu_0]M^{(\omega)}(\nu_m, \phi)$$
$$\times \exp\left[j2\pi\nu_m \frac{\xi}{\chi^2} + 2\pi\nu_\mu\eta\right]\mathrm{d}\phi\mathrm{d}\nu_m. \quad (25)$$

Equation (25) describes a family of fan-beam full-scan FBPP algorithms [indexed by the choice of $\omega_k(\nu_m)$], which becomes the family of FBPP algorithms for plane-wave full-scan DT[12] when $\chi \to 1$. In particular, when $\omega_k(\nu_m) = 1/2$, Eq. (25) corresponds to the fan-beam FBPP algorithm suggested by Devaney.[8] Because the derivation of the family of fan-beam full-scan FBPP algorithms was based on the family of fan-beam full-scan E-C algorithms [Eq. (20)], the E-C and FBPP algorithms are mathematically equivalent. However, as will be demonstrated below, these FBPP and E-C algorithms respond differently to data noise and other experimental errors.

4. Minimal-Scan Reconstruction Algorithms for Fan-Beam Diffraction Tomography

As discussed above, the redundant information contained in the scattered data can be employed for reducing the image noise. Such information can also be used for reducing the angular scanning requirements in a DT experiment.

A. Consistency Conditions and the Fan-Beam Data Space

According to the fan-beam FDP theorem in Eq. (6), the modified data function $M(\nu_m, \phi)$ satisfies the consistency condition

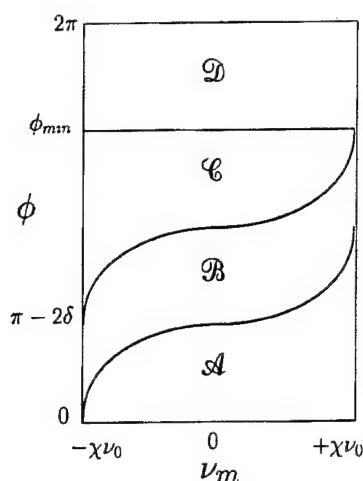$$M(\nu_m, \phi) = M(-\nu_m, \phi + \pi - 2\alpha), \quad (26)$$

Fig. 3. Complete data space $\mathcal{W} = \mathcal{A} \cup \mathcal{B} \cup \mathcal{C} \cup \mathcal{D}$ contains data from the view angles in $[0, 2\pi]$. Subset $\mathcal{M} = \cup \mathcal{A} \cup \mathcal{B} \cup \mathcal{C}$ obtained from the view angles in $[0, \phi_{\min}]$ is called the minimal-complete data set. The minimal-complete data set contains all the information necessary for exact reconstruction of the scattering object function.

where

$$\sin \alpha = \mathrm{sgn}(\nu_m) \left[\frac{(\nu' - \nu_0)^2}{(\nu_m{}^2/\chi^2) + (\nu' - \nu_0)^2} \right]^{1/2}. \quad (27)$$

Let $\mathcal{W} = [|\nu_m| \leq \chi\nu_0, 0 \leq \phi \leq 2\pi]$ denote the complete (or full-scan) data set. As shown in Fig. 3, $\mathcal{W}$ can be divided into the four subspaces, $\mathcal{A}$, $\mathcal{B}$, $\mathcal{C}$, and $\mathcal{D}$, where

$$\mathcal{A} = [|\nu_m| \leq \chi\nu_0, \ 0 \leq \phi \leq 2\alpha + 2\delta],$$

$$\mathcal{B} = [|\nu_m| \leq \chi\nu_0, \ 2\alpha + 2\delta \leq \phi \leq \pi + 2\alpha],$$

$$\mathcal{C} = [|\nu_m| \leq \chi\nu_0, \ \pi + 2\alpha \leq \phi \leq \phi_{\min}],$$

$$\mathcal{D} = [|\nu_m| \leq \chi\nu_0, \ \phi_{\min} \leq \phi \leq 2\pi],$$

where

$$\sin \delta = \frac{1}{(1 + 1/\chi^2)^{1/2}}, \qquad \phi_{\min} = \pi + 2\delta. \quad (28)$$

Using Eqs. (26) and (27), one can verify that information in subspace $\mathcal{C}$ is identical to that in subspace $\mathcal{A}$ and that information in subspace $\mathcal{B}$ is identical to that in subspace $\mathcal{D}$. As shown in Fig. 3, because the boundaries between the subspaces are generally functions of ν_m and ϕ and because each horizontal line in $\mathcal{W}$ corresponds to a measurement acquired at a particular view angle, the information in subspace $\mathcal{B}$ cannot in practice be determined independently of that in subspace $\mathcal{C}$ and vice versa. We therefore refer to the union, $\mathcal{M} = \mathcal{A} \cup \mathcal{B} \cup \mathcal{C} = [|\nu_m| \leq \chi\nu_0, 0 \leq \phi \leq \phi_{\min}]$, as the minimal-complete data set. A plot of $\phi_{\min}$ versus χ is shown in Fig. 4. As $\chi \to 1$, $\phi_{\min} \to 3\pi/2$, and $\mathcal{M}$ reduces to the minimal-complete data set proposed previously for plane-wave DT.[15] However, for $\chi < 1$, $\phi_{\min} < 3\pi/2$, which indicates that the
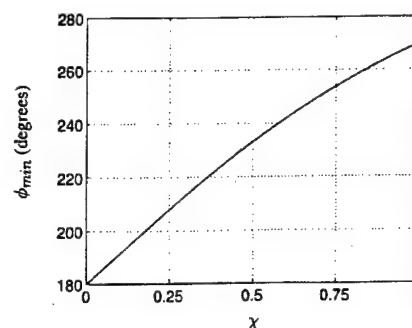

Fig. 4. Plot of $\phi_{\min}$ versus χ reveals that, in fan-beam DT, the required angular scanning range is less than 270°.

angular scanning requirements of fan-beam DT are less restrictive than for plane-wave DT.

Figure 5 clearly demonstrates that the minimal-complete data set contains all the information required for an exact reconstruction. According to the FDP theorem, the segment AOB corresponds to a semielliptical slice through the 2D Fourier transform of $a(\mathbf{r})$, which can be obtained from the modified data function $M(\nu_m, \phi)$. The Fourier space coverages produced by the segments OA and OB as ϕ varies from 0 to $\phi_{\min}$ are shown in Figs. 5(a) and 5(b), respec-
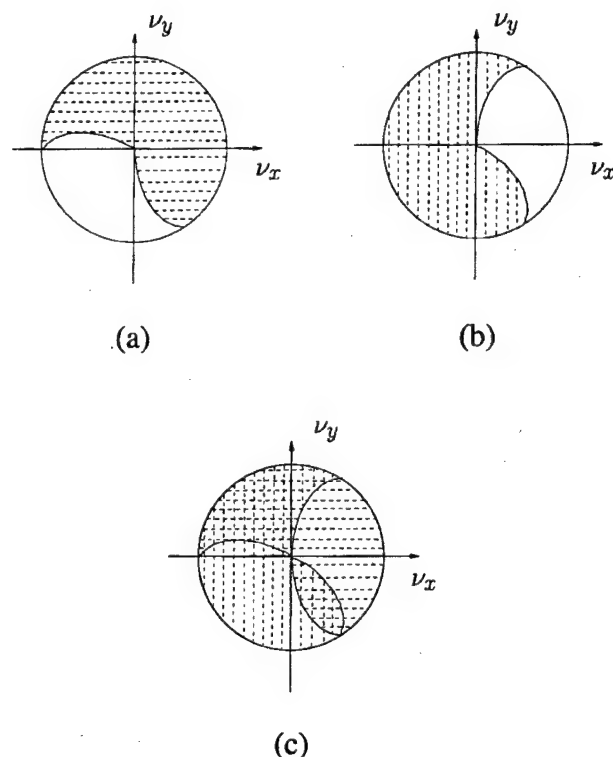

(a)   (b)

(c)

Fig. 5. As ϕ varies from 0 to $\phi_{\min}$, the two segments OA and OB (Fig. 2) yield two incomplete coverages of the 2D Fourier space of the object function, which are shown in (a) and (b), respectively. Superimposing the two incomplete coverages in (a) and (b), one obtains a complete coverage, as shown in (c), of the 2D Fourier space of the object function.

tively. It can be observed that each of these two coverages alone provides only an incomplete coverage of the 2D Fourier space of $a(\mathbf{r})$. However, one can superimpose these two incomplete coverages in Figs. 5(a) and 5(b) to obtain complete coverage of the 2D Fourier space of $a(\mathbf{r})$, as shown in Fig. 5(c).

The redundant information contained in subspaces $\mathcal{A}$ and $\mathcal{C}$ of the minimal-complete data set needs to be normalized properly before or during the reconstruction procedure. Let $M^{(m)}(\nu_m, \phi)$ denote the minimal scan data, where $M^{(m)}(\nu_m, \phi) = M(\nu_m, \phi)$ for $0 \leq \phi \leq \phi_{\min}$ and $M^{(m)}(\nu_m, \phi) = 0$ for $\phi_{\min} < \phi < 2\pi$. Consider a weighted data set $M'(\nu_m, \phi)$, defined as

$$M'(\nu_m, \phi) = w(\nu_m, \phi)M^{(m)}(\nu_m, \phi), \qquad (29)$$

where $w(\nu_m, \phi)$ can be a function of ν_m and ϕ that satisfies

$$w(\nu_m, \phi) + w(-\nu_m, \phi + \pi - 2\alpha) = 1 \qquad (30a)$$

in complete data space $\mathcal{W}$,

$$w(\nu_m, \phi) = 1 \qquad (30b)$$

in subspace $\mathcal{B}$, and

$$w(\nu_m, \phi) = 0 \qquad (30c)$$

in subspace $\mathcal{D}$. One can choose different $w(\nu_m, \phi)$ in subspaces $\mathcal{A}$ and $\mathcal{C}$ as long as these $w(\nu_m, \phi)$ satisfy Eq. 30(a). In the numerical examples that follow, we used the explicit form for $w(\nu_m, \phi)$ given by Eq. (38). We can now readily obtain minimal-scan reconstruction algorithms for fan-beam DT.

B. Fan-Beam Minimal-Scan Estimate–Combination Algorithms

Because of Eq. 30(c), Eq. (29) can also be rewritten as

$$M'(\nu_m, \phi) = w(\nu_m, \phi)M(\nu_m, \phi). \qquad (31)$$

Using Eqs. (26) and (30a), one can verify that

$$M(\nu_m, \phi) = M'(\nu_m, \phi) + M'(-\nu_m, \phi + \pi - 2\alpha). \qquad (32)$$

Using Eq. (32) in Eq. (10), one obtains

$$M_k(\nu_m) = [M_k'(\nu_m) + (-1)^k \gamma^{-2k} M_k'(-\nu_m)], \qquad (33)$$

where

$$M_k'(\nu_m) = (1/2\pi) \int_0^{2\pi} \exp(-jk\phi)M'(\nu_m, \phi)\mathrm{d}\phi.$$

Multiplying both sides of Eq. (33) by γ^k and noting Eq. (16), we conclude that, for $|\nu_m| \leq \chi\nu_0$,

$$P_k(\nu_a) = [\gamma^k M_k'(\nu_m) + (-1)^k \gamma^{-k} M_k'(-\nu_m)], \qquad (34)$$

where ν_a and ν_m are related by Eq. (14). A fan-beam minimal-scan E-C algorithm is formed by use of Eq. (34) to estimate the Radon transform from the minimal-complete data set acquired at measurement angles $0 \leq \phi \leq \phi_{\min}$ and the FBPJ algorithm to reconstruct the final image. One can form different
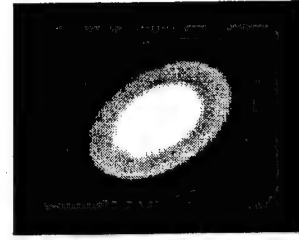

Fig. 6. The numerical phantom used in the simulation studies comprised two concentric ellipses. The fan-beam FDP theorem was used to calculate analytically the simulated scattered field data from the phantom.

fan-beam minimal-scan E-C algorithms by specifying different choices for $w(\nu_m, \phi)$ in Eq. (31) that satisfy Eqs. (30).

C. Fan-Beam Minimal-Scan Filtered Backpropagation Algorithms

Using Eq. (34) in Eq. (19) and using the strategy outlined in Subsection 3.B, we can also develop fan-beam minimal-scan FBPP algorithms that can reconstruct the object function directly from the weighted minimal-complete data set that is given by

$$a(\mathbf{r}) = \int_0^{\phi_{\min}} \int_{-\chi\nu_0}^{\chi\nu_0} \frac{|\nu_m|}{\chi^4 \nu'} \left[(1 - \chi^2)\nu' + \chi^2 \nu_0 \right] M'(\nu_m, \phi)$$

$$\times \exp\left[j2\pi\nu_m \frac{\xi}{\chi^2} + 2\pi\nu_\mu\eta \right] \mathrm{d}\phi\mathrm{d}\nu_m, \qquad (35)$$

where $\phi_{\min}$ is a function of χ as stated in Eq. (28). One can form different fan-beam minimal-scan FBPP algorithms by specifying different choices for $w(\nu_m, \phi)$ in Eq. (31) that satisfy Eqs. (30). When $\chi = 1$, the fan-beam minimal-scan FBPP algorithms reduce to the plane-wave minimal-scan FBPP algorithms derived previously.[15]

5. Numerical Results

We numerically investigated the fan-beam full- and minimal-scan reconstruction algorithms, using simulated noiseless and noisy data.

A. Data and Noise Model

We employed the numerical phantom composed of two concentric ellipses, as displayed in Fig. 6. The values of the scattering object function that correspond to the outer and inner ellipses are 0.0005 and 0.0001, respectively. We chose a fan-beam geometry specified by $\chi = 0.8$, but our observations below hold for arbitrary χ. The FDP theorem was employed to calculate analytically the modified data function $M(\nu_m, \phi)$ that by means of Eq. (3) determined the scattered field data $u_s(\xi, \phi)$. Therefore our simulations were designed to demonstrate the performance of the reconstruction algorithms under the condition that the Born and paraxial approximations are valid. The evaluation of the performance of the algorithms when the Born and paraxial approximations are not valid[10,11,20] remains a topic for future study. The

discrete complete data set comprised 128 equally spaced measurement angles in $[0, 2\pi)$. The discrete minimal-complete data set comprised 92 equally spaced measurement angles in $[0, 4.49)$ (or, equivalently, $[0, 257.3°)$). In this way, both data sets had the same angular sampling increment, $\Delta\phi = 2\pi/128 \approx 4.49/92$. The data function $M(\nu_m, \phi)$ contained 129 evenly spaced samples in $[-\chi\nu_0, \chi\nu_0]$.

To simulate the effects of data noise, we treated the scattered data $\mathbf{u}_s(\xi, \phi)$ as a complex stochastic process with a real and an imaginary component, denoted $\mathbf{u}_s^{(r)}(\xi, \phi)$ and $\mathbf{u}_s^{(i)}(\xi, \phi)$, respectively. (Here, boldface type for $\mathbf{u}$ and $\mathbf{a}$ denotes a random variable.) Let $\mathbf{u}_s^{(r)} = u_s^{(r)} + \Delta\mathbf{u}_s^{(r)}$ and $\mathbf{u}_s^{(i)} = u_s^{(i)} + \Delta\mathbf{u}_s^{(i)}$, where $u_s^{(r)}$ and $u_s^{(i)}$ are the means of $\mathbf{u}_s^{(r)}$ and $\mathbf{u}_s^{(i)}$, respectively. The statistics of the deviates $\Delta\mathbf{u}_s^{(r)}$ and $\Delta\mathbf{u}_s^{(i)}$ are described by the circular Gaussian model,

$$
p(\Delta u_s^{(r)}, \Delta u_s^{(i)}) = \frac{1}{2\pi\sigma_i\sigma_r}
$$
$$
\times \exp\left[-\frac{1}{2}\left(\frac{\Delta u_s^{(r)2}}{\sigma_r^2} + \frac{\Delta u_s^{(i)2}}{\sigma_i^2}\right)\right],
$$
(36)

where σ_r^2 and σ_i^2 are the variances of $\Delta\mathbf{u}_s^{(r)}(\xi, \phi)$ and $\Delta\mathbf{u}_s^{(i)}(\xi, \phi)$, respectively.

To study the noise properties of the reconstructed images quantitatively, we generated $N = 250$ noisy complete and minimal-complete data sets by using the noise model in Eq. (36) with $\sigma_r = \sigma_i = 0.05$. We used the fan-beam full-scan and minimal-scan E-C and FBPP algorithms to reconstruct sets of 250 noisy images from these noisy data sets. The matrix size of the reconstructed images was 128×128 pixels, and the wavelength of the incident radiation was equal to 2 pixels. The local image variance was calculated empirically from the N sets of reconstructed images as

$$
\text{var}[\mathbf{a}(\mathbf{r})] = \frac{1}{N-1}\left\{\sum_{i=1}^{N}\mathbf{a}_i(\mathbf{r})^2 - \frac{1}{N}\left[\sum_{i=1}^{N}\mathbf{a}_i(\mathbf{r})\right]^2\right\},
$$
(37)

where $\mathbf{a}_i(\mathbf{r})$ is the ith image obtained by use of the reconstruction algorithm under investigation.

B. Implementation Details

1. E-C Algorithms

From the uniformly sampled values of the scattered field $u_s(\xi, \phi)$, $M_k(\nu_m)$ can be determined at uniformly spaced values of ν_m. However, because of the nonlinear relationship [Eq. (14)] between ν_a and ν_m, the uniformly spaced values of ν_m at which $M_k(\nu_m)$ is sampled do not generally correspond to the uniformly spaced values of ν_a at which one needs to evaluate $P_k(\nu_a)$ (to utilize the fast Fourier transform in the FBPJ algorithm). For each of 65 evenly spaced values of ν_a spanning the range $0 \le \nu_a \le \nu_0\sqrt{1 + 1/\chi^2}$, we used linear interpolation to determine the values

of $M_k(\nu_m = \sqrt{\nu_a^2 + \nu_\mu^2})$ and $M_k(\nu_m = -\sqrt{\nu_a^2 + \nu_\mu^2})$ from the sampled values of $M_k(\nu_m)$ and $M_k(-\nu_m)$, which we subsequently used in Eq. (18) to evaluate $P_k(\nu_a)$. For each value of k, zero-padding interpolation was employed to increase the sampling density along the ν_m axis of $M_k(\nu_m)$ by a factor of 3 to increase the accuracy of the interpolation operation. We employed the consistency condition $P_k(\nu_a) = (-1)^k P_k(-\nu_a)$ to obtain the 64 samples of $P_k(\nu_a)$ for ν_a spanning the range $-\nu_0\sqrt{1 + 1/\chi^2} \le \nu_a < 0$. In our implementation of the FBPJ algorithm, an unapodized ramp filter was used. The interpolation necessary for aligning the backprojected data onto a 128×128 pixel discrete image matrix was performed by bilinear interpolation. When $M_k(\nu_m)$ is replaced by $M_k'(\nu_m)$, and Eq. (34) is employed in place of Eq. (18), the above paragraph also describes our implementation of the fan-beam minimal-scan E-C algorithm.

2. FBPP Algorithms

In the full-scan and minimal-scan FBPP algorithms, at each measurement angle ϕ, $M(\nu_m, \phi)$ or $M'(\nu_m, \phi)$, respectively, was multiplied by the depth-dependent filter $(|\nu_m|/\chi^4\nu')[(1 - \chi^2)\nu' + \chi^2\nu_0]\exp[2\pi\nu_\mu\eta]$ for each of 128 discrete values of η. For each value of η, the filtered data were zero padded to ensure that the pixel size of the reconstructed image matched the pixel size of the images reconstructed by use of the full- and minimal-scan E-C algorithms. The interpolation necessary for aligning the backpropagated data onto a 128×128 pixel discrete image matrix was performed by bilinear interpolation.

The fan-beam minimal-scan E-C and minimal-scan FBPP algorithms utilized the weight function $w(\nu_m, \phi)$ [see Eq. (29)] given by

$$
w(\nu_m, \phi)
$$
$$
= \begin{cases}
\sin^2\left[\dfrac{\pi}{4}\dfrac{\phi}{(\pi/4) - \alpha}\right] & 0 \le \phi \le 2\delta + 2\alpha \\
1 & 2\delta + 2\alpha \le \phi \le \pi + 2\alpha \\
\sin^2\left[\dfrac{\pi}{4}\dfrac{(3\pi/2) - \phi}{(\pi/4) + \alpha}\right] & \pi + 2\alpha \le \phi \le \phi_{\min} \\
0 & \phi_{\min} \le \phi \le 2\pi
\end{cases}
$$
(38)

C. Results

From the simulated noiseless complete and minimal-complete data sets we reconstructed the phantom, using the full- and minimal-scan fan-beam reconstruction algorithms. Figures 7(a) and 7(b) show the images obtained from the full-scan and the minimal-scan E-C reconstruction algorithms, respectively. The full-scan E-C algorithm was specified by $\omega_k(\nu_m) = 1/2$ in Eq. (18). The images appear identical, as is consistent with our assertion that the full- and minimal-scan E-C algorithms are mathematically equivalent in the absence of noise or other errors. Figures 7(c) and 7(d) show the images obtained by use of the full-scan and the minimal-scan
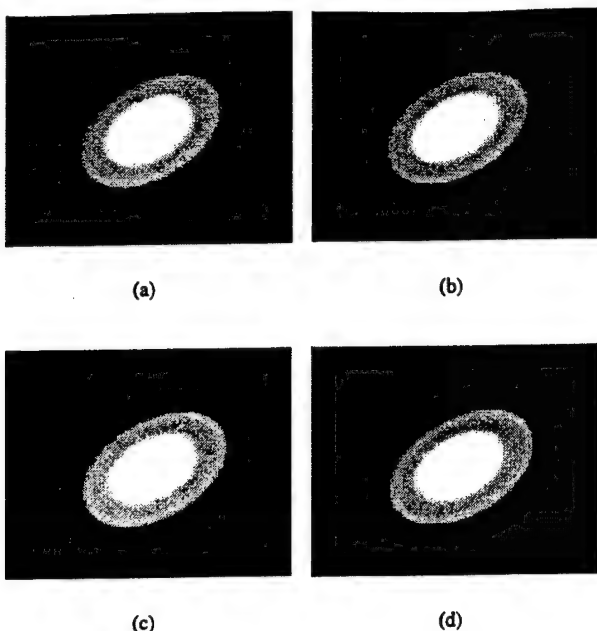
Fig. 7. Images reconstructed from noiseless data by use of (a) full-scan E-C, (b) minimal-scan E-C, (c) full-scan FBPP, and (d) minimal-scan FBPP reconstruction algorithms.
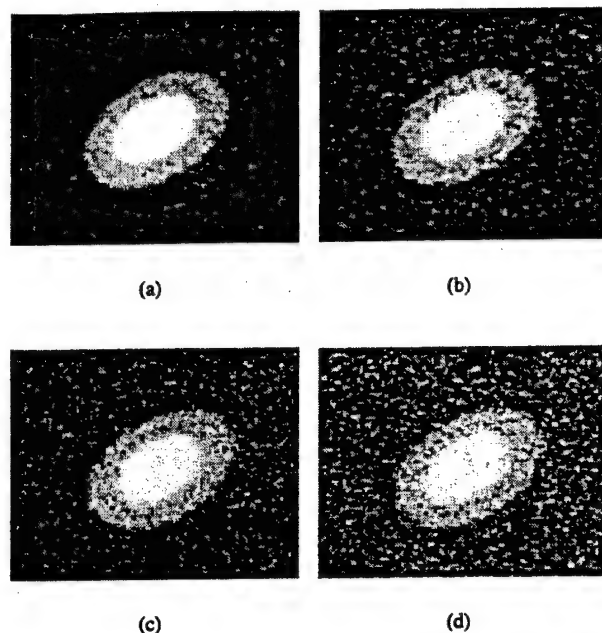

Fig. 8. Images reconstructed from noisy data by use of (a) full-scan E-C, (b) minimal-scan E-C, (c) full-scan FBPP, and (d) minimal-scan FBPP reconstruction algorithms. The noisy data were generated with $\sigma_r = \sigma_i = 0.05$ in Eq. (36).

FBPP reconstruction algorithms, respectively. Again, the images appear identical, consistent with our assertion that the full- and minimal-scan FBPP algorithms are mathematically equivalent in the absence of noise or other errors. As expected, it is also observed that the images reconstructed with the full- and minimal-scan E-C algorithms [Figs. 7(a) and 7(b)] are identical to the images reconstructed with the full- and minimal-scan FBPP algorithms [Figs. 7(c) and 7(d)].

Using one of the simulated noisy complete and minimal-complete data sets, we again reconstructed the phantom, using the full- and minimal-scan E-C and FBPP reconstruction algorithms. Figures 8(a) and 8(b) show the images obtained by use of the full-scan and the minimal-scan E-C reconstruction algorithms, respectively. The images no longer appear identical, and the image reconstructed with the full-scan E-C algorithm appears less noisy than the image reconstructed with the minimal-scan E-C algorithm. Figures 8(c) and 8(d) show the images obtained by use of the full-scan and the minimal-scan FBPP reconstruction algorithms, respectively. Similarly, the image reconstructed with the full-scan FBPP algorithm appears less noisy than the image reconstructed with the minimal-scan FBPP algorithm.

The observation that the full-scan algorithms generate cleaner-looking images than do the minimal-scan algorithms is not surprising and can be qualitatively understood by examination of ways in which the redundant information inherent in the DT data function is utilized. The full-scan FBPP and E-C algorithms [with $\omega_k(\nu_m) \neq 0, 1$] effectively use the redundant information to reconstruct two sepa-

rate images that are averaged to form the final image. It has been quantitatively demonstrated that this effective averaging operation can result in an unbiased reduction of the reconstructed image variance.[12,14] The minimal-scan algorithms, however, utilize part of the redundant information that is inherent in the data function to reduce the angular range over which measurements are required for the reconstruction. The redundant information not used for this purpose can be used to reduce the image variance of the reconstructed image. Specifically, the complementary information contained in subspaces $\mathcal{A}$ and $\mathcal{C}$ of Fig. 3 is weighted, as described by Eq. (29), and is subsequently combined during the reconstruction procedure. However, unlike the full-scan algorithms, the minimal-scan algorithms cannot further reduce the reconstructed image variance by exploiting the fact that subspaces $\mathcal{B}$ and $\mathcal{D}$ contain redundant information.

Although the full- and minimal-scan E-C algorithms are mathematically equivalent to the full- and minimal-scan FBPP algorithms, we observed from Fig. 8 that the E-C and FBPP algorithms respond differently to noise that is present in a discrete data set. To confirm this observation quantitatively, we calculated the local image variances of images reconstructed, using the different methods. Figure 9(a) is a plot of the local variance obtained from the minimal-scan FBPP reconstructed images divided by the local variance obtained from the minimal-scan E-C reconstructed images. Clearly, the ratio of the variances is everywhere greater than 1, quantitatively demonstrating that the minimal-scan E-C reconstruction algorithms are less susceptible to the
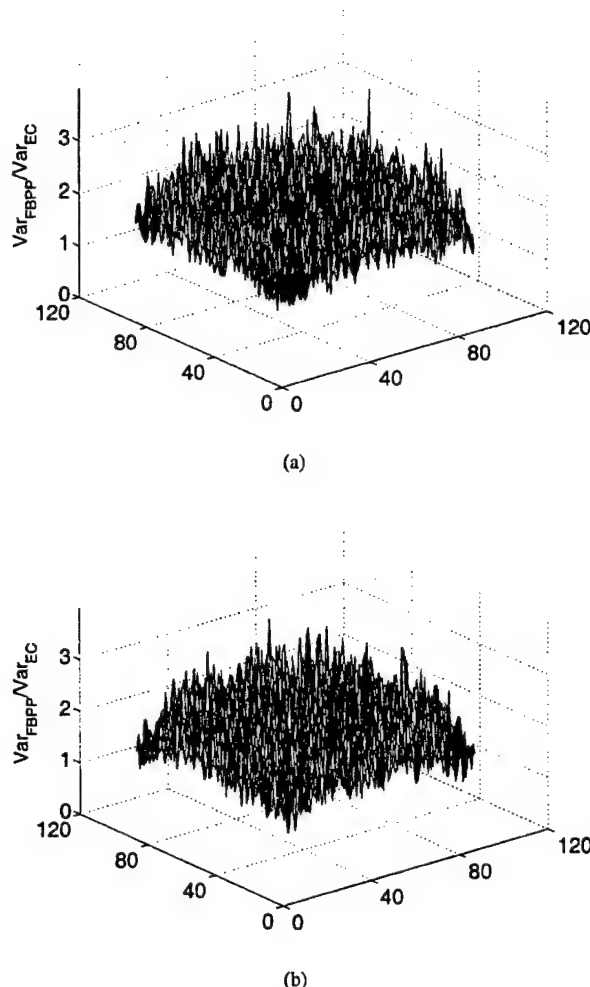
(a)

(b)

Fig. 9. (a) Plot of the local variance obtained from the full-scan FBPP reconstructed images divided by the local variance obtained from full-scan E-C reconstructed images. (b) Plot of the local variance obtained from the minimal-scan FBPP reconstructed images divided by the local variance obtained from minimal-scan E-C reconstructed images. In both the full- and the minimal-scan cases, the E-C algorithms did a better job of suppressing data noise than did the FBPP algorithms.

effects of data noise than are the minimal-scan FBPP reconstruction algorithms. Figure 9(b) is a plot of the local variance obtained from the full-scan FBPP reconstructed images divided by the local variance obtained from the full-scan E-C reconstructed images. The ratio of the variances is everywhere greater than 1, quantitatively demonstrating that the full-scan E-C reconstruction algorithms are less susceptible to the effects of data noise than are the full-scan FBPP reconstruction algorithms. These results are consistent with those obtained previously for full- and minimal-scan DT utilizing plane-wave illumination.[16,21]

6. Summary

In this study, we revealed and examined the redundant information that is inherent in the fan-beam DT data function. Such information can be exploited to reduce the reconstructed image variance or alternatively to reduce the angular scanning requirements of the fan-beam DT experiment. We developed novel full-scan and minimal-scan E-C and FBPP reconstruction algorithms for fan-beam DT. The family of fan-beam full-scan E-C algorithms operates by transforming (in 2D Fourier space) the fan-beam DT problem into a 2D parallel-beam x-ray CT problem, which can be efficiently and stably inverted by use of the FBPJ algorithm. The family of fan-beam full-scan FBPP algorithms operates directly on the modified data function to reconstruct the image and contains the fan-beam FBPP algorithm suggested by Devaney[8] as a special member. Different members of the families of full-scan E-C and FBPP algorithms are specified by different choices of the combination coefficient $\omega_k(\nu_m)$, which controls ways in which the redundant information in the data function is combined. Reconstruction algorithms that correspond to different choices of $\omega_k(\nu_m)$ will in general respond differently to the effect of noise and discrete sampling.[12]

The fan-beam minimal-scan E-C and FBPP algorithms were developed from the concept of the minimal-complete data set. The minimal-complete data set, which is acquired by use of view angles only in $[0, \phi_{min}]$ where $\pi \le \phi_{min} \le 3\pi/2$, contains all the information necessary for exactly reconstructing the scattering object function. The fan-beam minimal-scan E-C and FBPP algorithms utilize a weighting function $w(\nu_m, \phi)$ to normalize appropriately the partially redundant information inherent in the minimal-complete data set. Accordingly, one can form different fan-beam minimal-scan E-C and FBPP algorithms by specifying different choices for this weighting function. Reconstruction algorithms that correspond to different choices of $w(\nu_m, \phi)$ will in general respond differently to the effect of noise and discrete sampling.[15] It can be readily verified that, under the conditions of continuous sampling and in the absence of noise, the minimal-scan E-C and FBPP algorithms are exact and mathematically equivalent to their full-scan counterparts that utilize measurements over the angular range $0 \le \phi \le 2\pi$.

An implementation of the fan-beam full-scan and minimal-scan algorithms has been presented, along with numerical results obtained with noiseless and with noisy simulated data. It was observed that the full-scan algorithms did a better job of suppressing data noise than did their minimal-scan counterparts. We quantitatively demonstrated that the full- and minimal-scan E-C algorithms are less susceptible to data noise and to finite sampling effects than are the full- and minimal-scan FBPP algorithms, respectively. This result is consistent with the observation that the FBPP-based algorithms involve more-complicated numerical operations than do the E-C-based algorithms, which may amplify the propagation of noise and errors into the reconstructed image.

We have assumed a 2D imaging model in this

study. Therefore the developed reconstruction algorithms may be useful for applications in which out-of-plane scattering is not significant. The full-scan E-C and FBPP reconstruction algorithms can be generalized readily to address the three-dimensional DT problem by use of spherical-wave sources and planar measurement surfaces. It remains unclear whether numerically stable versions of the minimal-scan E-C and FBPP reconstruction algorithms can be developed for three-dimensional imaging geometries.

It can readily be verified that the four roots of Eq. (A2) are given by

$$\nu_{m1} = -\nu_{m2} = \nu_a \left(1 - \frac{\nu_a^2}{4\nu_0^2}\right)^{1/2} \left(\frac{\chi^4}{\frac{1}{2}\{1 - (1 - \chi^2)(\nu_a^2/2\nu_0^2) + [1 - \chi^2(1 - \chi^2)(\nu_a^2/\nu_0^2)]^{1/2}\}}\right)^{1/2}, \quad \text{(A3)}$$

$$\nu_{m3} = -\nu_{m4} = \nu_a \left(1 - \frac{\nu_a^2}{4\nu_0^2}\right)^{1/2} \left(\frac{\chi^4}{\frac{1}{2}\{1 - (1 - \chi^2)(\nu_a^2/2\nu_0^2) - [1 - \chi^2(1 - \chi^2)(\nu_a^2/\nu_0^2)]^{1/2}\}}\right)^{1/2}. \quad \text{(A4)}$$

Here we have developed linear reconstruction algorithms for fan-beam DT. It was not our intent to address the limitations of the Born or Rytov[10,11] weak-scattering approximation. The developed full- and minimal-scan algorithms will, however, provide a natural framework for the incorporation of higher-order scattering perturbation approximations[22-24] into the algorithms. It remains to be determined whether minimal-scan reconstruction algorithms can be developed without use of the paraxial approximation.[25] We intend to report on the theoretical development and numerical analysis of these problems in a forthcoming publication.

Because when $0 \leq \nu_a \leq \nu_0\sqrt{1 + 1/\chi^2}$

$$1 - (1 - \chi^2)\frac{\nu_a^2}{2\nu_0^2} < \left[1 - \chi^2(1 - \chi^2)\frac{\nu_a^2}{\nu_0^2}\right]^{1/2}, \quad \text{(A5)}$$

we observe that the roots ν_{m3} and ν_{m4} are complex valued and therefore are not physically meaningful. As expected, when $\chi \to 1$, Eq. (A3) reduces to the known result[12] for plane-wave DT given by

$$\nu_{m1} = -\nu_{m2} = \nu_a \left(1 - \frac{\nu_a^2}{4\nu_0^2}\right)^{1/2}. \quad \text{(A6)}$$

Appendix A: Acronyms Used

CT	Computed tomography
DT	Diffraction tomography
E–C reconstruction algorithm	Estimate-combination reconstruction algorithm
FBPJ reconstruction algorithm	Filtered backprojection reconstruction algorithm
FBPP reconstruction algorithm	Filtered backpropagation reconstruction algorithm
FDP theorem	Fourier diffraction projection theorem

Appendix B: Relationships between ν_m and ν_a

From Eq. (14) we know that

$$\nu_a^2 = \left(\frac{\nu_m}{\chi^2}\right)^2 + \left\{\left[\nu_0^2 - \left(\frac{\nu_m}{\chi}\right)^2\right]^{1/2} - \nu_0\right\}^2. \quad \text{(A1)}$$

For a given ν_a that satisfies $0 \leq \nu_a \leq \nu_0\sqrt{1 + 1/\chi^2}$, we would like to find the values of ν_m that satisfy Eq. (A1). This is equivalent to solving for the roots of the fourth-order equation:

$$(1 - \chi^2)^2\left(\frac{\nu_m}{\chi^2}\right)^4 + [4\nu_0^2 - 2(1 - \chi^2)\nu_a^2]\left(\frac{\nu_m}{\chi^2}\right)^2$$
$$+ \nu_a^2(\nu_a^2 - 4\nu_0^2) = 0. \quad \text{(A2)}$$

References

1. M. P. Andre, P. J. Martin, G. P. Otto, L. K. Olson, T. K. Barrett, B. A. Apivey, and D. A. Palmer, "A new consideration of diffraction computed tomography for breast imaging," Acoust. Imaging **21**, 379–390 (1995).
2. L. Gelius, I. Johansen, N. Sponheim, and J. Stamnes, "Diffraction tomography applications in medicine and seismics," in *NATO Advanced Workshop on Inverse Problems in Scattering and Imaging* (Adam Hilger, New York, 1991), pp. 268–292.
3. R. Mueller, M. Kaveh, and G. Wade, "Reconstructive tomography and applications to ultrasonics," Proc. IEEE **67**, 567–587 (1979).
4. G. Kino, "Acoustic imaging for nondestructive evaluation," Proc. IEEE **67**, 510–525 (1979).
5. A. Devaney, "Geophysical diffraction tomography," IEEE Trans. Geosci. Remote Sens. **22**, 3–13 (1984).
6. E. Robinson, "Image reconstruction in exploration geophysics," IEEE Trans. Sonics Ultrason. **31**, 259–270 (1984).
7. A. Devaney, "A filtered backpropagation algorithm for diffraction tomography," Ultrason. Imaging **4**, 336–350 (1982).
8. A. Devaney, "Generalized projection-slice theorem for fan-beam diffraction tomography," Ultrason. Imaging **7**, 264–275 (1985).
9. A. Ishimaru, *Wave Propagation and Scattering in Random Media* (Academic, New York, 1978).
10. B. Chen and J. Stamnes, "Validity of diffraction tomography based on the first-Born and first-Rytov approximations," Appl. Opt. **37**, 2996–3006 (1998).
11. M. Slaney, A. C. Kak, and L. Larsen, "Limitations of imaging with first-order diffraction tomography," IEEE Trans. Microwave Theory Tech. **32**, 860–874 (1984).
12. X. Pan, "Unified reconstruction theory for diffraction tomog-

raphy with considerations of noise control," J. Opt. Soc. Am. A **15,** 2312–2326 (1998).

13. M. Anastasio and X. Pan, "A new reconstruction algorithm for reflection-mode diffraction tomography," IEEE Trans. Image Process. **9,** 1262–1271 (2000).

14. M. Anastasio and X. Pan, "Investigation of the noise properties of a new class of reconstruction methods in diffraction tomography," Int. J. Imaging Syst. Technol. **10,** 437–446 (2000).

15. X. Pan and M. Anastasio, "Minimal-scan filtered backpropagation algorithms for diffraction tomography," J. Opt. Soc. Am. A **16,** 2896–2903 (1999).

16. M. Anastasio and X. Pan, "Efficient and numerically robust minimal-scan reconstruction algorithms for diffraction tomography," submitted to IEEE Trans. Image Process.

17. E. Wolf, "Three-dimensional structure determination of semi-transparent objects from holographic data," Opt. Commun. **1,** 153–156 (1969).

18. H. H. Barrett, "The Radon transform and its applications," in Progress in Optics, E. Wolf, ed. (North-Holland, Amsterdam, 1984), Vol. 21, pp. 219–286.

19. C. E. Metz and X. Pan, "A unified analysis of exact methods of inverting the 2-D exponential Radon transform, with implica-tions for noise control in SPECT," IEEE Trans. Med. Imag. **14,** 643–658 (1995).

20. M. Azimi and A. Kak, "Distortion in diffraction tomography caused by multiple scattering," IEEE Trans. Med. Imag. **2,** 176–195 (1983).

21. M. Anastasio, M. Kupinski, and X. Pan, "Noise properties of reconstructed images in ultrasound diffraction tomography," IEEE Trans. Nucl. Sci. **45,** 2216–2223 (1998).

22. Z.-Q. Lu and Y.-Y. Zhang, "Acoustical tomography based on the second-order Born transform perturbation approxima-tion," IEEE Trans. Ultrason. Ferroelectrics Freq. Control **43,** 296–302 (1996).

23. G. Tsihrintzis and A. Devaney, "Higher-order (nonlinear) diffraction tomography: reconstruction algorithms and computer simulation," IEEE Trans. Image Process. **9,** 1560–1572 (2000).

24. G. Tsihrintzis and A. Devaney, "Higher order (nonlinear) diffraction tomography: inversion of the Rytov series," IEEE Trans. Inf. Theory **46,** 1748–1761 (2000).

25. A. Devaney and G. Beylkin, "Diffraction tomography using arbitrary transmitter and receiver surfaces," Ultrason. Imaging **6,** 181–193 (1984).

Communications

An Improved Reconstruction Algorithm for 3-D Diffraction Tomography Using Spherical-Wave Sources

Mark A. Anastasio* and Xiaochuan Pan

Abstract—Diffraction tomography (DT) is an inversion technique that reconstructs the refractive index distribution of a weakly scattering object. In this paper, a novel reconstruction algorithm for three-dimensional diffraction tomography employing spherical-wave sources is mathematically developed and numerically implemented. Our algorithm is numerically robust and is much more computationally efficient than the conventional filtered backpropagation algorithm. Our previously developed algorithm for DT using plane-wave sources is contained as a special case.

Index Terms—Diffraction tomography, wavefield inversion, 3-D imaging.

I. INTRODUCTION

In diffraction tomography (DT), a weakly scattering object is interrogated using a diffracting wavefield, and the scattered wavefield around the object is measured and used to reconstruct the (low-pass filtered) refractive index distribution of the scattering object. The principles of DT have been extensively utilized for developing optical [1], [2] and acoustic [3] tomographic imaging systems for biomedical applications.

It is known that the filtered backpropagation (FBPP) and direct Fourier (DF) reconstruction algorithms for three-dimensional (3-D) DT possess certain limitations [4]. The depth-dependent filtering (backpropagation) in the 3-D FBPP algorithm requires a large number of two-dimensional (2-D) fast Fourier transforms (FFTs) to be performed for processing the measured data at each measurement view, which renders the 3-D FBPP algorithm computationally demanding. Furthermore, we have shown that [in two-dimensional (2-D) DT] the FBPP algorithm may amplify data noise more than alternative algorithms do [5]. The 3-D DF algorithms require the use of a 3-D interpolation method to obtain samples on a 3-D Cartesian grid in the Fourier space of the scattering object, upon which a 3-D inverse FFT can be employed to reconstruct the scattering object function. Because the sample density in the 3-D Fourier space obtained from the measured data is nonuniform, sophisticated and computationally demanding interpolation strategies are generally required to avoid producing significant interpolation errors that would degrade the accuracy of the reconstructed image.

For 3-D DT employing plane-wave sources, we have recently developed a new class of reconstruction algorithms that circumvent the shortcomings of the 3-D FBPP and DF algorithms [4]. These algorithms, referred to as plane-wave estimate-combination (E-C) reconstruction algorithms, effectively reduce the 3-D DT reconstruction problem to a series of 2-D X-ray reconstruction problems and, thus, greatly reduce the large computational load required by conventional 3-D DT reconstruction algorithms. Additionally, these algorithms do not require an explicit 3-D interpolation in the Fourier space of the scattering object.

In many imaging applications [1], [6], it may be useful to utilize a diverging spherical-wave rather than a plane-wave to interrogate the scattering object. Because of the distinct advantages of the E-C reconstruction algorithms for plane-wave DT [4], it is important to generalize them to DT employing spherical-wave sources. In this paper, we generalize our previously developed (plane-wave) E-C reconstruction algorithms to DT employing spherical-wave sources and numerically demonstrate the developed algorithm using simulated data.

II. BACKGROUND

We will utilize the model of spherical-wave DT described by Devaney in [7], the scanning geometry of which is shown in Fig. 1. The case of 3-D DT utilizing a plane-wave source can be viewed as a special case of spherical-wave DT and will be discussed below. The scattering object is illuminated by monochromatic spherical-wave source located at the position $\eta = -S$ on the η axis, emitting a wavefield of the form

$$
\begin{aligned}
u_0(\xi, z, \phi) &= A_0 \frac{e^{j2\pi\nu_0|\vec{r}-S\hat{\beta}|}}{|\vec{r}-S\hat{\beta}|} \\
&= A_0 \frac{e^{j2\pi\nu_0\sqrt{\xi^2+z^2+(S+D)^2}}}{\sqrt{\xi^2+z^2+(S+D)^2}}
\end{aligned}
\tag{1}
$$

where A_0 is the complex amplitude, $k = 2\pi\nu_0$ is the wavenumber, $\hat{\beta}$ is a unit vector pointing along the positive η axis, and D is the distance of the detector surface (i.e., $\xi{-}z$ plane) to the axis of rotation (i.e., z axis). A complete data set is acquired by varying the view angle ϕ between 0 and 2π, where ϕ denotes the angle measured from the positive x axis. (The rotated coordinates (ξ, η) are related to the unrotated coordinates (x, y) by $\xi = x\cos\phi + y\sin\phi$ and $\eta = y\cos\phi - x\sin\phi$.) From the measured scattered wavefield data, one seeks to reconstruct the scattering object function $a(\vec{r})$. The underlying physical property of the scattering object that is mapped in DT is the refractive index distribution $n(\vec{r})$, which is related to the scattering object function by the equation $a(\vec{r}) = n^2(\vec{r}) - 1$.

Let $u(\xi, z, \phi)$ denote the measured total wavefield in the $\xi{-}z$ plane positioned at $\eta = D$, as shown in Fig. 1. The scattered data is given by

$$
u_s(\xi, z, \phi) = u(\xi, z, \phi) - u_0(\xi, z, \phi)
\tag{2}
$$

which can be treated as a measurable data function because $u(\xi, z, \phi)$ can be measured and because $u_0(\xi, z, \phi)$ is assumed known. We can introduce a modified data function

$$
M(\nu_m, \nu_z, \phi) = \frac{\chi}{\pi\nu_0^2}\nu' e^{-j2\pi(\nu'-\nu_0)D}\mathcal{F}_{\nu_m}\left\{\frac{u_s(\xi, z, \phi)}{u_0(\xi, z, \phi)}\right\}
\tag{3}
$$

where $\mathcal{F}_{\nu_m, \nu_z}\{h(\xi, z)\} = (1/2\pi)\iint_{-\infty}^{\infty} h(\xi)e^{-j2\pi(\nu_m\xi+\nu_z z)}\,d\xi\,dz$

$$
\chi = \sqrt{\frac{S}{S+D}}
\tag{4}
$$

and

$$
\nu' = \sqrt{\nu_0^2 - \frac{\nu_m^2}{\chi^2} - \frac{\nu_z^2}{\chi^2}}.
\tag{5}
$$

*M. A. Anastasio is with the Department of Biomedical Engineering, Pritzker Institute of Biomedical Science and Engineering, Illinois Institute of Technology, 10 W. 32nd Street, E1-116, Chicago, IL 60616 USA (e-mail: anastasio@iit.edu).

X. Pan is with the Department of Radiology, The University of Chicago, Chicago, IL 60637 USA.
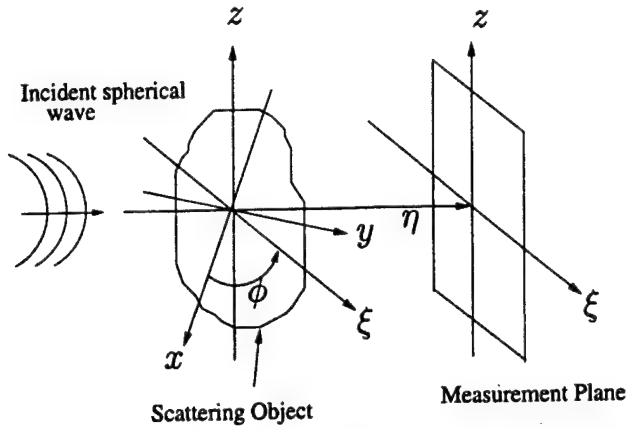
Fig. 1. The classical scanning geometry of spherical-wave 3-D DT. A spherical-wave is incident at angle ϕ, and the scattered field is measured in the ξ–z plane positioned at $\eta = D$. The measurement angle ϕ is varied from 0 to 2π.
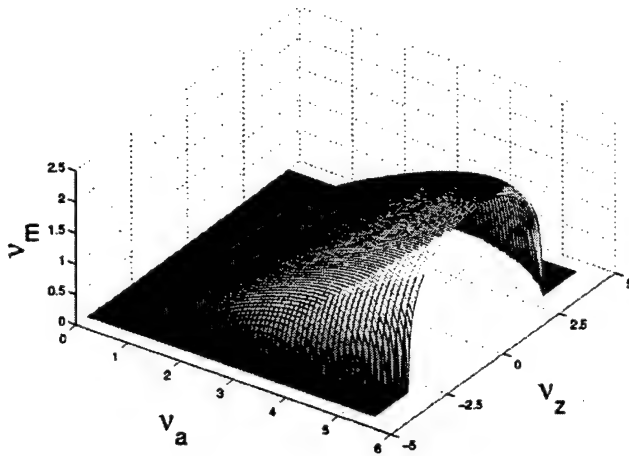

Fig. 2. A plot of ν_m as a function of ν_z and ν_a as described by (17). The plot was generated using $\chi = 0.7$ and $\nu_0 = \pi$.

Using paraxial[1] and weak scattering approximations, Devaney derived [7] the spherical-wave FDP theorem that is given by

$$
\begin{aligned}
&\mathrm{M}(\nu_m,\, \nu_z,\, \phi) \\
&= \int_{-\infty}^{\infty}\int_{-\infty}^{\infty} a(\vec{r}) \mathrm{e}^{-j2\pi[(\nu_m/\chi^2)\xi + (\nu_z/\chi^2)z + (\nu'-\nu_0)\eta]}\, d\vec{r} \\
&\qquad \text{if } \nu_m^2 + \nu_z^2 \le \chi^2 \nu_0^2 \\
&= 0 \qquad \text{if } \nu_m^2 + \nu_z^2 > \chi^2 \nu_0^2.
\end{aligned} \tag{6}
$$

Equation (6) states that the modified data function, $\mathrm{M}(\nu_m,\, \nu_z,\, \phi)$, is equal to a semi-ellipsoidal slice, oriented at angle ϕ, through the 3-D Fourier transform of the object function $a(\vec{r})$. As the measurement angle ϕ is varied between 0 and 2π, a certain low-pass coverage of the 3-D Fourier space is specified (for details, please refer to reference [7]). In this paper, we assume the validity of the first-order Born approximation; the spherical-wave FDP theorem can also be derived based upon the Rytov approximation by appropriately redefining (3) [7].

---

[1]The paraxial approximation requires that both S and D are much larger than the size of the scattering object.

Equation (6), coupled with a 3-D interpolation method, can be used to implement a DF reconstruction algorithm. The 3-D FBPP algorithm for plane-wave DT [8] can readily be extended to 3-D spherical-wave DT [6] and is given by [9], [6]

$$
\begin{aligned}
a(\vec{r}) = \frac{1}{2}\int_{\phi=0}^{2\pi} d\phi \iint_{\nu_m^2 + \nu_z^2 \le \chi^2\nu_0^2} &\frac{|\nu_m|}{\chi^6\nu'}\left[(1-\chi^2)\nu' + \chi^2\nu_0\right] \\
&\times \mathrm{M}(\nu_m,\, \nu_z,\, \phi)\mathrm{e}^{j2\pi(\nu_m'\xi - j2\pi\nu_\mu\eta + \nu_z'z)}\, d\nu_m\, d\nu_z
\end{aligned} \tag{7}
$$

where

$$
\nu_m' = \frac{\nu_m}{\chi^2} \qquad \nu_z' = \frac{\nu_z}{\chi^2}
$$

and

$$
\nu_\mu = -j\left(\sqrt{\nu_0^2 - \chi^2(\nu_m'^2 + \nu_z'^2)} - \nu_0\right).
$$

III. E-C Reconstruction Algorithm

In deriving the E-C reconstructions algorithms for spherical-wave DT, we will modify the procedure employed for the derivation of the plane-wave DT algorithms described in [4]. Let $a(r,\, \theta,\, z)$ denote a 3-D scattering object function where $r = \sqrt{x^2 + y^2}$, $\theta = \tan^{-1}(y/x)$, and z denote cylindrical coordinates. The X-ray transform, $\mathrm{p}(\xi,\, z,\, \phi_0)$, of $a(r,\, \theta,\, z)$ is defined as

$$
\mathrm{p}(\xi,\, z,\, \phi_0) = \int_{\eta=-\infty}^{\infty} a(r,\, \theta,\, z)\, d\eta \tag{8}
$$

where ϕ_0 is the projection angle, $\xi = r\cos(\phi_0 - \theta)$ and $\eta = -r\sin(\phi_0 - \theta)$. Equation (8) states that $\mathrm{p}(\xi,\, z,\, \phi_0)$ is the geometrical projection of $a(r,\, \theta,\, z)$ onto the ξ–z plane oriented at angle ϕ_0 about the z axis. Consequently, $\mathrm{p}(\xi,\, z,\, \phi_0)$ can be interpreted as a stack of 2-D Radon transforms of $a(r,\, \theta,\, z)$ along the z axis. The combination of a 2-D Fourier transform with respect to ξ and z and a one-dimensional Fourier series expansion with respect to ϕ_0 of $\mathrm{p}(\xi,\, z,\, \phi_0)$ is given by

$$
\begin{aligned}
\mathrm{P}_k(\nu_a,\, \nu_z) = \frac{1}{2\pi}\int_{\phi=0}^{2\pi}\iint_{\xi,\, z=-\infty}^{\infty} &\mathrm{p}(\xi,\, z,\, \phi_0) \\
&\times \mathrm{e}^{-j2\pi\nu_a\xi - j2\pi\nu_z z - jk\phi_0}\, d\xi\, dz\, d\phi_0
\end{aligned} \tag{9}
$$

where the integer k is the angular frequency index with respect to ϕ_0, and ν_a and ν_z are the continuous spatial frequencies conjugate to ξ and z, respectively. As a matter of convenience, we refer to $\mathrm{P}_k(\nu_a,\, \nu_z)$ as the "3-D Fourier transform" of $\mathrm{p}(\xi,\, z,\, \phi_0)$. Substituting (8) into (9) and carrying out the integral over ϕ_0 yields

$$
\begin{aligned}
\mathrm{P}_k(\nu_a,\, \nu_z) = (-j)^k \int_{z=-\infty}^{\infty} \mathrm{e}^{-j2\pi\nu_z z}\, dz \int_{\theta=0}^{2\pi}\int_{r=0}^{\infty} &a(r,\, \theta,\, z) \\
&\times \mathrm{e}^{-jk\theta}\mathrm{J}_k(2\pi\nu_a r)r\, dr\, d\theta.
\end{aligned} \tag{10}
$$

Again, for convenience, we refer to $\mathrm{M}_k(\nu_m,\, \nu_z) = (1/2\pi)\int_0^{2\pi}\mathrm{M}(\nu_m,\, \nu_z,\, \phi)\mathrm{e}^{-jk\phi}\, d\phi$ as the "3-D Fourier transform" of the modified data function. Using (6) and noting that $\xi = r\cos(\phi - \theta)$ and $\eta = -r\sin(\phi - \theta)$, one can obtain

$$
\begin{aligned}
&\mathrm{M}_k(\nu_m,\, \nu_z) \\
&= \int_{z=-\infty}^{\infty}\mathrm{e}^{-j2\pi\nu_z'z}\, dz \int_{\theta=0}^{2\pi}\int_{r=0}^{\infty} a(r,\, \theta,\, z) \\
&\quad \times \left\{\frac{1}{2\pi}\int_{\phi=0}^{2\pi}\mathrm{e}^{2\pi\nu_\mu r\sin(\phi-\theta) - j(k\phi + 2\pi\nu_m' r\cos(\phi-\theta))}\, d\phi\right\}r\, dr\, d\theta
\end{aligned} \tag{11}
$$

where $\nu_m^2 + \nu_z^2 \leq \chi^2 \nu_0^2$. Carrying out the integral [10] in the curly brackets in (11), one can re-express $M_k(\nu_m, \nu_z)$ as

$$M_k(\nu_m, \nu_z)$$

$$= (-j)^k \left[\frac{\nu_m' + \nu_\mu}{\sqrt{\nu_m'^2 - \nu_\mu^2}} \right]^k \int_{z=-\infty}^{\infty} e^{-j2\pi\nu_z' z} \, dz$$

$$\times \int_{\theta=0}^{2\pi} \int_{r=0}^{\infty} a(r, \theta, z) e^{-jk\theta} J_k \left(2\pi r \sqrt{\nu_m'^2 - \nu_\mu^2} \right) r \, dr \, d\theta \quad (12)$$

where $\nu_m^2 + \nu_z^2 \leq \chi^2 \nu_0^2$.

Comparison of (10) and (12) yields that for $\nu_m^2 + \nu_z^2 \leq \chi^2 \nu_0^2$

$$P_k(\nu_a, \nu_z') = [\gamma(\nu_m', \nu_z')]^k M_k(\nu_m, \nu_z) \quad (13)$$

where

$$\nu_a^2 = \nu_m'^2 - \nu_\mu^2 \quad (14)$$

and

$$\gamma(\nu_m', \nu_z') = \frac{\sqrt{\nu_m'^2 - \nu_\mu^2}}{\nu_m' + \nu_\mu}. \quad (15)$$

The explicit forms of this general relationship in (13) are determined completely by the forms of the relationship between ν_a and ν_m implied in (14). Equation (14) indicates that the condition $\nu_m^2 + \nu_z^2 \leq \chi^2 \nu_0^2$ is equivalent to the condition $\nu_a^2 + \nu_z'^2 \leq \nu_0^2(1 + 1/\chi^2)$. In order to determine ν_m as a function of ν_z and ν_a, we must solve for the roots of the fourth-order equation

$$C_1 \nu_m'^4 + C_2 \nu_m'^2 + C_3 = 0 \quad (16)$$

where the coefficients C_i are given by

$$C_1 = (1 - \chi^2)^2,$$

$$C_2 = 2(1 - \chi^2) \left(2\nu_0^2 - \nu_a^2 - \frac{\nu_z^2}{\chi^2} \right) + 4\nu_0^2 \chi^2$$

and

$$C_3 = \left(2\nu_0^2 - \nu_a^2 - \frac{\nu_z^2}{\chi^2} \right)^2 - 4\nu_0^2 \left(\nu_0^2 - \frac{\nu_z^2}{\chi^2} \right).$$

The four roots of (16) are given by

$$\nu_{m1}' = -\nu_{m2}' = \left[\frac{-C_2 + \sqrt{C_2^2 - 4C_1 C_3}}{2C_1} \right]^{1/2} \quad (17)$$

and

$$\nu_{m3}' = -\nu_{m4}' = \left[\frac{-C_2 - \sqrt{C_2^2 - 4C_1 C_3}}{2C_1} \right]^{1/2}. \quad (18)$$

Let $\nu_{mi} \equiv \nu_{mi}' \chi^2, i = 1, 2, 3,$ and 4. For $\nu_a^2 + \nu_z'^2 \leq \nu_0^2(1 + 1/\chi^2)$, the two roots ν_{m3}' and ν_{m4}' are complex-valued and, therefore, not physically meaningful. A plot of (17) is shown in Fig. 2. In the plane-wave case ($\chi = 1$), there are only two roots that are given by [4]

$$\nu_{m1} = -\nu_{m2} = \nu_m = \left\{ (\nu_a^2 + \nu_z^2) \left[1 - \frac{\nu_a^2 + \nu_z^2}{4\nu_0^2} \right] - \nu_z^2 \right\}^{1/2} \quad (19)$$

where $\nu_a^2 + \nu_z^2 \leq 2\nu_0^2$.

Therefore, for a given pair of ν_a and ν_z' satisfying $0 \leq \nu_a^2 + \nu_z'^2 \leq \nu_0^2(1 + 1/\chi^2)$, $P_k(\nu_a, \nu_z')$ can be obtained from $M_k(\nu_m, \nu_z)$ at $\nu_{m1} = \nu_m$ and ν_z as

$$P_k(\nu_a, \nu_z') = [\gamma(\nu_{m1}', \nu_z')]^k M_k(\nu_{m1}, \nu_z)$$

$$= [\gamma(\nu_m', \nu_z')]^k M_k(\nu_m, \nu_z) \quad (20)$$

and also from $M_k(\nu_m, \nu_z)$ at $\nu_{m2} = -\nu_m$ and ν_z as

$$P_k(\nu_a, \nu_z') = [\gamma(\nu_{m2}', \nu_z')]^k M_k(\nu_{m2}, \nu_z)$$

$$= (-1)^k [\gamma(\nu_m', \nu_z')]^{-k} M_k(-\nu_m, \nu_z). \quad (21)$$

The fact that there are two distinct ways to obtain $P_k(\nu_a, \nu_z')$ from the measured data can be explained by the existence of a double coverage of the scattering object Fourier space [7]. At a given measurement angle ϕ, the spherical-wave FDP theorem relates the 2-D Fourier transform of the modified measured data to the 3-D Fourier transform of $a(\vec{r})$ evaluated over a semi-ellipsoid oriented at angle ϕ. As the measurement angle ϕ is varied from 0 to 2π, two overlapping coverages of the Fourier space are generated, with each coverage producing one of the relationships described by (20) or (21).

Equations (20) and (21) yield two identical values of $P_k(\nu_a, \nu_z')$ when the measured data are consistent. However, when the measured data contain noise, (20) and (21) will generally produce different values of $P_k(\nu_a, \nu_z')$. These two values can be combined to obtain a final estimate of $P_k(\nu_a, \nu_z')$ that has a reduced noise level as

$$P_k^{(\omega)}(\nu_a, \nu_z') = \omega_k(\nu_m, \nu_z)[\gamma(\nu_m', \nu_z')]^k M_k(\nu_m, \nu_z)$$

$$+ (1 - \omega_k(\nu_m, \nu_z))(-1)^k [\gamma(\nu_m', \nu_z')]^{-k} M_k(-\nu_m, \nu_z) \quad (22)$$

where $\omega_k(\nu_m, \nu_z)$ is a generally complex-valued combination coefficient. The superscript "ω" indicates that $P_k^{(\omega)}(\nu_a, \nu_z')$ is obtained by use of a combination coefficient $\omega_k(\nu_m, \nu_z)$. If $M_k(\nu_m, \nu_z)$ and $M_k(-\nu_m, \nu_z)$ are interpreted as a random variables, then for a given $\omega_k(\nu_m, \nu_z)$, (22) can be interpreted as an *estimation method* for obtaining the ideal sinogram. Because $\omega_k(\nu_m, \nu_z)$ may be any complex-valued function of ν_m, ν_z and k, (22), in effect, represents an infinite class of estimation methods. An estimate of $p(\xi, z, \phi_0)$ can be obtained by taking the 3-D inverse Fourier transform of $P_k^{(\omega)}(\nu_a, \nu_z')$. For a fixed value of z, the filtered backprojection (FBP) algorithm of X-ray CT can be employed to reconstruct the corresponding transverse slice of $a(r, \theta, z)$ from $p(\xi, z, \phi_0)$. We refer to the *combination* of (22) to estimate $P_k^{(\omega)}(\nu_m, \nu_z)$ coupled with the 2-D FBP algorithm to reconstruct transverse slices of $a(r, \theta, z)$ as a *spherical-wave E-C reconstruction algorithm for 3-D DT*.

IV. NUMERICAL RESULTS

We performed numerical simulations to demonstrate the spherical-wave E-C reconstruction algorithm. We considered a mathematical phantom comprised of two different (uniform) spheres whose 3-D Fourier transforms were approximately bandlimited to a sphere of radius $\sqrt{2}\nu_0$. Our intention was not to test the validity of the weak scattering (Born) condition (see the Discussion Section), but rather to demonstrate that the spherical-wave E-C reconstruction algorithm can accurately reconstruct the scattering object function from weakly scattered data. We, therefore, employed (3) and (6), along with the analytic expression for the 3-D Fourier transform of the spheres, to calculate noiseless samples of $u_s(\xi, z, \phi)$ over a 128×128 detector array at 128 view angles that were evenly spaced over $360°$. In generating the simulation data, we assumed a scanning geometry with $S = 100$ (arbitrary units) and $D = 104.0816$ that, according to (4), yields $\chi = 0.7$. In order to simulate the stochastic nature of noisy scattered data, we created a second data set, $\hat{u}_s(\xi, z, \phi)$, where the measured scattered data were treated as samples of an uncorrelated bivariate Gaussian stochastic process. When generating $\hat{u}_s(\xi, z, \phi)$, the mean and variance parameters describing the real (imaginary) component of the stochastic process were set equal to the real (imaginary) values of the noiseless data $u_s(\xi, z, \phi)$. Therefore, at a given position (ξ, z, ϕ) in the data space, the magnitude of noise contained in the real and imaginary components of $\hat{u}_s(\xi, z, \phi)$ was
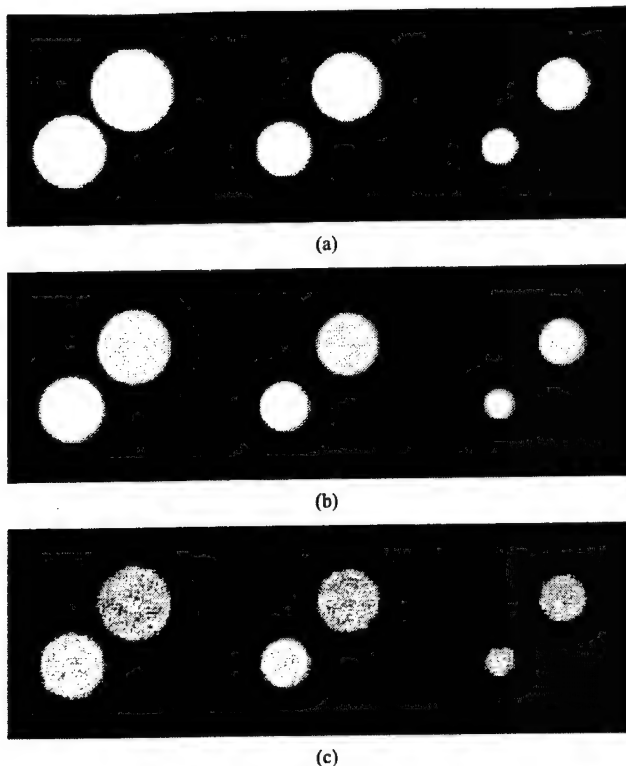
(a)

(b)

(c)

Fig. 3. (a) True slices through the numerical phantom. Transverse slices reconstructed from (b) noiseless and (c) noisy data using a spherical-wave E-C reconstruction algorithm.

proportional to the magnitude of the real and imaginary components of $u_s(\xi, z, \acute{o})$, respectively.

We reconstructed three transverse slices of the scattering object by use of the spherical-wave E-C algorithm specified by $\omega_k(\nu_m, \nu_z) = 1/2$ in (22). It can readily be shown that when the data noise is uncorrelated, $\omega = 1/2$ is a statistically optimal choice in the sense that it minimizes the variance of the estimate $P_k^{(\omega)}(\nu_a)$, which in turn, results in a minimization of the global image variance[2] [4]. For more general noise models, it is, in principle, possible to derive other optimal forms for $\omega_k(\nu_m, \nu_z)$. The true images of the chosen transverse slices are shown in Fig. 3(a). The images reconstructed from the noiseless data, shown in Fig. 3(b), do not contain any artifacts and accurately represent the corresponding true slices shown in Fig. 3(a). The same images reconstructed from the noisy data set are shown in Fig. 3(c). Out of curiosity, we also reconstructed the same transverse slices by use of our previously developed plane-wave E-C reconstruction algorithm (that assumes the measurement geometry corresponds to $\chi = 1$) and the noiseless data set. The reconstructed images, shown in Fig. 4, clearly contain artifacts and distortions. This numerically demonstrates the importance of properly accounting for the wavefield curvature in 3-D DT.

V. DISCUSSION

Previously, we developed a novel class of reconstruction algorithms for 3-D DT using plane-wave sources. These algorithms, referred to as plane-wave E-C reconstruction algorithms, had a significant computational advantage over the conventional 3-D FBPP algorithm, and unlike the 3-D DF method, did not require an explicit 3-D interpolation in the Fourier space of the scattering object.

---

[2] The global image variance is equal to the local variance of an image at a point summed over all points in image space.

Fig. 4. Transverse slices reconstructed from the spherical-wave data function ($\chi = 0.7$) using a plane-wave DT reconstruction algorithm. As expected, the images contain distortions.

The use of a plane-wave source may not be feasible in many experimental situations, and it may be more convenient to interrogate the scattering object using a diverging spherical wave that is produced by a point source. In this paper, we have developed a class of spherical-wave E-C reconstruction algorithms for DT using spherical-wave sources and measurement geometries that satisfy the paraxial approximation [7]. The spherical-wave E-C reconstruction algorithms can be viewed as generalizations of the plane-wave E-C reconstruction algorithms, and reduce to the plane-wave E-C algorithms in the special case $\chi = 1$. The spherical-wave E-C reconstruction algorithms possess the same advantages as their plane-wave counterparts. For example, to reconstruct an N^3 image volume the spherical-wave E-C algorithm requires $\sim N^3 \log N$ numerical operations while the spherical-wave FBPP algorithm described by (7) would require $\sim N^4 \log N$ numerical operations. Unlike DF methods, the spherical-wave E-C algorithms do not require an explicit 3-D interpolation in the Fourier space of the scattering object.

The spherical-wave E-C reconstruction algorithms have been developed using the first-order Born (or Rytov) weak scattering approximation. In certain applications, the weak scattering approximation may not be valid and the reconstructed image may contain artifacts. However, the spherical-wave E-C algorithms provide a natural framework for the incorporation of higher-order scattering perturbation approximations [11]–[13] into the algorithms.

REFERENCES

[1] S. Norton and T. Vo-Ding, "Diffraction tomographic imaging with photon density waves: An explicit solution," *J. Opt. Soc. Amer. A*, vol. 15, pp. 2670–2677, 1998.

[2] N. Jayshree, G. K. Datta, and R. M. Vasu, "Optical tomographic microscope for quantitative imaging of phase objects," *Appl. Opt.*, vol. 39, pp. 277–283, 2000.

[3] M. Andre, P. Martin, G. P. Otto, L. K. Olson, T. K. Barrett, and B. A. Spivey, "A new consideration of diffraction computed tomography for breast imaging: Studies in phantoms and patients," *Acoust. Imag.*, vol. 21, pp. 379–390, 1995.

[4] M. Anastasio and X. Pan, "Computationally efficient and statistically robust image reconstruction in 3D diffraction tomography," *J. Opt. Soc. Amer. A*, vol. 17, pp. 391–400, 2000.

[5] ——, "Numerically robust minimal-scan reconstruction algorithms for diffraction tomography via. radon transform inversion," Int. J. Imag. Syst. Technol., 2002, to be published.

[6] Z. Lu, "Multidimensional structure diffraction tomography for varying object orientation through generalized scattered waves," *Inverse Prob.*, vol. 1, pp. 339–356, 1985.

[7] A. J. Devaney, "Generalized projection-slice theorem for fan-beam diffraction tomography," *Ultrason. Imag.*, vol. 7, pp. 264–275, 1985.

[8] A. J. Devaney, "A filtered backpropagation algorithm for diffraction tomography," *Ultrason. Imag.*, vol. 4, pp. 336–350, 1982.

[9] M. Anastasio, "Development and analysis of image reconstruction algorithms in diffraction tomography," Ph.D. dissertation, The University of Chicago, Chicago, IL, 2001.

[10] C. E. Metz and X. Pan, "A unified analysis of exact methods of inverting the 2-d exponential radon transform, with implications for noise control in SPECT," *IEEE Trans. Med. Imag.*, vol. 14, pp. 643–658, Dec. 1995.

[11] Z.-Q. Lu and Y.-Y. Zhang, "Acoustical tomography based on the second-order Born transform perturbation approximation," *IEEE Trans. Ultrason., Ferroelect., Freq. Contr.*, vol. 43, pp. 296–302, Mar. 1996.

[12] G. A. Tsihrintzis and A. J. Devaney, "Higher-order (nonlinear) diffraction tomography: Reconstruction algorithms and computer simulation," *IEEE Trans. Image Processing*, vol. 9, pp. 1560–1572, Sept. 2000.

[13] G. A. Tsihrintzis and A. J. Devaney, "Higher order (nonlinear) diffraction tomography: Inversion of the Rytov series," *IEEE Trans. Inform. Theory*, vol. 46, pp. 1748–1761, Aug. 2000.

A Comparison of Algorithms for Detection of Spikes in the Electroencephalogram

Clement C. C. Pang, Adrian R. M. Upton, Glenn Shine, and Markad V. Kamath*

Abstract—Identification of the short transient waveform, called a spike, in the cortical electroencephalogram (EEG) plays an important role during diagnosis of neurological disorders such as epilepsy. It has been suggested that artificial neural networks (ANN) can be employed for spike detection in the EEG, if suitable features are provided as input to an ANN. In this paper, we explore the performance of neural network-based classifiers using features selected by algorithms suggested by four previous investigators. Of these, three algorithms model the spike by mathematical parameters and use them as features for classification while the fourth algorithm uses raw EEG to train the classifier. The objective of this paper is to examine if there is any inherent advantage to any particular set of features, subject to the condition that the same data are used for all feature selection algorithms. Our results suggest that artificial neural networks trained with features selected using any one of the above three algorithms as well as raw EEG directly fed to the ANN will yield similar results.

Index Terms—Classification, EEG, neural networks, spike detection.

I. INTRODUCTION

Epilepsy is characterized by sudden recurrent and transient disturbances of mental function and/or movements of the body that result from excessive discharging of groups of brain cells [10], [13]. Patients who are suspected of having epileptogenic foci in their brain are subjected to an electroencephalography (EEG) recording in the neurophysiology laboratory. In clinical neurological practice, detection of abnormal EEG activity plays an important role in the diagnosis of epilepsy [10]. It is generally accepted that spikes (often called "spike discharges"), a kind of transient waveform(s) present in human EEG, have a high correlation with seizure occurrence. Therefore, detection of spikes in the EEG plays a key role in the diagnosis of the disease.

Over the past several decades, physicians have developed empirical techniques which help them identify episodes of abnormal signal components, including the spike discharges. Such expertise has led to

methods that mimic the mental process of the neurologist in identifying spikes [5], [6], [17]. Research involving a variety of signal processing algorithms has led to automated systems for analyzing and locating spikes in EEG recordings lasting several hours [4], [14]. While it is desirable to have detection of spikes and transient waveforms in continuous on-line EEG, efficient algorithms for accurate off-line detection of spikes and transient waveforms have been studied for some time [5], [11], [14], [19], [21].

Previous implementations have approached the problem using back-propagation [3], [11], [21] and Kohonen's self-organizing maps [12]. We examined four methods that use features derived from wavelet transforms (WTs) [9], autoregressive (AR) modeling [18], context parameters [20] and an ANN trained using raw EEG [15]. These algorithms were chosen specifically for this study due to their high spike detection rates and their ability to reject false alarms.

II. METHODS

A. Definition of Spikes

Epileptic EEG contains transient waveforms called spikes (or spike discharge) and includes the following types of waveforms (Fig. 1).

— Spike: lasts 20–70 ms.
— Sharp wave: lasts 70–200 ms although not as sharply contoured as a spike.
— Spike and wave complex : A spike is followed by a slow wave. If they occur at rates below 3 Hz, they are called spike-and-slow wave complexes.
— Polyspikes: Multiple spike complexes; several spikes occur in sequence.
— Polyspike—and—slow wave: polyspikes followed by a slow wave.

Fig. 1 shows examples of a spike, spike and a slow wave, polyspikes in addition to normal EEG, and EEG contaminated by eye blinks and muscle artifacts.

B. Feature Extraction Algorithms

Mathematical modeling of spikes has enabled researchers a wide range of methods to characterize a spike. We present four principal procedures developed by previous researchers to achieve this purpose.

1) Tarassenko's Algorithm: Tarassenko *et al.* [18] considered both time-domain parameters and frequency-domain parameters for the characterization of the EEG signal. The proposed time-domain parameters are as follows (Fig. 2):

Average slope:

$$s_{av} = \frac{|s_1| + |s_o|}{2} \quad [\text{V/s}] \tag{1}$$

$$\text{where } s_o = \frac{x_1 - x_0}{\Delta t}, \ s_1 = \frac{x_2 - x_1}{\Delta t}$$

$$\text{and } \Delta t = \frac{1}{F_s}$$

Sharpness:

$$a = |s_1 - s_0| \quad [\text{V/s}^2] \tag{2}$$

Mobility:

$$(2\pi M)^2 = \frac{1}{(\Delta t)^2} \frac{s_{av}^2}{x_{av}^2} \quad [\text{Hz}] \tag{3}$$

Complexity:

$$(2\pi C)^2 = \left(\frac{1}{(\Delta t)^2} \frac{(s_1 - s_0)^2}{s_{av}^2} \right) - (2\pi M)^2 \quad [\text{Hz}] \tag{4}$$

where, x_{av} is the average amplitude of the signal within an epoch.

The latter two parameters, which were proposed by Hjorth [8] and Walmsley [19], can be used to characterize the slope and slope spread

Numerically Robust Minimal-Scan Reconstruction Algorithms for Diffraction Tomography via Radon Transform Inversion

Mark A. Anastasio,[1] Xiaochuan Pan[2]

[1] Pritzker Institute of Medical Engineering, Illinois Institute of Technology, 10 West 32nd Street, Chicago, Illinois 60616-3793

[2] Department of Radiology, The University of Chicago, Chicago, Illinois 60637

ABSTRACT: It is widely believed that measurements from a full angular range of 2π are generally required to exactly reconstruct a complex-valued refractive index distribution in diffraction tomography (DT). In this work, we developed a new class of minimal-scan reconstruction algorithms for DT that utilizes measurements only over the angular range $0 \leq \phi \leq 3\pi/2$ to perform an exact reconstruction. These algorithms, referred to as minimal-scan estimate-combination (MS-E-C) reconstruction algorithms, effectively operate by transforming the DT reconstruction problem into a conventional x-ray CT reconstruction problem that requires inversion of the Radon transform. We performed computer simulations to compare the noise and numerical properties of the MS-E-C algorithms against existing filtered backpropagation-based algorithms. © 2002 Wiley Periodicals, Inc. Int J Imaging Syst Technol, 12, 84–91, 2002; Published online in Wiley InterScience (www.interscience.wiley.com). DOI 10.1002/ima.10014

Key words: topographic reconstruction; diffraction tomography; wavefield inversion

I. INTRODUCTION

In diffraction tomography (DT), a scattering object is interrogated using a diffracting acoustical or electromagnetic wavefield, and the scattered wavefield around the object is measured and used to reconstruct the refractive index distribution of the scattering object. There are numerous potential applications of DT that can be found in various scientific fields (Andre et al., 1995; Tabbara et al., 1988; Mueller et al., 1979; Kino, 1979; Devaney, 1984; Robinson, 1984). Recently, there has also been considerable interest in using DT to perform coherent x-ray imaging using third-generation synchrotron sources (Cheng and Han, 2001). Unlike the x-rays used in computed tomography (CT) that travel along straight lines, the radiation employed in DT has to be treated in terms of wavefronts and fields scattered by inhomogeneities in the object. In DT, the interaction between the incident wavefield and the object medium is governed by the inhomogeneous Helmholtz equation. Using a weak-scattering approximation, the inhomogeneous equation can be analytically solved (Wolf, 1969; Mueller et al., 1979) to obtain a linear relationship between the scattered field and the refractive index distribution.

This relationship has been used to develop DT reconstruction algorithms such as the well-known filtered backpropagation (FBPP) algorithm (Devaney, 1982), which is a generalization of the filtered backprojection (FBPJ) algorithm of x-ray CT.

It is widely believed that measurements from a full-angular range of 2π around the scattering object are generally required to exactly reconstruct a complex-valued refractive index distribution (Devaney, 1982). However, we have recently revealed that one needs measurements only over the angular range $0 \leq \phi \leq 3\pi/2$ to perform an exact reconstruction, and we developed minimal-scan filtered backpropagation (MS-FBPP) algorithms to achieve this (Pan and Anastasio, 1999). A useful characteristic of the MS-FBPP algorithms is their ability to decrease the data acquisition time by at least 25% over conventional (full-scan) algorithms. They can also reduce artifacts due to movement in or temporal fluctuations of the scattering object. Furthermore, in certain practical situations, it may be impossible to acquire measurements over a full 2π angular range.

A new class of reconstruction algorithms has recently been developed for full-scan DT (in other words, DT employing measurements over a full 2π angular range). These algorithms, referred to as estimate-combination (E-C) reconstruction algorithms (Pan, 1998; Anastasio and Pan, 2000b; Anastasio and Pan, 2000a), effectively operate by transforming the DT reconstruction problem into a conventional x-ray CT reconstruction problem that can be efficiently solved using the filtered backprojection (FBPJ) algorithm. The E-C reconstruction algorithms are more computationally efficient than the FBPP algorithm, and also provide a flexible framework for imposing unbiased regularization.

Because the E-C reconstruction algorithms involve a Fourier series expansion of the data function that is acquired over the angular range $0 \leq \phi \leq 2\pi$, they cannot be applied directly to the minimal-scan problem where measurements are only acquired over the angular range $0 \leq \phi \leq 3\pi/2$. Because of the potential advantages of the E-C reconstruction algorithms, it is important to generalize them to the minimal-scan situation. In this work, we developed minimal-scan E-C (MS-E-C) reconstruction algorithms for DT. We performed computer simulations to compare the noise and numerical properties of the MS-E-C and MS-FBPP algorithms. Our results quantitatively demonstrate that the MS-E-C algorithms pos-

Correspondence to: Mark A. Anastasio, Ph.D., Pritzker Institute of Medical Engineering, Illinois Institute of Technology, 10 West 32nd Street, Chicago, IL 60616-3793. (V) 312-567-3926, (F) 312-567-5707, Email: anastasio@iit.edu.
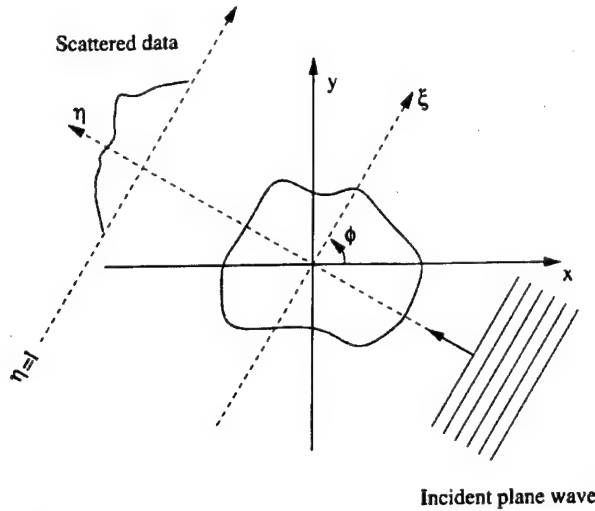
Figure 1. The classical scanning geometry of 2D DT. The insonifying plane wave propagates along the η axis, and the scattered wave field is measured along the line $\eta = 1$. Full-scan and minimal-scan data sets are obtained by varying the measurement angle ϕ between 0 and 2π or between 0 and $3\pi/2$, respectively.

sess statistical and numerical properties superior to those of the MS-FBPP algorithms.

II. BACKGROUND

A. The Fourier Diffraction Projection Theorem. In two-dimensional (2D) DT employing the classical scanning configuration, as shown in Figure 1, the scattering object is illuminated by monochromatic plane-wave radiation of frequency ν_0, and the transmitted wavefield is measured along the ξ axis oriented at a measurement angle ϕ, at a distance $\eta = l$ from the origin. From measurements of the scattered wavefield obtained at various angles ϕ, one seeks to reconstruct the scattering object function $a(\vec{r})$, which is related to the refractive index distribution $n(r, \theta)$ by $a(r, \theta) = n^2(r, \theta) - 1$.

At a measurement angle ϕ, the scattered data are measured along the line $\eta = l$, as shown in figure 1. Let $U_s(\nu_m, \phi)$ to denote the 1D Fourier transform of the measured scattered data with respect to ξ. For convenience, we define a modified 1D Fourier transform of the scattered data as

$$M(\nu_m, \phi) = U_s(\nu_m, \phi)\frac{j\nu'}{2\pi^2\nu_0^2 U_0} e^{-j2\pi\nu' l}, \qquad (1)$$

where $\nu' = \sqrt{\nu_0^2 - \nu_m^2}$ and $|\nu_m| \le \nu_0$. The quantities on the right-hand side of equation 1 are known or can be measured. Therefore, we will treat $M(\nu_m, \phi)$ as a measurable data function. Under the Born approximation (Mueller et al., 1979), the Fourier diffraction projection (FDP) theorem (Mueller et al., 1979) can be derived, which is mathematically stated as

$$
\begin{aligned}
M(\nu_m, \phi) &= \int_{-\infty}^{\infty}\int_{-\infty}^{\infty} a(\vec{r})e^{-j2\pi[\nu_m\xi-(\nu'-\nu_0)\eta]}\, d\vec{r} \quad && \text{if } |\nu_m| \le \nu_0 \\
&= 0 && \text{if } |\nu_m| > \nu_0,
\end{aligned}
$$

$$(2)$$

where the polar coordinates (r, θ) and the rotated coordinates (ξ, η) are related through $\xi = r\cos(\phi - \theta)$ and $\eta = -r\sin(\phi - \theta)$. The FDP theorem indicates that $M(\nu_m, \phi)$ provides the values of the 2D Fourier transform of $a(\vec{r})$ along the semi-circular arc AOB of radius ν_0, as shown in figure 2.

B. Minimal-Scan Filtered Backpropagation Algorithms.
The widely used filtered backpropagation (FBPP) algorithm (Devaney, 1982) is mathematically expressed as

$$a(\vec{r}) = \frac{1}{2}\int_{\phi=0}^{2\pi}\int_{\nu_m=-\nu_0}^{\nu_0} \frac{\nu_0}{\nu'}\,|\nu_m| M(\nu_m, \phi)e^{j2\pi\nu_m\xi+2\pi\nu_\mu\eta}\, d\nu_m\, d\phi.$$

$$(3)$$

where $\nu_\mu = j(\sqrt{\nu_0^2 - \nu_m^2} - \nu_0)$. When $\nu_0 \to \infty$, the FBPP algorithm reduces to the filtered backprojection (FBPJ) algorithm of x-ray CT. The FBPP algorithm generally requires full knowledge of $M(\nu_m, \phi)$ in the data space $\mathcal{W} = [|\nu_m| \le \nu_0, 0 \le \phi \le 2\pi]$, for exact reconstruction of the generally complex-valued object function. We will refer to such full knowledge of $M(\nu_m, \phi)$ as a *full-scan data set*. The full-scan data space $\mathcal{W}$ can be decomposed into four subspaces, $\mathcal{A}$, $\mathcal{B}$, $\mathcal{C}$, and $\mathcal{D}$, where $\mathcal{A} = [|\nu_m| \le \nu_0, 0 \le \phi \le 2\alpha + \pi/2]$, $\mathcal{B} = [|\nu_m| \le \nu_0, \pi/2 + 2\alpha \le \phi \le \pi + 2\alpha]$, $\mathcal{C} = [|\nu_m| \le \nu_0, \pi + 2\alpha \le \phi \le 3\pi/2]$ and $\mathcal{D} = [|\nu_m| \le \nu_0, 3\pi/2 \le \phi \le 2\pi]$, where $\alpha = \text{sgn}(\nu_m)\arcsin\sqrt{\nu_m^2 - \nu_\mu^2}/(2\nu_o)$. A schematic of this partitioning of the data space is given in figure 3. Using the FDP theorem, it can be shown (Pan and Kak, 1983) that $M(\nu_m, \phi) = M(-\nu_m, \phi + \pi - 2\alpha)$. Therefore, the information contained in subspace $\mathcal{A}$ is redundant to that contained in subspace $\mathcal{C}$, and the information contained in subspace $\mathcal{B}$ is redundant to that contained in subspace $\mathcal{D}$. We have demonstrated (Pan and Anastasio, 1999) that it is possible to exactly reconstruct the object function using only knowledge of $M(\nu_m, \phi)$ in the subspace $\mathcal{M} = \mathcal{A} \cup \mathcal{B}$
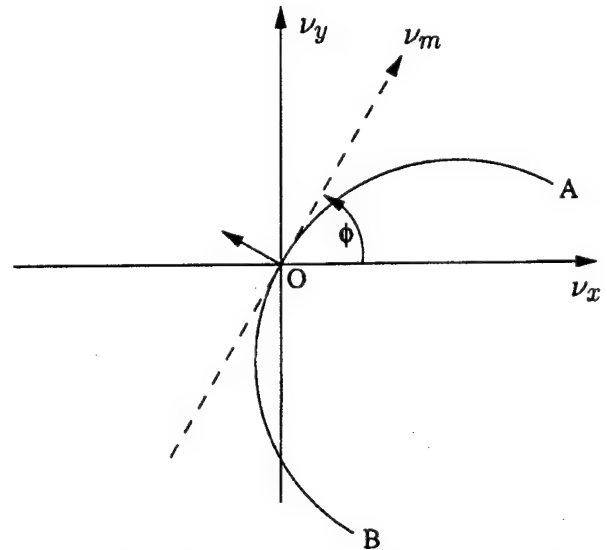

Figure 2. The FDP theorem states that $M(\nu_m, \phi)$ is equal to the 2D Fourier transform of $a(\vec{r})$ along a semi-circle AOB that has a radius of ν_0 and is centered at $\nu_\eta = \nu_0$.
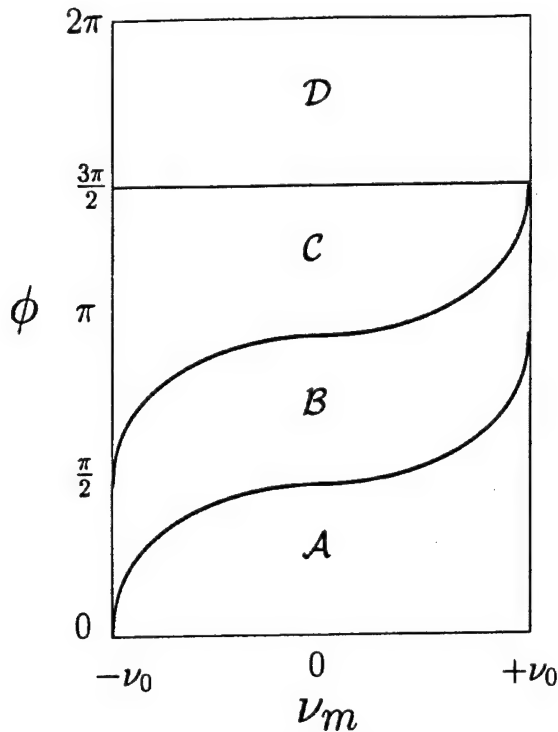
Figure 3. The subspaces $\mathcal{A}$, $\mathcal{B}$, $\mathcal{C}$ and $\mathcal{D}$ in the complete DT data space.

$\cup \, \mathcal{C} = [|\nu_m| \leq \nu_0, 0 \leq \phi \leq 3\pi/2]$, which we refer to as a *a minimal-scan data set.*

Although the minimal-scan data set $\mathcal{M}$ contains all of the information necessary for exact reconstruction of the scattering object function, the redundant information contained in the subspaces $\mathcal{A}$ and $\mathcal{C}$ needs to be properly normalized in the reconstruction process (Pan and Anastasio, 1999). The MS-FBPP algorithms operate by first normalizing such partially redundant information by generating an appropriately weighted minimal-scan data set $M'(\nu_m, \phi)$ and subsequently using the FBPP algorithm described by equation 3 (scaled by a factor of 2), to exactly reconstruct the image. The weighted minimal-scan data set is given by (Pan and Anastasio, 1999)

$$M'(\nu_m, \phi) = w(\nu_m, \phi)M(\nu_m, \phi), \tag{4}$$

where $w(\nu_m, \phi)$ is a function of ν_m and ϕ, which satisfies

$$w(\nu_m, \phi) + w(-\nu_m, \phi + \pi - 2\alpha) = 1 \tag{5a}$$

in complete data space $\mathcal{W}$,

$$w(\nu_m, \phi) = 1 \tag{5b}$$

in subspace $\mathcal{B}$, and

$$w(\nu_m, \phi) = 0 \tag{5c}$$

in subspace $\mathcal{D}$. Although the forms of $w(\nu_m, \phi)$ in subspaces $\mathcal{B}$ and $\mathcal{D}$ are completely specified by equations 5b and 5c, respectively, the explicit forms of $w(\nu_m, \phi)$ in subspaces $\mathcal{A}$ and $\mathcal{C}$ are unspecified for the moment. In principle, one can choose different $w(\nu_m, \phi)$ in subspaces $\mathcal{A}$ and $\mathcal{C}$ as long as these $w(\nu_m, \phi)$ satisfy equation 5a.

III. MINIMAL-SCAN ESTIMATE-COMBINATION ALGORITHMS

The previously derived (full-scan) E-C reconstruction algorithms are more computationally efficient than the (full-scan) FBPP reconstruction algorithms, which involve a depth-dependent filtering operation (backpropagation). Accordingly, we expect that the MS-FBPP algorithms, which use the FBPP algorithm to reconstruct the final image from the weighted data function $M'(\nu_m, \phi)$, will also be less computationally efficient than the E-C reconstruction algorithms. Because they will involve fewer and less complicated numerical operations, we also expect that the MS-E-C algorithms will be minimize the propagation of data noise and errors as compared to the MS-FBPP algorithms. The full-scan E-C reconstruction algorithms (Pan, 1998; Anastasio and Pan, 2000b) involve a Fourier series expansion of the data function $M(\nu_m, \phi)$, which requires knowledge of $M(\nu_m, \phi)$ over an angular range of 2π, and therefore can not be directly applied to the minimal-scan data set containing only measurements in the range $0 \leq \phi \leq 3\pi/3$. Below, we develop minimal-scan E-C (MS-E-C) reconstruction algorithms that can be directly applied to the minimal-scan data set.

A. The Radon Transform. Let $p(\xi, \phi)$ and $P_k(\nu_a)$ denote the Radon transform of $a(r, \theta)$ and its 2D Fourier transform, respectively. (Here, the 2D Fourier transform is actually a 1D Fourier transform with respect to ξ and a 1D Fourier series with respect to ϕ.) From knowledge of $p(\xi, \phi)$, or equivalently, $P_k(\nu_a)$, one can reconstruct $a(r, \theta)$ by use of the computationally efficient and numerically stable FBPJ algorithm, which is given by

$$a(r, \theta) = \frac{1}{2} \int_0^{2\pi} \int_{-\infty}^{\infty} \sum_{k=-\infty}^{\infty} P_k(\nu_a)e^{jk\phi}|\nu_a|e^{j\nu_a r\cos(\phi-\theta)} \, d\nu_a \, d\phi.$$

$$\tag{6a}$$

For theoretical convenience, the FBPJ algorithm can also be expressed as

$$a(r, \theta) = 2\pi \sum_{k=-\infty}^{\infty} j^k \int_{\nu_a=0}^{\infty} P_k(\nu_a)e^{jk\theta}J_k(2\pi\nu_a r)\nu_a \, d\nu_a, \tag{6b}$$

where $J_k(\,\cdot\,)$ is a Bessel function of the first kind. The MS-E-C algorithms will operate by estimating $P_k(\nu_a)$, or equivalently $p(\xi, \phi)$, from the minimal-scan data set, and using the FBPJ algorithm to reconstruct the final image $a(r, \theta)$.

B. Derivation of the MS-E-C Algorithms. Consider a given weighting function $w(\nu_m, \phi)$ in equation 4. The corresponding MS-FBPP algorithm can be expressed as (Pan and Anastasio, 1999)

$$a(r, \theta) = \frac{1}{2} \int_{\phi=0}^{2\pi} \int_{\nu_m=-\nu_0}^{\nu_0} \frac{\nu_0}{\nu'} |\nu_m|M'(\nu_m, \phi)e^{j2\pi\nu_m\xi+2\pi\nu_a\eta} \, d\nu_m \, d\phi.$$

$$\tag{7}$$

Let $M'_k(\nu_m)$ denote the Fourier series expansion of $M'(\nu_m, \phi)$. One can re-express equation 7 as

$$a(r, \theta)$$

$$= \frac{1}{2} \int_{\phi=0}^{2\pi} \int_{\nu_m=-\nu_0}^{\nu_0} \frac{\nu_0}{\nu'} |\nu_m| e^{j2\pi\nu_m\xi + 2\pi\nu_\mu\eta} \sum_{k=-\infty}^{\infty} M'_k(\nu_m) e^{jk\phi} \, d\nu_m \, d\phi.$$

$$(8)$$

Using the definition $\gamma(\nu_m) = e^{j\alpha}$ and separating the contribution to the integral from positive and negative ν_m, equation 8 can be re-written as

$$a(r, \theta) = \frac{1}{2} \int_{\phi=0}^{2\pi} \int_{\nu_m=0}^{\nu_0} \frac{\nu_0}{\nu'} \nu_m e^{j2\pi\nu_m\xi + 2\pi\nu_\mu\eta + jk\phi} \sum_{k=-\infty}^{\infty} M'_k(\nu_m) \, d\nu_m \, d\phi$$

$$+ \frac{1}{2} \int_{\phi=0}^{2\pi} \int_{\nu_m=-\nu_0}^{0} \frac{\nu_0}{\nu'} (-\nu_m) e^{j2\pi\nu_m\xi + 2\pi\nu_\mu\eta + jk\phi}$$

$$\times \sum_{k=-\infty}^{\infty} M'_k(\nu_m) \, d\nu_m \, d\phi. \quad (9)$$

Changing ν_m to $-\nu_m$ in the second term in equation 9 and grouping ϕ-dependent terms yields

$$a(r, \theta) = \frac{1}{2} \int_{\nu_m=0}^{\nu_0} \frac{\nu_0}{\nu'} \nu_m \left\{ \int_{\phi=0}^{2\pi} e^{j2\pi\nu_m\xi + 2\pi\nu_\mu\eta + jk\phi} \, d\phi \right\}$$

$$\times \sum_{k=-\infty}^{\infty} M'_k(\nu_m) \, d\nu_m + \frac{1}{2} \int_{\phi=0}^{2\pi} \int_{\nu_m=0}^{\nu_0} \frac{\nu_0}{\nu'} \nu_m$$

$$\times \left\{ \int_{\phi=0}^{2\pi} e^{-j2\pi\nu_m\xi + 2\pi\nu_\mu\eta + jk\phi} \, d\phi \right\} \sum_{k=-\infty}^{\infty} M'_k(-\nu_m) \, d\nu_m. \quad (10)$$

The integrals in the curly braces of the first and second terms of equation 10 can be evaluated (Metz and Pan, 1995) yielding the expressions $2\pi j^k \gamma(\nu_m)^k e^{jk\theta} J_k(2\pi r \sqrt{\nu_m^2 - \nu_\mu^2})$ and $2\pi(-1)^k j^k \gamma(\nu_m)^{-k} e^{jk\theta} J_k(2\pi r \sqrt{\nu_m^2 - \nu_\mu^2})$, respectively. Using this result and the change of variables $\nu_a = \sqrt{\nu_m^2 - \nu_\mu^2}$ (which implies $\nu_a d\nu_a = \nu_0/\nu' \, \nu_m d\nu_m$), we arrive at

$$a(r, \theta) = \pi \sum_{k=-\infty}^{\infty} j^k \int_{\nu_a=0}^{\sqrt{2}\nu_0} \left[\gamma^k M'_k(\nu_m) + (-1)^k \gamma^{-k} M'_k(-\nu_m) \right]$$

$$\times e^{jk\theta} J_k(2\pi\nu_a r) \nu_a \, d\nu_a, \quad (11)$$

where $\nu_m = \nu_a \sqrt{1 - \nu_a^2/2\nu_0^2}$. Comparison of Eqns. 11 and 6b indicates that, for $0 \le \nu_a \le \sqrt{2}\nu_0$,

$$P_k(\nu_a) = \frac{1}{2} \left[\gamma^k M'_k(\nu_m) + (-1)^k \gamma^{-k} M'_k(-\nu_m) \right], \quad (12)$$

and therefore the Radon transform of the scattering object function $a(r, \theta)$ can be estimated from the appropriately weighted minimal-scan data set. *The use of equation 12 to estimate $P_k(\nu_a)$ coupled with the 2D FBPJ algorithm to reconstruct $a(r, \theta)$ is referred to as a MS-E-C reconstruction algorithm.* In practice, the FBPJ algorithm described by equation 6a requires knowledge of $P_k(\nu_a)$ for evenly spaced values of ν_a spanning the range $-\sqrt{2}\,\nu_0 \le \nu_a \le \sqrt{2}\,\nu_0$ in order to be efficiently implemented using the fast Fourier transform (FFT). In this case, the consistency condition (Deans, 1983) $P_k(\nu_a) = (-1)^k P_k(-\nu_a)$ can be employed to obtain values of $P_k(\nu_a)$ for negative ν_a.

IV. NUMERICAL SIMULATIONS

We performed simulation studies to evaluate and compare the numerical and statistical properties of images obtained by use of the MS-E-C and MS-FBPP reconstruction algorithms.

A. Measurement Data. We investigated the statistical properties of the reconstruction algorithms under near-ideal conditions by employing a single component scattering object that exactly satisfied the (first-order) Born approximation. The propagation of deterministic artifacts by the reconstruction algorithms under less-than-ideal conditions was investigated by employing a two component scattering object that introduced strong and multiple-scattering effects into the measurement data.

A.1 Single-Scattered (Born) Data and Noise Model. The scattering object function, shown in figure 4, was taken to be a lossless, uniform cylindrical disk with a diameter of 30 pixels that was convolved with a symmetric Gaussian function with a standard deviation of 0.2 pixel. The Fourier transform of the object function was therefore approximately bandlimited to a circular disk of radius $\sqrt{2}\,\nu_0$ in its 2D Fourier space. It was assumed that the scatterer was weakly scattering, so that the Born approximation may reasonably be taken to hold. Therefore, these numerical simulations were designed to investigate the statistical properties of the reconstruction algorithms rather than the weak scattering model. Minimal-scan data sets were generated by using the FDP theorem to calculate simulated scattered field data for 96 measurement angles ϕ that were evenly spaced between 0 and $3\pi/2$. At each measurement angle, 128 samples were calculated with a sampling increment $\Delta\xi = 1/2\nu_0$, where ν_0 is the frequency of the incident plane wave.
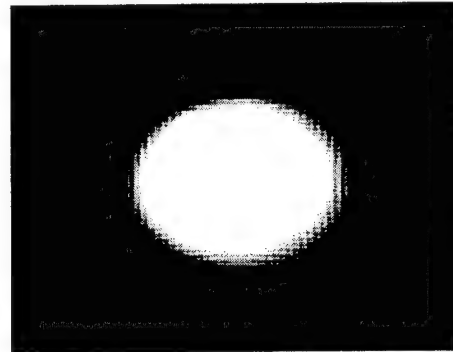

Figure 4. The original scattering object function was formed by convolving a uniform circular disk with a diameter of 30 pixels with a circularly symmetric Gaussian function with a standard deviation of 0.2 pixels.
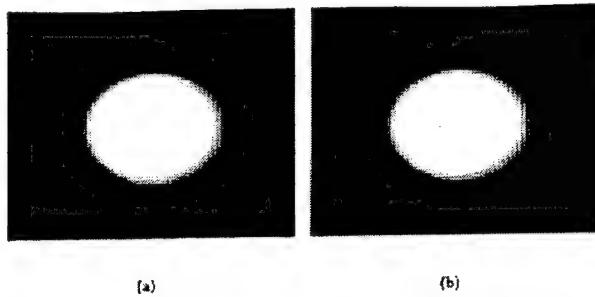
Figure 5. Images reconstructed from noiseless data using the (a) MS-E-C and (b) MS-FBPP reconstruction algorithms.

Figure 7. A plot of the local variance obtained from the MS-FBPP reconstructed images divided by the local variance obtained from the MS-E-C reconstructed images.

To simulate the effects of data noise, we treated the scattered data $\mathbf{u}_s(\xi, \phi)$ as a complex stochastic process with a real and an imaginary component denoted by, $\mathbf{u}_s^{(r)}(\xi, \phi)$ and $\mathbf{u}_s^{(i)}(\xi, \phi)$, respectively. Let $\mathbf{u}_s^{(r)} = u_s^{(r)} + \Delta \mathbf{u}_s^{(r)}$ and $\mathbf{u}_s^{(i)} = u_s^{(i)} + \Delta \mathbf{u}_s^{(i)}$, where $u_s^{(r)}$ and $u_s^{(i)}$ are the means of $\mathbf{u}_s^{(r)}$ and $\mathbf{u}_s^{(i)}$, respectively. The statistics of the deviates $\Delta \mathbf{u}_s^{(r)}$ and $\Delta \mathbf{u}_s^{(i)}$ are described by the circular Gaussian model:

$$p(\Delta u^{(r)}, \Delta u^{(i)}) = \frac{1}{2\pi\sigma_i\sigma_r} \times \exp\left[-\frac{1}{2}\left(\frac{\Delta u^{(r)^2}}{\sigma_r^2} + \frac{\Delta u^{(i)^2}}{\sigma_i^2}\right)\right], \quad (13)$$

where σ_r^2 and σ_i^2 are the variances of $\Delta \mathbf{u}_s^{(r)}(\xi, \phi)$ and $\Delta \mathbf{u}_s^{(i)}(\xi, \phi)$, respectively.

A.2 Multiple-Scattered Data. To investigate the impact of strong and multiple-scattering effects on the performance of the MS-E-C and MS-FBPP algorithms, which implicitly assume weak scattering conditions, we employed the two component scattering object shown in figure 8. This scattering object was composed of two uniform cylinders with radius 3λ whose centers were separated by 7λ. (λ = wavelength of incident plane wave.) The refractive index values of the cylinders were varied as described below. Twersky's theory of multiple scattering (Ishimaru, 1978) was used to calculate measurement data that contained second-order scattering effects. The first-order contributions to the measurement data were obtained by considering the interaction of the incident plane-wave with each cylinder, assuming the other cylinder to be absent. Note that this was an exact calculation that did not rely on the Born approximation. The second-order contributions to the measurement data were obtained by calculating the scattering component created
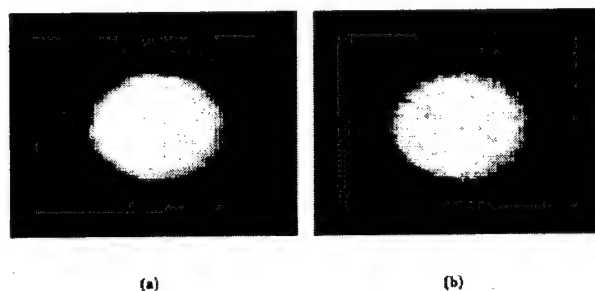
when the incident wave interacts with one cylinder and subsequently scatters off of the second cylinder before being measured (Azimi and Kak, 1983). Minimal-scan data sets were generated containing 96 measurement angles ϕ that were evenly spaced between 0 and $3\pi/2$. At each measurement angle, 128 samples were calculated with a sampling increment $\Delta\xi = 1/2\nu_0$.

B. Implementation Details. Both the MS-E-C and MS-FBPP reconstruction algorithms require the computation of the weighted minimal-scan data set that is defined in equation 4. This was accomplished by using the weighting function

$$w(\nu_m, \phi) = \begin{cases} \frac{1}{2} : 0 \le \phi \le \frac{\pi}{2} + 2\alpha \\ 1 : \frac{\pi}{2} + 2\alpha \le \phi \le \pi + 2\alpha \\ \frac{1}{2} : \pi + 2\alpha \le \phi \le \frac{3\pi}{2} \\ 0 : \frac{3\pi}{2} \le \phi \le 2\pi, \end{cases} \quad (14)$$

Figure 6. Images reconstructed from noisy and weakly scattered data using the (a) MS-E-C and (b) MS-FBPP reconstruction algorithms. The noisy data were generated using $\sigma_r = \sigma_i = 0.5$ in Eqn. 13.
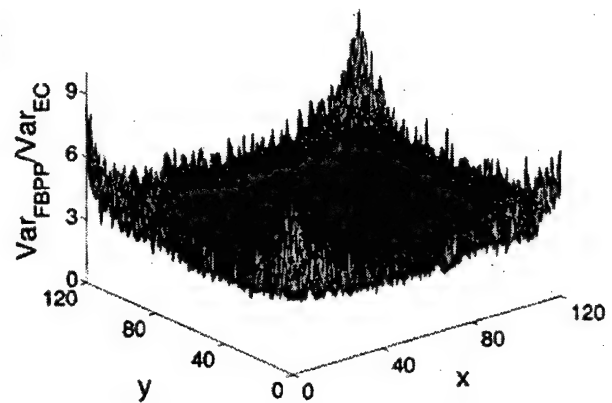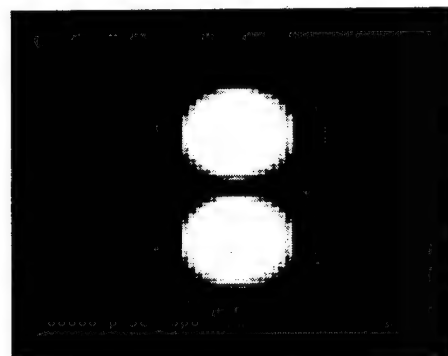

Figure 8. The geometry of the two component scattering object. We considered the cases where the refractive index of the uniform cylinders took the values $n(\bar{r}) = 1.01$, 1.05, and 1.08.

where $|\nu_m| \leq \nu_0$. This weighting function satisfies the requirements described by equation 5.

MS-E-C Algorithm. From the uniformly sampled values of the scattered field $u_s(\xi, \phi)$, $M_k(\nu_m)$, and hence $M'_k(\nu_m)$, can be determined at uniformly spaced values of ν_m. (This calculation can be performed using the FFT algorithm.) However, the uniformly spaced values of ν_m at which $M'_k(\nu_m)$ is known do not generally correspond to the uniformly spaced values of $\nu_a = \sqrt{\nu_m^2 - \nu_\mu^2}$ at which we are required to evaluate $P_k(\nu_a)$. For each of 65 evenly spaced values of ν_a spanning the range $0 \leq \nu_a \leq \sqrt{2}\,\nu_0$, we used linear interpolation to determine the values of M'_k ($\nu_m = \sqrt{\nu_a^2 + \nu_\mu^2}$) and M'_k ($\nu_m = -\sqrt{\nu_a^2 + \nu_\mu^2}$) from the sampled values of $M'_k(\nu_m)$ and $M'_k(-\nu_m)$, which were subsequently used in equation 13 to evaluate $P_k(\nu_a)$. For each value of k, zero-padding interpolation was employed to increase the sampling density along the ν_m axis of $M'_k(\nu_m)$ by a factor of three in order to increase the accuracy of the interpolation operation. The consistency condition $P_k(\nu_a) = (-1)^k P_k(-\nu_a)$ was employed to obtain the 64 samples of $P_k(\nu_a)$ for ν_a spanning the range $-\sqrt{2}\,\nu_0 \leq \nu_a < 0$. In our implementation of the FBPJ algorithm, an unapodized ramp filter was used. The interpolation necessary to align the backprojected data onto a 128×128 pixel discrete image matrix was performed using bilinear interpolation.

MS-FBPP Algorithm. In the MS-FBPP algorithm, at each measurement angle ϕ, $M(\nu_m, \phi)$ was multiplied by the depth-dependent filter $\nu_0/\nu' \,|\nu_m| e^{2\pi\nu_\mu\eta}$ for each of 128 discrete values of η. For each value of η, the filtered data was zero-padded to a length of 182 samples, upon which the inverse FFT was employed to transform the filtered data to the corresponding depth (value of η) in image space. This ensured that the pixel size of the images reconstructed using the MS-E-C and MS-FBPP algorithms were equivalent. The interpolation necessary to align the backpropagated data onto a 128×128 pixel discrete image matrix was performed using bilinear interpolation.

C. Simulation Studies

C.1 Single-Scattered (Born) Data Case. To study the noise properties of the reconstructed images quantitatively, we utilized the noiseless data set described in Section IV-A.1 along with the noise model in equation 13 with $\sigma_r = \sigma_i = 0.5$ to generate $N = 250$ noisy minimal-scan data sets. The MS-E-C and MS-FBPP algorithms were used to reconstruct sets of 250 noisy images from these noisy minimal-scan data sets. The local image variance was calculated empirically from the N sets of reconstructed images as
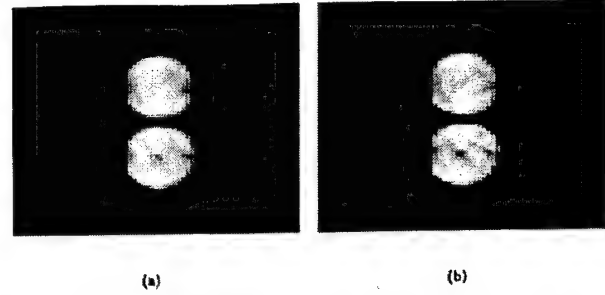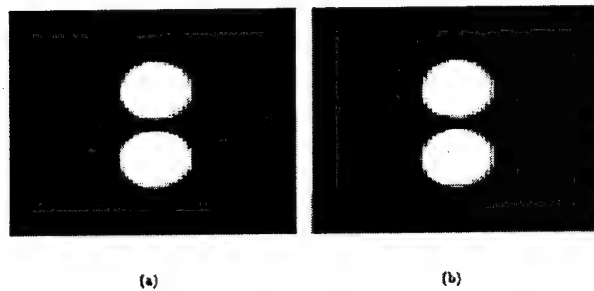

(a)   (b)

Figure 10. Images of the two component scattering object corresponding to $n(\vec{r}) = 1.05$, reconstructed by use of the (a) MS-E-C and (b) MS-FBPP reconstruction algorithms.

$$\mathrm{Var}\{a(\vec{r})\} = \frac{1}{N-1}\left(\sum_{i=1}^{N} a_i(\vec{r})^2 - \frac{1}{N}\left(\sum_{i=1}^{N} a_i(\vec{r})\right)^2\right), \quad (15)$$

where $a_i(\vec{r})$ is the ith image obtained with either the MS-E-C or MS-FBPP reconstruction algorithm.

C.2 Multiple-Scattering Case. To assess the impact of multiple-scattering effects on the performance of the MS-E-C and MS-FBPP algorithms, we employed the two component scattering object described in Section IV-A.2. We considered the three cases where the cylinders had refractive index values of $n(\vec{r}) = 1.01$, 1.05, and 1.08. For each value of $n(\vec{r})$, we used the MS-E-C and MS-FBPP algorithms to reconstruct the image from the corresponding data set. The percentage of cumulative error in the reconstructed images was quantified using the metric

$$E_{ROI} = \frac{\displaystyle\int_{ROI} |a(\vec{r}) - a_{true}(\vec{r})|^2 \, d\vec{r}}{\displaystyle\int_{ROI} |a_{true}(\vec{r})|^2 \, d\vec{r}} \times 100, \quad (16)$$

where $a_{true}(\vec{r})$ is the true scattering object function and the subscript 'ROI' denotes that the error was calculated over a 64×64 pixel^2 region of interest containing the scattering objects.

(a)   (b)

Figure 9. Images of the two component scattering object corresponding to $n(\vec{r}) = 1.01$, reconstructed by use of the (a) MS-E-C and (b) MS-FBPP reconstruction algorithms.

(a)   (b)
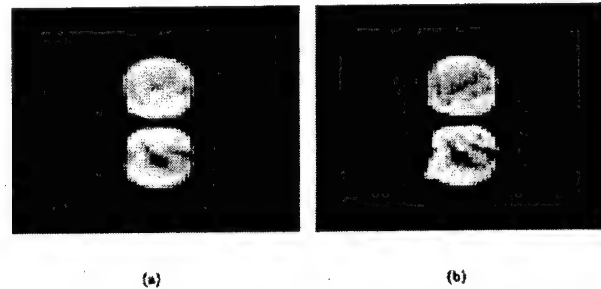
Figure 11. Images of the two component scattering object corresponding to $n(\vec{r}) = 1.08$, reconstructed by use of the (a) MS-E-C and (b) MS-FBPP reconstruction algorithms.

Table I. Error values of the reconstructed images shown in Figs. 9–11.

Contrast	MS-E-C Error	MS-FBPP Error
1.01	12.03	13.68
1.05	51.26	53.70
1.08	115.25	119.13

V. RESULTS

A. Single-Scattered (Born) Data Case. We first used the MS-E-C and MS-FBPP algorithms to reconstruct the scattering object function using the simulated noiseless minimal-scan data set. The images reconstructed using the MS-E-C and MS-FBPP algorithms are displayed in figures 5a and 5b, respectively. It is observed that, in the absence of noise, both the MS-E-C and MS-FBPP algorithms can, with high fidelity, reconstruct the original scattering object function from the minimal-scan data set.

Using one of the noisy minimal-scan data sets, we used the MS-E-C and MS-FBPP algorithms to reconstruct the scattering object function. The noisy images reconstructed using the MS-E-C and MS-FBPP algorithms are displayed in figures 6a and 6b, respectively. The image reconstructed using the MS-E-C algorithm (Fig. 6a) appears less affected by the data noise and more closely resembles the original object than does the image reconstructed using the MS-FBPP algorithm (Fig. 6b). The local image variance, which was empirically calculated from the two sets of 250 noisy images reconstructed using the MS-E-C and MS-FBPP algorithms, quantitatively confirms this observation. Figure 7 is a plot of the local variance obtained from the MS-FBPP reconstructed images divided by the local variance obtained from the MS-E-C reconstructed images. Clearly, the ratio of the variances is everywhere greater than one, and near the corners of the reconstructed image is as great as ten. This quantitatively demonstrates that the MS-E-C reconstruction algorithms are less susceptible to the effects of data noise than are the MS-FBPP reconstruction algorithms.

B. Multiple-Scattering Case. Using the MS-E-C and MS-FBPP algorithms we reconstructed the two component scattering objects shown in figures 9–11, which correspond to the cases where the cylinders had refractive index values of $n(\bar{r}) = 1.01$, 1.05, and 1.08, respectively. In each case, the image reconstructed by use of the MS-E-C algorithm (Figs. 9a–11a) appears to contain less pronounced artifacts than does the image reconstructed by use of the MS-FBPP algorithm (Figs. 9b–11b). This observation is confirmed by Table I, which shows that for each value of $n(\bar{r})$ the MS-E-C algorithm produced images that have lower error values than the corresponding images produced by the MS-FBPP algorithm. This quantitatively demonstrates that the MS-E-C algorithms are less susceptible to multiple-scattering effects and other deterministic inconsistencies than are the MS-FBPP algorithms. However, as one would expect, the performance of both algorithms dramatically deteriorates as the refractive index values increases and the Born condition (Chen and Stamnes, 1998) is severely violated.

VI. DISCUSSION

Previously we have shown (Pan and Anastasio, 1999) that, in DT employing the 2D classical scanning geometry, the minimal-scan data set acquired using view angles only in $[0, 3\pi/2]$ contains all of the information necessary to exactly reconstruct the scattering object function. We subsequently developed a class of MS-FBPP algo-

rithms that were capable of exactly reconstructing the scattering object function from the minimal-scan data set.

In this work, we have developed a novel class of reconstruction algorithms for the minimal-scan DT reconstruction problem. These algorithms, referred to as MS-E-C reconstruction algorithms, have distinct advantages over the MS-FBPP reconstruction algorithms. Because the FBPJ algorithm used by the MS-E-C algorithms does not involve a depth-dependent filtering, the MS-E-C algorithms are more computationally efficient than are the MS-FBPP algorithms. More importantly, we have quantitatively demonstrated that the MS-E-C algorithms are less susceptible to data noise, modeling errors due to the violation of weak scattering conditions, and other finite sampling effects than are the MS-FBPP algorithms. This result is consistent with the observation that the MS-FBPP algorithms involve more complicated numerical operations than do the MS-E-C algorithms, which may amplify the propagation of noise and errors into the reconstructed image. Therefore, the use of a MS-E-C algorithm instead of a MS-FBPP algorithm (using the same weighting function) will generally result in a reduction of the reconstructed image variance and/or a reduction of the image artifacts.

Recently, non-linear reconstruction algorithms that incorporate higher-order scattering approximations have been proposed for full-scan DT (Lu and Zhang, 1996; Tsihrintzis and Devaney, 2000b; Tsihrintzis and Devaney, 2000a). The generalization of these works to case of minimal-scan DT is an important task that is currently under way.

REFERENCES

M. Anastasio and X. Pan, Computationally efficient and statistically robust image reconstruction in 3D diffraction tomography, J Opt Soc Amer, 17 (2001a), 391–400.

M. Anastasio and X. Pan, A new reconstruction algorithm for reflection-mode diffraction tomography, IEEE Trans Image Process, 9 (2001b), 1262–1271.

M.P. Andre, P.J. Martin, G.P. Otto, L.K. Olson, T.K. Barrett, B.A. Apivey, and D.A. Palmer, A new consideration of diffraction computed tomography for breast imaging, Acoust Imag, 21 (1995), 379–390.

M. Azimi and A. Kak, Distortion in diffraction tomography caused by multiple scattering, IEEE Trans Med Imag, 2 (1983), 176–195.

B. Chen and J. Stamnes, Validity of diffraction tomography based on the first-Born and first-Rytov approximations, Appl Opt, 37 (1998), 2996–3006.

J. Cheng and S. Han, Diffraction tomography reconstruction algorithms for quantitative imaging of phase objects, J Opt Soc Amer (A), 18, 7 (2001), 1460–1464.

S. Deans, The Radon Transform and Some of Its Applications, (1983), Wiley, New York.

A. Devaney, A filtered backpropagation algorithm for diffraction tomography, Ultra Imag, 4 (1982), 336–350.

A. Devaney, Geophysical diffraction tomography, IEEE Trans Geo Rem Sens, 22 (1984), 3–13.

A. Ishimaru, Wave Propagation and Scattering in Random Media, (1978), Academic, New York.

G. Kino, Acoustic imaging for nondestructive evaluation, Proc IEEE, 67 (1979), 510–525.

Z.-Q. Lu and Y.-Y. Zhang, Acoustical tomography based on the second-order born transform perturbation approximation, IEEE Trans Ultra, Ferro, and Freq Cont, 43 (1996), 296–302.

C.E. Metz and X. Pan, A unified analysis of exact methods of inverting the 2-D exponential radon transform, with implications for noise control in spect, IEEE Trans Med Imag, 14 (1995), 643–658.

R. Mueller, M. Kaveh, and G. Wade, Reconstructive tomography and applications to ultrasonics, Proc IEEE, 67 (1979), 567–587.

S. Pan and A. Kak, A computational study of reconstruction algorithms for diffraction tomography: Interpolation versus filtered backpropagation, IEEE Trans Acous Sp and Sig Proc, 31 (1983), 1262–1275.

X. Pan, A unified reconstruction theory for diffraction tomography with considerations of noise control, J Opt Soc Amer (A), 15 (1998), 2312–2326.

X. Pan and M. Anastasio, Minimal-scan filtered back-propagation algorithms for diffraction tomography, J Opt Soc Amer (A), 16 (1999), 2896–2903.

E. Robinson, Image reconstruction in exploration geophysics, IEEE Trans Son and Ultrason, 31 (1984), 259–270.

W. Tabbara, B. Duchene, C. Pichot, D. Lesselier, L. Chommeloux, and N. Joachimowicz, Diffraction tomography: contribution to the analysis of some applications in microwaves and ultrasonics, Inverse Problems, 4 (1988), 305–331.

G. Tsihrintzis and A. Devaney, Higher order (nonlinear) diffraction tomography: Inversion of the Rytov series, IEEE Tran Inf Theory, 46 (2000a), 1748–1761.

G. Tsihrintzis and A. Devaney, Higher-order (nonlinear) diffraction tomography: Reconstruction algorithms and computer simulation, IEEE Trans Imag Proc, 9 (2000b), 1560–1572.

E. Wolf, Three-dimensional structure determination of semi-transparent objects from holographic data, Opt Comm, 1 (1969), 153–156.

Correspondence

On a Limited-View Reconstruction Problem in Diffraction Tomography

Xiaochuan Pan* and Mark A. Anastasio

Abstract—Diffraction tomography (DT) is an inversion technique that reconstructs the refractive index distribution of a scattering object. We previously demonstrated that by exploiting the redundant information in the DT data, the scattering object could be exactly reconstructed using measurements taken over the angular range $[0, \phi_{\min}]$, where $\pi < \phi_{\min} \leq 3\pi/2$. In this paper, we reveal a relationship between the maximum scanning angle and image resolution when a filtered backpropagation (FBPP) reconstruction algorithm is employed for image reconstruction. Based on this observation, we develop short-scan FBPP algorithms that reconstruct a low-pass filtered scattering object from measurements acquired over the angular range $[0, \Phi^c]$, where $\Phi^c < \phi_{\min}$.

Index Terms—Diffraction tomography, limited-view tomography, wavefield inversion techniques.

I. INTRODUCTION

In diffraction tomography (DT), a semi-transparent scattering object is interrogated using a diffracting optical or acoustical wavefield and the scattered wavefield around the object is measured and used to reconstruct the (low-pass filtered) refractive index distribution of the scattering object. The principles of DT have been extensively utilized for developing optical and acoustic tomographic imaging systems. Recently, interest in DT within the optical imaging community has increased because of its potential application to the diffuse-photon density wave tomography [1]–[3].

It was shown previously [4], [5] that, in two-dimensional (2-D) DT employing plane-wave or cylindrical-wave sources and the classical scanning geometry, one can reconstruct the scattering object from a minimal-scan data set comprised of measurements acquired over the angular range $[0, \phi_{\min}]$, where $\pi \leq \phi_{\min} \leq 3\pi/2$ is specified by the measurement geometry. In this paper, we reveal a relationship between image resolution and maximum scan angle, based upon which short-scan algorithms can be designed for reconstructing a low-pass filtered scattering object from measurements acquired over the angular range $[0, \Phi^c]$, where $\Phi^c < \phi_{\min}$. When the scattering object is sufficiently bandlimited, it can be exactly reconstructed from the limited-view measurements in $[0, \Phi^c]$. We present numerical examples that confirm our theoretical assertions.

II. BACKGROUND

Consider the classical scanning geometry of DT with a cylindrical wave source, as shown in Fig. 1. Let (x, y) and (r, θ) denote the fixed Cartesian and polar coordinate systems and
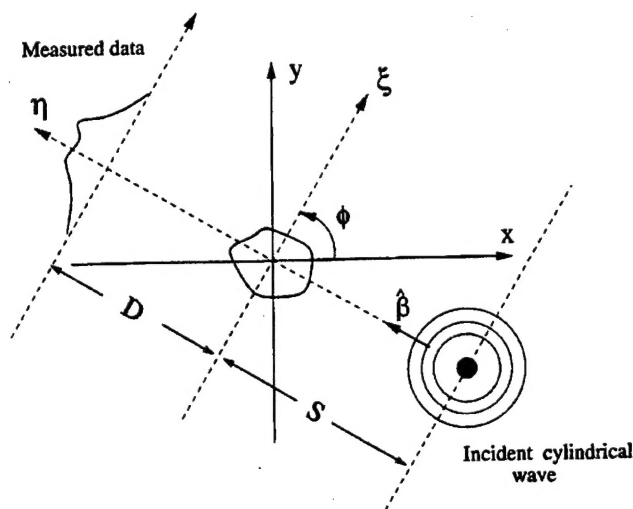
Fig. 1. The fan-beam scanning geometry of 2-D DT. The interrogating cylindrical wave propagates along the η axis and the scattered wave field is measured along the line $\eta = 1$. S (or D) denotes the distance between the source (or the detector) and the center of rotation.

(ξ, η) the rotated coordinate system. These systems are related by $x = r\cos\theta$, $y = r\sin\theta$, $\xi = x\cos\phi + y\sin\phi = r\cos(\phi - \theta)$, and $\eta = -x\sin\phi + y\cos\phi = -r\sin(\phi - \theta)$. The scattering object, which is embedded in a lossless and homogeneous background medium, is illuminated by a monochromatic cylindrical-wave $u_i(\xi, \phi)$ with complex amplitude U_0 and wavenumber $k = 2\pi\nu_0$, generated by a line source located at the position $\eta = -S$ on the η axis. From measurements of the scattered wavefield on the ξ axis at different view angles ϕ, one seeks to reconstruct the scattering object function $a(\vec{r})$, which is related to the refractive index distribution $n(\vec{r})$ within the scattering object by $a(\vec{r}) = n^2(\vec{r}) - 1$.

Let $u(\xi, \phi)$ and $u_s(\xi, \phi) = u(\xi, \phi) - u_i(\xi, \phi)$ denote the total and scattered wavefields measured along the line $\eta = D$ oriented at angle ϕ, as shown in Fig. 1. For the sake of convenience, we introduce a modified data function $M(\nu_m, \phi)$ that can be obtained readily from the scattered wavefield and is defined as

$$M(\nu_m, \phi) = \frac{\chi}{\pi\nu_0^2}\nu' \exp\left[-j2\pi(\nu' - \nu_0)D\right] \mathcal{F}_{\nu_m}\left\{\frac{u_s(\xi, \phi)}{u_i(\xi, \phi)}\right\} \quad (1)$$

where $\chi = \sqrt{S/(S + D)}$, $\nu' = \sqrt{\nu_0^2 - \nu_m^2/\chi^2}$, and $\mathcal{F}_{\nu_m}\{h(\xi)\} = 1/(2\pi)\int_{-\infty}^{\infty} h(\xi)e^{-j2\pi\nu_m\xi}d\xi$. The special case of plane-wave illumination ($S \to \infty$) corresponds to $\chi = 1$. Under the Born and paraxial approximations, Devaney derived the fan-beam Fourier diffraction projection (FDP) theorem [6], which relates $a(\vec{r})$ to the modified data function by

$$M(\nu_m, \phi) = \int_{-\infty}^{\infty}\int_{-\infty}^{\infty} a(\vec{r})$$
$$\cdot \exp\left\{-j2\pi\left[\frac{\nu_m}{\chi^2}\xi - (\nu' - \nu_0)\eta\right]\right\} d\vec{r},$$
$$\text{if } |\nu_m| \leq \chi\nu_0$$
$$= 0 \quad \text{if } |\nu_m| > \chi\nu_0. \quad (2)$$

The FDP theorem can also be derived by employing the Rytov approximation. In this case, (2) remains unchanged and only (1) needs to be appropriately redefined [6]. When ϕ is varied from 0 to 2π, the FDP theorem specifies a circular disk of (double) coverage centered at the origin with radius $\nu_0 \sqrt{1 + 1/\chi^2}$ in the 2-D Fourier space of $a(\vec{r})$. Conventional full-scan reconstruction algorithms, such as the well known filtered backpropagation (FBPP) algorithm [7], utilize this Fourier space coverage for reconstructing $a(\vec{r})$. We will refer to such a (low-pass filtered) reconstructed $a(\vec{r})$ as the "exact" image.

According to the fan-beam FDP theorem in (2), the modified data function $M(\nu_m, \phi)$ satisfies the consistency condition [4]

$$M(\nu_m, \phi) = M(-\nu_m, \phi + \pi - 2\alpha) \qquad (3)$$

where $\sin \alpha = \mathrm{sgn}(\nu_m)\left[((\nu' - \nu_0)^2/(\nu_m^2/\chi^2) + (\nu' - \nu_0)^2)\right]^{1/2}$. Using (3), one can show [4], [5] that the minimal-scan data acquired in the angular range $[0, \phi_{\min}]$ specifies a circular disk (with radius $\nu_0 \sqrt{1 + 1/\chi^2}$) of coverage in the Fourier space of $a(\vec{r})$, where

$$\phi_{\min} = \pi + 2\delta \quad \text{and} \quad \sin \delta = \frac{1}{\sqrt{1 + \frac{1}{\chi^2}}}. \qquad (4)$$

III. A LIMITED-VIEW RECONSTRUCTION PROBLEM FOR 2-D DT

We focus now on a limited-view problem, in which data are acquired only over the angular range $[0, \Phi^c]$, where $\pi < \Phi^c < \phi_{\min}$. In this situation, it is well known that the exact image cannot, in general, be reconstructed [8]. However, we demonstrate that algorithms can be developed for reconstructing a low-pass filtered approximation of the exact image. Consider a scattering object $a^c(\vec{r})$ whose 2-D Fourier transform $A^c(\vec{\nu})$ is bandlimited to a disk of radius R_c centered at the origin, where

$$R_c(\nu_c) = \left[\left(\frac{\nu_c}{\chi^2}\right)^2 + \left[\sqrt{\nu_0^2 - \left(\frac{\nu_c}{\chi}\right)^2} - \nu_0\right]^2\right]^{1/2} \qquad (5)$$

and $0 \leq \nu_c \leq \chi \nu_0$. Then, according to the fan-beam FDP theorem in (4), the modified data function $M(\nu_m, \phi)$ is nonzero only for $|\nu_m| \leq \nu_c$. The data space $\mathcal{W}_c = [|\nu_m| \leq \nu_c, 0 \leq \phi \leq 2\pi]$, in which the modified data function $M(\nu_m, \phi)$ is defined, can be divided into the four subspaces $\mathcal{A}$, $\mathcal{B}$, $\mathcal{C}$, and $\mathcal{D}$, as shown in Fig. 2, where $\mathcal{A} = [|\nu_m| \leq \nu_c, 0 \leq \phi \leq 2\alpha(\nu_m) + 2\alpha(\nu_c)]$, $\mathcal{B} = [|\nu_m| \leq \nu_c, 2\alpha(\nu_m) + 2\alpha(\nu_c) \leq \phi \leq \pi + 2\alpha(\nu_m)]$, $\mathcal{C} = [|\nu_m| \leq \nu_c, \pi + 2\alpha(\nu_m) \leq \phi \leq \Phi^c]$, and $\mathcal{D} = [|\nu_m| \leq \nu_c, \Phi^c \leq \phi \leq 2\pi]$. The value of Φ^c is determined by

$$\Phi^c = \pi + 2\alpha(\nu_c). \qquad (6)$$

Using (3), it can be verified that information of $M(\nu_m, \phi)$ in subspace $\mathcal{A}$ is redundant to that of $M(\nu_m, \phi)$ in subspace $\mathcal{C}$. Similarly, information of $M(\nu_m, \phi)$ in subspace $\mathcal{B}$ is redundant to that of $M(\nu_m, \phi)$ in subspace $\mathcal{D}$. Therefore, in principle, the modified data function $M(\nu_m, \phi)$ is completely specified by its values in the subspaces $\mathcal{A}$ and $\mathcal{B}$. However, because the boundary between the subspaces $\mathcal{B}$ and $\mathcal{C}$ is a nonlinear function of ν_m and ϕ and because each horizontal line in $\mathcal{W}_c$ corresponds to a measurement acquired at a particular angle ϕ, the information in subspaces $\mathcal{B}$ and $\mathcal{C}$ cannot in practice be determined independently of each other. Consequently, in order to determine $M(\nu_m, \phi)$ in subspaces $\mathcal{A}$ and $\mathcal{B}$, it is necessary to scan the union $\mathcal{A} \cup \mathcal{B} \cup \mathcal{C} = [|\nu_m| \leq \nu_c, 0 \leq \phi \leq \Phi^c]$. This observation can also be understood by examining the 2-D Fourier space coverage of $a(\vec{r})$ that is obtained by varying the scanning angle from 0 to Φ^c. As shown in Fig. 3, although the disk of Fourier space coverage with
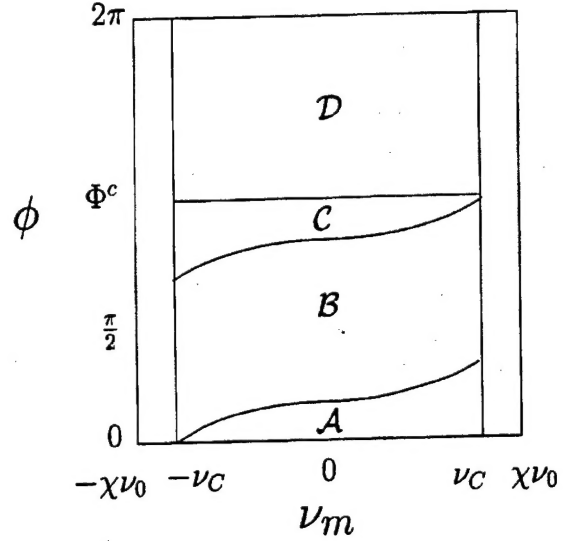

Fig. 2. The full-scan data space $\mathcal{W}^c = \mathcal{A} \cup \mathcal{B} \cup \mathcal{C} \cup \mathcal{D}$ contains data in the angular range $[0, 2\pi]$. The subspace $\mathcal{A} \cup \mathcal{B} \cup \mathcal{C}$ in $[0, \Phi^c]$ contains all of the information necessary for exact reconstruction of the scattering object function whose 2-D Fourier transform is bandlimited to a disk of radius $R_c(\nu_c)$.
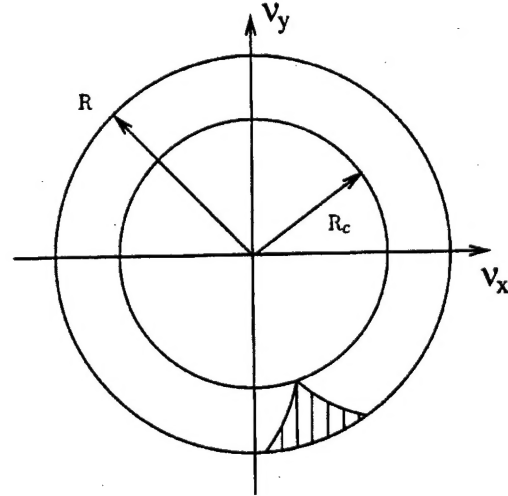

Fig. 3. The 2-D Fourier space coverage of the scattering object that is obtained by varying ϕ from 0 to Φ^c. The disk of Fourier space coverage with radius $R = \nu_0 \sqrt{1 + 1/\chi^2}$ is incomplete, with the shaded region denoting the missing data. However, the coverage corresponding to the disk of radius R_c, which is defined by (5), is completely specified. In generating the figure, $\Phi^c = 230°$ and $\chi = 1$ were utilized.

radius $R = \nu_0 \sqrt{1 + 1/\chi^2}$ is incomplete, the coverage corresponding to the disk of radius $R_c(\nu_c)$ is completely specified. Therefore, in order to exactly reconstruct $a^c(\vec{r})$ whose 2-D Fourier transform $A^c(\vec{\nu})$ is bandlimited to a disk of radius $R_c(\nu_c)$, only measurements corresponding to view angles in $[0, \Phi^c]$ are required. Alternatively, for an arbitrary scattering object $a(\vec{r})$ and specified $\Phi^c > \pi$, one can readily reconstruct $a^c(\vec{r})$, which is a low-pass filtered version of $a(\vec{r})$ whose 2-D Fourier transform is bandlimited to the disk of radius $R_c(\nu_c)$, where the value of the data cutoff frequency $0 \leq \nu_c \leq \chi \nu_0$ is determined by (6).

A plot of Φ^c versus ν_c/ν_0 for plane- and cylindrical-wave illumination is shown in Fig. 4. As expected, the maximum scanning angle Φ^c is a monotonically increasing function of the data cutoff frequency ν_c.
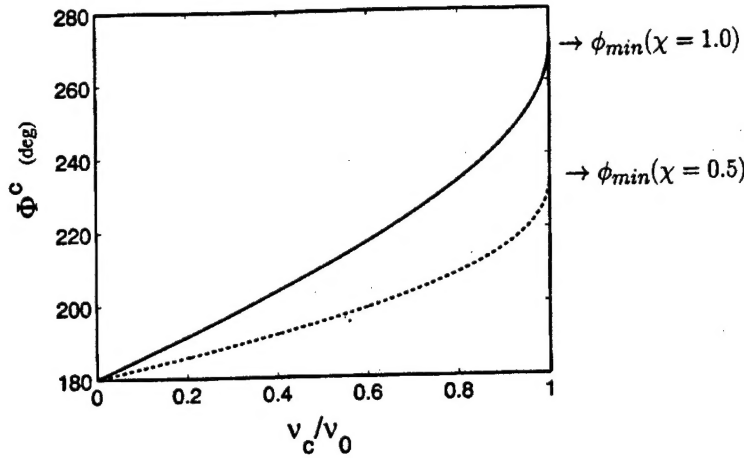
Fig. 4. A plot of Φ^c versus ν_c/ν_0 for $\chi = 1$ (solid line) and $\chi = 0.5$ (dashed line).

The nonlinear shape of the curves indicates the scanning angle can be reduced from $\phi_{\min}$ (e.g., by 30°) with little loss of resolution in the reconstructed image. Also, the fact that the plane-wave ($\chi = 1$) curve is everywhere higher than the cylindrical-wave ($\chi = 0.5$) curve reflects the fact that the angular scanning requirements of plane-beam DT are more restrictive than for fan-beam DT [5].

IV. SHORT-SCAN RECONSTRUCTION ALGORITHMS FOR LIMITED-VIEW DT

Although the data $\mathcal{A} \cup \mathcal{B} \cup \mathcal{C}$ in Fig. 2 contains all of the information necessary for reconstruction of $a^c(\vec{r})$, subspaces $\mathcal{A}$ and $\mathcal{C}$ contain redundant information that needs to be properly normalized in the reconstruction process. This can be achieved by introducing a weighted modified data function as [4], [5]

$$M'(\nu_m, \phi) = w(\nu_m, \phi) M(\nu_m, \phi) \tag{7}$$

where $w(\nu_m, \phi)$ satisfies

$$w(\nu_m, \phi) + w(-\nu_m, \phi + \pi - 2\alpha) = 1 \tag{8a}$$

everywhere in the data space $\mathcal{W}_c$

$$w(\nu_m, \phi) = 1 \tag{8b}$$

in subspace $\mathcal{B}$ and

$$w(\nu_m, \phi) = 0 \tag{8c}$$

in the subspace $\{\mathcal{D} \cup [|\nu_m| > \nu_c, 0 \leq \phi \leq 2\pi]\}$. The image $a^c(\vec{r})$ can be reconstructed using a *short-scan FBPP (SS-FBPP) reconstruction algorithm* given by

$$
a^{(w)}(r, \theta) = \int_{\phi=0}^{\Phi^c} \int_{\nu_m=-\nu_c}^{\nu_c} \frac{\nu_0}{\nu'} |\nu_m| M'(\nu_m, \phi)
$$
$$
\times \exp\left[j 2\pi \, \text{sgn}(\nu_m) \sqrt{\frac{\nu_m^2}{\chi^2} + (\nu' - \nu_0)^2} \, r \cos(\phi - \alpha - \theta) \right]
$$
$$
\times d\nu_m d\phi \tag{9}
$$

which reduces to the full-scan fan-beam FBPP algorithm [5] when $\Phi^c = 2\pi$ and $w(\nu_m, \phi) = 1/2$. Note that different choice for $w(\nu_m, \phi)$ that satisfy (8), in effect, specify different SS-FBPP algorithms.

V. NUMERICAL RESULTS

To validate the theoretical results above, we considered a numerical phantom containing two elliptical disks whose 2-D Fourier transform was approximately bandlimited to a disk of radius $R_c(\nu_c = 0.45\nu_0)$ [see (5)]. Data sets of simulated scattered fields were generated using the plane-wave FDP theorem (i.e., $\chi = 1$) and using various values for Φ^c. We reconstructed images, which are shown in Fig. 5, from these data sets using the conventional FBPP and SS-FBPP algorithms. The SS-FBPP algorithm was specified by a weighting function $w(\nu_m, \phi)$ that took on the values 1/2, 1, 1/2, and 0, in the data subspaces $\mathcal{A}, \mathcal{B}, \mathcal{C}$, and $\mathcal{D}$, respectively. Fig. 5(a) shows images reconstructed by use of the FBPP algorithm (left) and SS-FBPP algorithm (right), using data sets corresponding to $\Phi^c = 2\pi$ and $\Phi^c = \phi_{\min}(\chi = 1) = 3\pi/2$, respectively. It is observed that both images appear virtually identical, reflecting the fact that both of these data sets contain the complete information about the scattering object.

Fig. 5(b) shows images reconstructed by use of the FBPP algorithm (left) and SS-FBPP algorithm (right), using a data set corresponding to $\Phi^c = \pi + 2\alpha\underbrace{(0.45\nu_0)}_{\nu_c}(\approx 207°)$. Clearly, the image reconstructed using the FBPP algorithm is distorted and contains artifacts. However, the image reconstructed by use of the SS-FBPP algorithm appears correct and virtually identical to the images shown in Fig. 5(a). This confirms our assertion that the SS-FBPP algorithms, which utilize in the angular range $[0, \Phi^c]$, can exactly reconstruct a scattering object $a^c(\vec{r})$ whose 2-D Fourier transform $A^c(\vec{\nu})$ is bandlimited to a disk of radius $R_c(\nu_c)$, where ν_c and Φ^c are related by (6).

Fig. 5(c) shows images reconstructed by use of the FBPP algorithm (left) and SS-FBPP algorithm (right), using a data set corresponding to $\Phi^c = \pi + 2\alpha(0.25\nu_0)(\approx 195°)$. Note that because the 2-D Fourier transform of $a(\vec{r})$ has support on the disk or radius $R_c(\nu_c = 0.45\nu_0)$, the measurements in the angular range $[0, \Phi^c = 195°]$ do not completely specify the scattering object (i.e., the disk of coverage in 2-D Fourier space with radius $R_c(\nu_c = 0.45\nu_0)$ will not be completely filled in.) As expected, the image reconstructed using the FBPP algorithm is blurred, distorted and contains artifacts. The image reconstructed using the SS-FBPP algorithm also appears blurred, but does not contain any noticeable distortions or artifacts. This confirms our assertion that, when the 2-D Fourier transform of a scattering object $a(\vec{r})$ is not bandlimited to a disk of radius $R_c(\nu_c)$, the SS-FBPP algorithms that utilize the measurements corresponding to view angles in $[0, \Phi^c]$ (where ν_c and Φ^c are related by (6)) can reconstruct a low-pass filtered version of $a(\vec{r})$ whose 2-D Fourier transform is bandlimited to
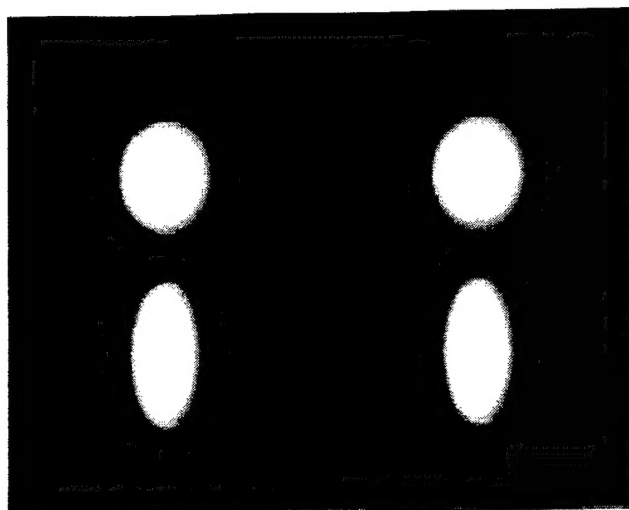
(a)
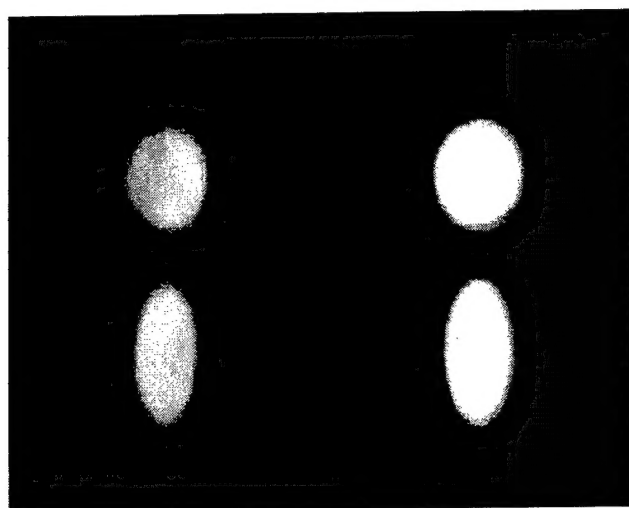
(b)
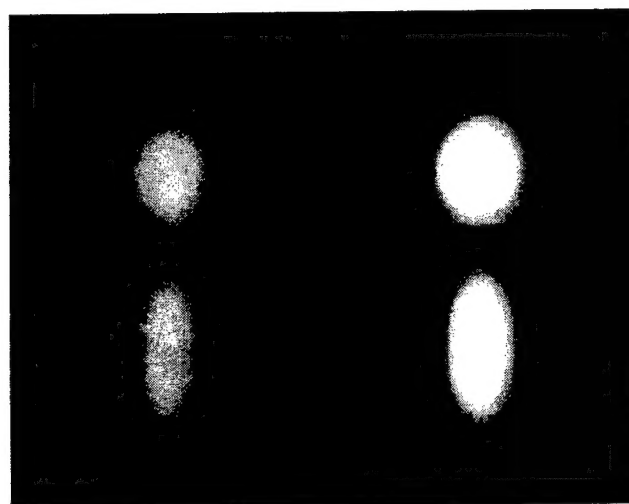
(c)

Fig. 5. Images reconstructed using the FBPP and SS-FBPP algorithms for various simulated data sets. See the text for a detailed description.

the disk of radius $R_c(\nu_c)$. In this particular example, the 2-D Fourier transform of the image reconstructed by use of the SS-FBPP algorithm is bandlimited to a disk of radius $R_c(.25/.45\ \nu_c)$.

VI. SUMMARY

We demonstrated previously [4], [5] that in 2-D DT employing plane-wave or cylindrical-wave sources, one can exactly reconstruct the scattering object from a minimal-scan data set acquired using view angles only in $[0, \phi_{\min}]$, where $\pi \leq \phi_{\min} \leq 3\pi/2$ is a specified function of the measurement geometry. In this study, we have demonstrated that when measurements are available only for view angles in $[0, \Phi^c]$, where $\pi < \Phi^c < \phi_{\min}$, a simple relationship exists between the maximum scanning angle Φ^c and the image resolution when a FBPP algorithm is employed to reconstruct the image. By properly weighting the measurement data, a low-pass filtered approximation of the scattering object that is free of conspicuous artifacts can be obtained from the measurements corresponding to view angles in $[0, \Phi^c]$. When the scattering object is sufficiently bandlimited, it can be exactly reconstructed. This observation is practically useful, because it provides a convenient mechanism for regularizing the severely ill-posed limited-view DT reconstruction problem; when the maximum scanning angle Φ^c is greater than π, a stable reconstruction can always be performed by sacrificing spatial resolution in the reconstructed image. It can be demonstrated that the statistical properties of the SS-FBPP algorithms are qualitatively similar to those of the minimal-scan FBPP reconstruction algorithms investigated previously [5]. In the limited-view radon transform inversion problem [9], an analogous regularization mechanism does not exist and some sort of *a priori* information regarding the object function is generally required to effectively regularize the problem.

Because we have assumed a 2-D imaging geometry in this study, the developed SS-FBPP reconstruction algorithms may be useful for applications in which out-of-plane scattering is not significant. In diffuse-photon density wave tomography, the wavenumber is complex-valued and the FDP theorem describes a mapping between the data function and a set of complex-valued frequencies of the scattering object function's Fourier transform. The extension of the concepts and techniques introduced in this correspondence to the case where the wavenumber is complex-valued and to the three-dimensional reconstruction problem represent important topics for future research.

REFERENCES

[1] S. Norton and T. Vo-Ding, "Diffraction tomographic imaging with photon density waves: An explicit solution," *J. Opt. Soc. Amer. A*, vol. 15, pp. 2670–2677, 1998.

[2] X. Li, T. Durduran, A. G. Yodh, B. Chance, and D. N. Pattanayak, "Diffraction tomography for biomedical imaging with diffuse photon density waves," *Optics Lett.*, vol. 22, pp. 573–575, 1997.

[3] C. Matson, "A diffraction tomographic model of the forward problem using diffuse photon density waves," *Optics Exp.*, vol. 1, pp. 6–11, 1997.

[4] X. Pan and M. Anastasio, "Minimal-scan filtered backpropagation algorithms for diffraction tomography," *J. Opt. Soc. Amer. A*, vol. 16, pp. 2896–2903, 1999.

[5] M. Anastasio and X. Pan, "Full- and minimal-scan reconstruction algorithms for fan-beam diffraction tomography," *Appl. Optics*, vol. 40, no. 20, pp. 3334–3345, 2001.

[6] A. J. Devaney, "Generalized projection-slice theorem for fan-beam diffraction tomography," *Ultrason. Imag.*, vol. 7, pp. 264–275, 1985.

[7] ——, "A filtered backpropagation algorithm for diffraction tomography," *Ultrason. Imag.*, vol. 4, pp. 336–350, 1982.

[8] ——, "The limited view problem in diffraction tomography," *Inverse Prob.*, vol. 5, p. 501, 1989.

[9] M. Davison, "The ill-conditioned nature of the limited angle tomography problem," *SIAM J. Appl. Math.*, vol. 43, pp. 428–448, 1983.